

FINITE ELEMENT ANALYSIS OF  
FREEFORM COMPOSITE  
STRUCTURES

By

JEFFREY RYAN CALLICOAT

Bachelor of Science

Oklahoma State University

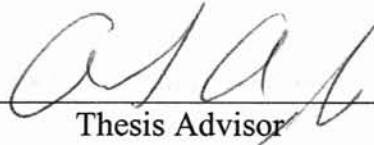
Stillwater, Oklahoma

2000

Submitted to the Faculty of the  
Graduate College of the  
Oklahoma State University  
in partial fulfillment of  
the requirements for  
the Degree of  
MASTER OF SCIENCE  
December, 2002

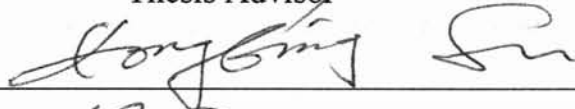
FINITE ELEMENT ANALYSIS OF  
FREEFORM COMPOSITE  
STRUCTURES

Thesis Approved:



---

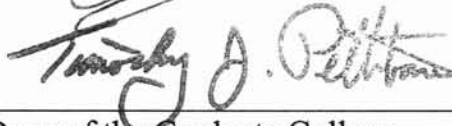
Thesis Advisor



---



---



---

Dean of the Graduate College

## ACKNOWLEDGEMENTS

I would like to thank my major advisor, Dr. Andrew S. Arena, Jr., for his continual support and encouragement throughout this project. In addition, I would like to thank the other members of my Graduate Advisory Committee, Dr. H. Lu and Dr. R. D. Delahoussaye, for their time, effort, and help during the course of this work.

I also wish to express my sincere appreciation to my family and friends who encouraged me and stood by me throughout my educational career.

## TABLE OF CONTENTS

Chapter	Page
INTRODUCTION.....	1
1.1. Background.....	1
1.2. Research Objective .....	3
LITERATURE REVIEW .....	4
2.1. Advanced Composite Materials.....	4
2.1.1. Reinforcing Fibers .....	5
2.1.2. Resin Matrix.....	8
2.2. Rapid Prototyping .....	8
2.2.1. Stereolithography.....	10
2.2.2. Fused Deposition Modeling.....	11
2.3. Finite Element Analysis.....	12
2.3.1. Implementation of FEA .....	14
2.3.2. The H-Method and the P-Method.....	19
2.3.2.1. The H-Method.....	20
2.3.2.2. The P-Method .....	23
2.3.2.3. Advantages of the P-Method .....	25
2.4. Pro/MECHANICA.....	26
2.4.1. Integrated Mode and Independent Mode .....	26
2.4.2. Convergence .....	27
2.4.3. AutoGEM.....	30
METHODOLOGY .....	32
3.1. Model Development.....	32
3.1.1. Material Properties.....	34
3.1.2. Boundary Conditions for 3-Point Bending Analysis .....	36
3.1.2.1. Loads.....	37
3.1.2.2. Constraints .....	39
3.1.3. Use of Symmetry .....	43
3.1.3.1. Full Model.....	45

3.1.3.2. Half Model .....	46
3.1.3.3. Quarter Model.....	47
3.1.4. Avoidance of Contact Regions .....	49
3.1.5. Honeycomb Model.....	53
3.1.5.1. All Solid Elements .....	54
3.1.5.2. Facings Compressed to Shells .....	56
3.1.5.3. Core Walls and Facings Are Shells .....	60
3.2. Implementation to Test Specimen A.....	68
3.3. Implementation to Test Specimen B.....	69
3.4. Effect of Number of Carbon Fiber Layers.....	70
3.5. Effect of Wall Thickness .....	70
3.6. Effect of Core Orientation .....	71
 RESULTS.....	 73
4.1. Results for Test Specimen A.....	73
4.1.1. All Solid Elements .....	73
4.1.2. Facings Compressed to Shells .....	74
4.1.3. Core Walls and Facings Are Shells .....	75
4.1.4. Comparison to Experimental Results.....	77
4.2. Results for Test Specimen B.....	84
4.2.1. All Solid Elements .....	85
4.2.2. Facings Compressed to Shells .....	86
4.2.3. Core Walls and Facings Are Shells .....	89
4.2.4. Comparison to Experimental Results.....	93
4.3. Effect of Number of Carbon Fiber Layers.....	94
4.4. Effect of Wall Thickness .....	96
4.5. Effect of Core Orientation .....	97
 CONCLUSIONS AND RECOMMENDATIONS.....	 99
5.1. Conclusions.....	99
5.2. Recommendations.....	100
 BIBLIOGRAPHY .....	 102
 APPENDICES.....	 105
APPENDIX A: RPC 700 ND RESIN DATA SHEET .....	106
APPENDIX B: LTM25 / CFS003 2x2 TWILL DATA SHEET .....	107
APPENDIX C: COMPARISON OF TWO LOADING CONDITIONS.....	108

APPENDIX D: COMPARISON OF DISPLACEMENT AND STRESS VALUES AT SEED POINT LOCATIONS IN HONEYCOMB CORE TEST SPECIMEN .....	109
APPENDIX E: SEED POINT LOCATIONS IN TEST SPECIMEN A .....	112
APPENDIX F: COMPARISON OF DISPLACEMENT AND STRESS VALUES AT SEED POINT LOCATIONS IN TEST SPECIMEN B ....	113

## LIST OF TABLES

Table	Page
Table 3.1: In-plane properties of LTM25 / CFS003 .....	35
Table 3.2: Comparison of analyses on full model, half model, and 1/4 model.....	49
Table 3.3: Comparison of analyses with and without contact regions.....	53
Table 4.1: Effect of number of carbon fiber layers .....	95
Table 4.2: Effect of wall thickness.....	96
Table 4.3: Test Specimen B comparison of core orientations.....	98
Table 4.4: Test Specimen A comparison of core orientations .....	98

## LIST OF FIGURES

Figure	Page
Figure 2.1: Common weave patterns of carbon fiber fabric.....	7
Figure 2.2: Thin plate discretized using triangular elements .....	15
Figure 2.3: Cantilever beam with end load .....	21
Figure 2.4: Using h-elements to model the cantilever beam .....	22
Figure 2.5: Using h-elements to model a stress distribution .....	23
Figure 2.6: Using one p-element to model the cantilever beam.....	24
Figure 2.7: Using p-elements to model a stress distribution .....	25
Figure 2.8: Sample convergence plots from Pro/MECHANICA.....	29
Figure 2.9: AutoGEM parameters .....	31
Figure 3.1: Loading condition for three-point bending test .....	32
Figure 3.2: Experimental setup for three-point bending test.....	33
Figure 3.3: Coordinate directions for laminate properties .....	35
Figure 3.4: Components in FEM model .....	37
Figure 3.5: Applied load in FEM model .....	38
Figure 3.6: FEM model incorporating Instron head.....	39
Figure 3.7: Constraints for FEM model .....	41
Figure 3.8: Bending stress in deformed test specimen .....	42
Figure 3.9: Planes of symmetry.....	44



Figure 3.10: Convergence plots for full model .....	45
Figure 3.11: Fringe plots of von Mises stress in full model.....	46
Figure 3.12: Fringe plots of von Mises stress in half model .....	47
Figure 3.13: Fringe plots of von Mises stress in 1/4 model .....	48
Figure 3.14: Contact region in 1/4 model.....	51
Figure 3.15: Convergence plots for analysis without contact region .....	52
Figure 3.16: Von Mises stress fringe plots for analysis without contact region .....	52
Figure 3.17: Honeycomb core .....	53
Figure 3.18: Convergence plots for honeycomb-core test specimen .....	54
Figure 3.19: Von Mises stress fringe plots for honeycomb-core test specimen, all solid elements .....	55
Figure 3.20: Convergence plots for honeycomb-core test specimen, with facings compressed to shells .....	58
Figure 3.21: Stress convergence at seed points within test specimen .....	59
Figure 3.22: Von Mises stress in honeycomb-core test specimen, with facings compressed to shells .....	60
Figure 3.23: Fringe plot of deformed test specimen, showing penetration of rubber pad into core .....	62
Figure 3.24: Datum points to “tie” surfaces of rubber pad and loading pad to composite beam .....	63
Figure 3.25: Convergence plots for honeycomb-core test specimen, with core walls and facings modeled as shells .....	64
Figure 3.26: Stress convergence at seed points within test specimen .....	65
Figure 3.27: Von Mises stress in honeycomb-core test specimen, with core walls and facings modeled as shells .....	66
Figure 3.28: Von Mises stress fringe plots using capping surfaces .....	67
Figure 3.29: Test Specimen A .....	68
Figure 3.30: Test Specimen B .....	69

Figure 3.31: Alternate core orientation based on Test Specimen B .....	71
Figure 3.32: Alternate core orientation based on Test Specimen A.....	72
Figure 4.1: Test Specimen A.....	73
Figure 4.2: Convergence plots for Test Specimen A, with core walls and facings modeled as shells.....	76
Figure 4.3: Stress convergence at seed points within Test Specimen A .....	76
Figure 4.4: Von Mises stress in Test Specimen A, with core walls and facings modeled as shells.....	77
Figure 4.5: Load versus deflection curves based on computational and experimental results.....	78
Figure 4.6: Instron load frame .....	80
Figure 4.7: Experimental load versus deflection curve for small steel plate .....	81
Figure 4.8: Test Specimen A load versus deflection curves based on computational and experimental results, corrected for Instron deflection .....	81
Figure 4.9: Exploded view of experimental setup.....	83
Figure 4.10: Test Specimen B .....	85
Figure 4.11: Convergence plots for Test Specimen B, all solid elements.....	85
Figure 4.12: Von Mises stress in Test Specimen B, all solid elements.....	86
Figure 4.13: Convergence plots for Test Specimen B, with facings compressed to shells.....	87
Figure 4.14: Stress convergence at seed points within Test Specimen B, with facings compressed to shells .....	88
Figure 4.15: Von Mises stress in Test Specimen B, with facings compressed to shells.....	89
Figure 4.16: Convergence plots for Test Specimen B, with core walls and facings modeled as shells.....	90
Figure 4.17: Stress convergence at seed points within Test Specimen B, with core walls and facings modeled as shells .....	91
Figure 4.18: Von Mises stress in Test Specimen B, with core walls and facings modeled as shells.....	92

Figure 4.19: Test Specimen B load versus deflection curves based on computational and experimental results, corrected for Instron deflection ..... 93

Figure 4.20: Effect of number of carbon fiber layers ..... 95

Figure 4.21: Effect of core wall thickness ..... 97

## NOMENCLATURE

3DP	Three-Dimensional Printing
CAD	computer-aided design
CNC	computer numerical control
DOF	degree of freedom
E	Young's modulus
{F}	global force vector
{f <sup>e</sup> }	element force vector
FDM	Fused Deposition Modeling
FEA	finite element analysis
FEM	finite element method
f <sub>x</sub> , f <sub>y</sub>	components of internal distributed force
G	shear modulus
I	area moment of inertia
IGES	Initial Graphics Exchange Specifications file
IRHD	International Rubber Hardness Degree (equivalent to Shore A)
[K]	global stiffness matrix
[k <sup>e</sup> ]	element stiffness matrix
L	length

LOM	Laminated Object Manufacturing
MJM	Multi-Jet Modeling
P	applied load
{Q}	global displacement vector
{q <sup>e</sup> }	element displacement vector
RP	rapid prototyping
SFF	solid freeform fabrication
SL	stereolithography
SLA	Stereolithography Apparatus
SLI	SLIce file
SLS	Selective Laser Sintering
STL	STereoLithography file
T	traction load
t	thickness
UV	ultraviolet
u, v	components of displacement in x- and y-directions
x, y, z	coordinate directions
$\epsilon_x, \epsilon_y$	components of normal strain
$\gamma_{xy}$	engineering shear strain
$\nu$	Poisson's ratio
$\rho$	density
$\sigma_x, \sigma_y$	components of normal stress
$\tau_{xy}$	shear stress

## CHAPTER 1

### INTRODUCTION

#### 1.1. Background

Freeform composite structures result from combining advanced composite materials with rapid prototyping (RP) technology. Advanced composite materials provide these structures with high strength, while RP technology allows the structures to be built without reliance upon part-specific rigid tooling.

Advanced composites (also known as engineered composites) are a class of materials consisting of high strength, high modulus fibers suspended in a resin matrix. The fibers give the material its strength, while the resin matrix bonds the fibers together and helps transfer load from one fiber to the next. In general, advanced composites have high strength-to-weight ratios, which makes them very useful in the aerospace industry. A main disadvantage of composite materials, though, is that one often requires special tooling (i.e., forms or molds) to fabricate a composite part. The tooling can be quite expensive or difficult to obtain, and every unique structure may require its own special tool.

Rapid prototyping is a set of manufacturing processes for fabricating physical objects directly from three-dimensional computer-aided-design (CAD) models.

There are numerous different RP construction techniques and build materials, but they all share the same general approach: a computer model of the desired object is sliced mathematically into thin layers, and then the RP fabricator reads the geometry of each slice and builds the desired object in a layerwise additive fashion. Traditionally, RP parts are used only for visualization of structures and testing the fit of assembly components since the structures generally have relatively low strength.

Research is currently being performed at Oklahoma State University to utilize rapid prototyping parts as a substructure upon which composite laminates are fabricated. On one hand, this “freeform composite manufacturing” is a technique for embedding strength (via composite materials) into the RP part. On the other hand, it is a technique for manufacturing advanced composite parts without the need for expensive tooling (the RP part itself serves as the tool). By either interpretation, the result is fast, cost-efficient production of strong, lightweight structures.

As the viability of freeform composite parts increases, so does the need for analysis tools to evaluate these structures. Just as with other manufactured products, good design of freeform composites requires prior understanding of the stresses and strains that the part will experience in service. The current standard for gaining this type of information is finite element analysis.

Numerous software packages exist for performing finite element analysis of structures. Among them are ANSYS, CADRE, ABAQUS, and Pro/MECHANICA. For this research, Pro/MECHANICA has been identified as the software of choice because it interfaces so well with the Pro/ENGINEER solid modeling software often used to generate the CAD models for RP construction.

## 1.2. Research Objective

The objective of this research is to evaluate the Pro/MECHANICA software as a tool for performing finite element analysis of freeform composite structures. Specifically, we wish to analyze several composite beam test specimens obtained through freeform composite construction, and we want to model their response to an ASTM three-point bending test. After running the Pro/MECHANICA analysis, we will compare the FEM computational results to experimental results obtained in OSU's mechanical engineering laboratories. The computer models can then be modified and re-analyzed to study the effects of changing the geometry or composition of the structures.



## CHAPTER 2

### LITERATURE REVIEW

This research project involves the finite element analysis of freeform composite structures using Pro/MECHANICA. As discussed in the previous chapter, freeform composite structures result from the combination of rapid prototyping technology and advanced composite materials.

To provide a thorough background for this research, the present chapter gives an overview of advanced composite materials and rapid prototyping technology, followed by an investigation of the finite element method and PTC's Pro/MECHANICA software package.

#### 2.1. Advanced Composite Materials

A composite material is typically defined as any material made up of two or more constituent materials, such that the properties of the composite are superior to those of the constituents acting independently. The term "advanced composites" (or, alternatively, "engineered composites") refers to a class of materials manufactured from high performance fibers suspended in a resin matrix, offering structural performance far superior to conventional materials.

The development of advanced composites began in the 1960's, motivated by the need for strong yet lightweight manufacturing materials for the aerospace industry. As materials were developed, they quickly found application in other manufacturing markets as well, and they are now utilized in a great number of products ranging from recreational equipment to industrial robotics.

Advanced composites offer numerous advantages over conventional materials. Among these are the following [Advanced Composites Group, 1999]:

- Extended life cycle. Composites offer excellent fatigue life and very good resistance to environmental degradation and corrosion. Furthermore, composites can have outstanding impact resistance.
- High strength and stiffness. The high specific modulus and strength of composites enables the construction of very strong and stiff structures, with substantial weight savings.
- Design efficiency. Composite structures can be designed to give exacting performance characteristics. By aligning fiber orientation with the direction of principle stresses, the designer can maximize structural efficiency.

Advanced composites thus offer the advantages of lower weight, higher stiffness, greater strength, and improved durability.

Advanced composite materials consist of two principal components: reinforcing fibers and a homogeneous resin matrix. The following sections describe these components in detail.

### 2.1.1. Reinforcing Fibers

The reinforcing fibers in advanced composites provide the material's high strength. The percentage of fibers (by volume) in the material is typically 10 to 60 percent [Kalpakjian, 1997].

Reinforcing fibers are most commonly made of glass, carbon, aramid, polyethylene, or boron. Glass fibers are the most frequently used and least expensive of the fibers. Carbon has higher strength and stiffness values but is more expensive. Aramid fibers (commonly marketed under the trade name Kevlar®) are among the toughest fibers available and are normally applied to areas where there is a likelihood of impact. Like Kevlar, polyethylene (also known as Spectra®) can absorb and dissipate energy well and is commonly used in impact areas. It is lighter than Kevlar, but it is also more expensive and has a relatively low melting point. Boron fibers exhibit high strength and stiffness and are resistant to high temperatures, but they have a high density and are expensive.

The fibers in advanced composites may be randomly dispersed in the resin matrix or may be aligned in specific orientations. When all the fibers in the material are oriented along a single direction, the material is termed a uni-directional composite or uni-directional tape. Alternatively, fibers may be woven together to form a cloth-like fabric that has reinforcement fibers oriented in multiple directions. These composite fabrics are available in numerous different weave patterns based on the particular configuration in which fibers are interlaced with one another. Three of the more common weave patterns are illustrated in Figure 2.1 below.

The *plain weave* (Figure 2.1a.) is an “over-under” pattern in which fibers pass alternatively above and below each other. A *twill weave* is constructed of fibers passing above and below a particular number of cross fibers. For example, a 2x2 twill (Figure 2.1b) has fibers passing over two fibers and then under two fibers. Adjacent fibers are offset by one cross fiber, and this creates a “herring bone” or

diagonal pattern in the fabric. The *satin weave* consists of fibers passing over a particular number of cross fibers and then under one cross fiber. For example, a 5 harness satin weave has fibers passing over four fibers and then under one, as illustrated in Figure 2.1c.

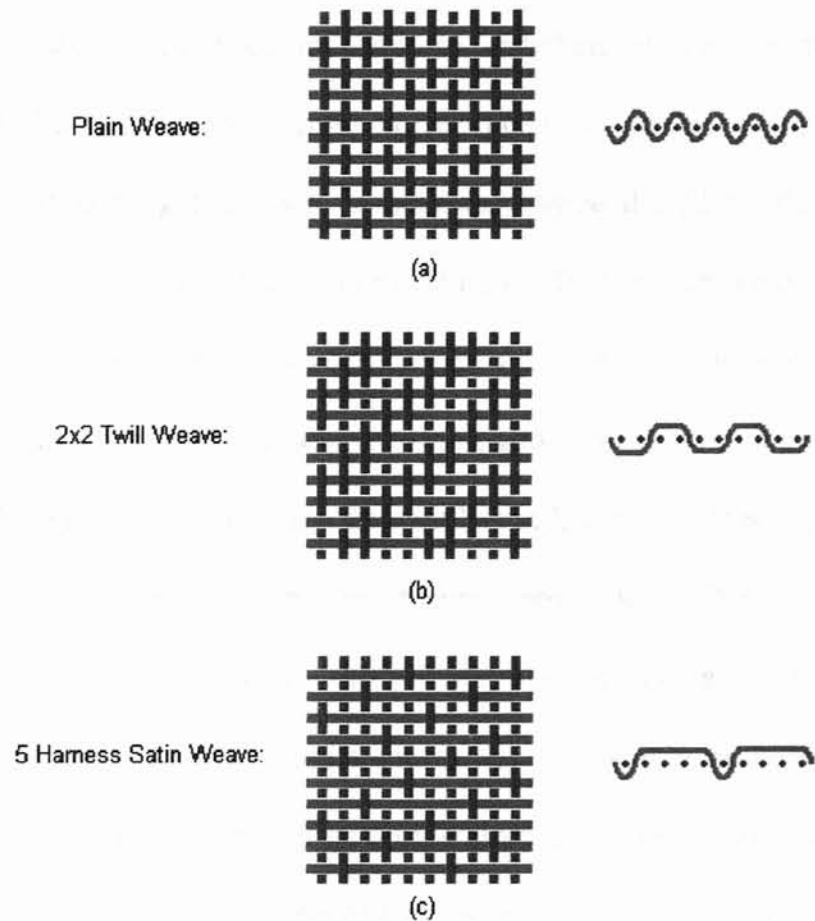


**Figure 2.1: Common weave patterns of carbon fiber fabric [Advanced Composites Group, 1999].**

In this research effort, two different composite fabrics were utilized: a 2x2 twill and a plain weave. The reinforcing fibers in both fabrics were carbon.

### 2.1.2. Resin Matrix

The resin matrix in advanced composite materials has two main functions:

- Support the fibers and transfer load from one fiber to the next.
- Protect the fibers against physical damage and the environment.

Transferring loads is important in order to distribute stresses in the material. Supporting the fibers keeps them in the correct position and orientation to carry the applied load. Protecting the fibers is necessary since the fibers themselves are generally brittle and may be sensitive to moisture or other contaminants.

Several different resin types are commonly used in composites. The most frequently used are epoxy resins, which exhibit good corrosion resistance and high toughness. Polyester resins are also frequently used; they are less expensive than epoxies but do not have as good mechanical properties. Phenolic resins are commonly used when fire resistance is a primary concern (i.e., aircraft interiors); in a fire they give off less smoke and toxic fumes than epoxy or polyester resins. Cyanate ester resins are found in high-temperature applications; although they are expensive, they can retain their mechanical properties at extremely high service temperatures.

The two composite materials in this research effort both utilized epoxy resin systems.

## 2.2. Rapid Prototyping

Rapid prototyping (RP), also known as solid freeform fabrication (SFF), refers to a set of manufacturing processes for producing complex solid objects

directly from a computer model without part-specific tooling or final assembly. These processes are often categorized based on the initial form of their materials, and as such they can be classified as (1) liquid-based, (2) solid-based, or (3) powder-based systems [Kai & Fai, 1997].

Liquid-based rapid prototyping systems begin with a liquid photocurable resin and build the desired three-dimensional object using laser radiation (usually in the ultraviolet range) to solidify the resin layer-by-layer. An example of this method is the stereolithography process commercialized by 3D Systems. Solid-based rapid prototyping utilizes solid material in the form of wire, pellets, or rolls as its starting material; the desired three-dimensional object is produced using processes analogous to extrusion, lamination, or ink-jet printing. Examples of solid-based RP include Fused Deposition Modeling (FDM), Laminated Object Manufacturing (LOM), and Multi-Jet Modeling (MJM). Finally, powder-based rapid prototyping systems begin with powder (in grain-like form) and employ a laser or glue-like adhesive to bind the grains into the desired solid object. Examples include Selective Laser Sintering (SLS) and 3-Dimensional Printing (3DP).

This research effort utilizes products made by two of the above methods, stereolithography and Fused Deposition Modeling. The following sections discuss these technologies in greater detail.

### 2.2.1. Stereolithography

Stereolithography (SL) was developed in the mid-1980's by inventor Charles Hull. The first Stereolithography Apparatus (SLA) for producing SL parts was marketed in 1988 by Hull's company, 3D Systems [3D Systems, 2002].

The stereolithography process begins with a three-dimensional CAD model of the desired object. The CAD model is then tessellated, approximating the surfaces of the solid model with triangles, and saved as a **STereoLithography (STL)** file. The STL file is essentially a list of the x, y, z coordinates of each triangle's three vertices, along with an index describing the orientation of the surface normal [Jacobs, 1996]. The geometry described by the STL file is then "sliced" horizontally into cross-sections (typically 10-20 cross-sections/millimeter) and saved as a **SLIce (SLI)** file that will guide the SLA's laser as each layer of the object is built.

Fabrication of the solid object takes place in a Stereolithography Apparatus. This machine initially contains a vat of liquid photopolymer, with an elevator platform slightly below the surface of the liquid. The first (bottom) layer of the part is built on the platform, along with any auxiliary support structures needed to stabilize the part, by directing a focused ultraviolet laser downward onto the surface of the liquid. Computer-controlled mirrors aim the laser so that it traces the desired geometry, and the photopolymer cures (solidifies) where it is illuminated by the UV laser. After the first layer is completed, the elevator platform moves downward by the height of one layer. Liquid resin flows over the solidified layer, and a recoater blade moves across the surface to remove excess resin. The second layer of the part is then traced by the laser, solidifying in contact with the previous layer. This

process continues, adding to the structure layer-by-layer, until the entire three-dimensional object has been fabricated, from bottom to top [Kietzman, 1999].

The completed part is then raised out of the vat, and excess resin is drained off. Any remaining uncured resin is cleaned off the part using a solvent, and the solid support structures are carefully removed. Finally, the object is placed in a postcure chamber, where it is flooded with ultraviolet radiation to achieve full resin strength [Jacobs, 1996].

### 2.2.2. Fused Deposition Modeling

Fused Deposition Modeling (FDM) was developed at Stratasys, Inc., in the late 1980's. The process was patented and commercialized by Stratasys in 1992 [Stratasys, Inc., 2002].

Like stereolithography, the FDM process begins with a three-dimensional CAD model of the desired object. This model is converted to an STL file (or, alternatively, to an Initial Graphics Exchange Specifications, IGES, file) for processing by Stratasys QuickSlice® software. QuickSlice® slices the model into horizontal layers (typically 10-20 layers/millimeter), and a companion software, SupportWork™, detects and generates any necessary support structures [Kai & Fai, 1997].

The FDM fabricator uses spools of thermoplastic filament as its starting material. The filament is fed into an extrusion head, where it is heated to just above its flow point. As the head is guided in the x-y plane by a control computer reading the QuickSlice files, the molten thermoplastic is extruded through a nozzle and



deposited on demand. The material cools and quickly solidifies as it exits the nozzle, forming a layer of the part. As with stereolithography, the object is built upon a platform or table which lowers as each layer is completed. In this way, the FDM process builds parts from bottom to top in a layer-by-layer additive fashion [Jacobs, 1996].

The extrusion head is actually a dual-tip mechanism that can dispense two modeling materials simultaneously. Often, the desired part is built from one material, and any auxiliary support structures are constructed of a secondary material. After the object is completely built, the supports can be easily snapped off because the bond between the two materials is relatively weak. However, the recent introduction of water-soluble support materials has made this post-processing even easier, as the supports can simply be washed away, leaving the desired part.

### 2.3. Finite Element Analysis

Finite element analysis (FEA) is a powerful tool for obtaining the numerical solution of a wide range of problems in engineering and mathematical physics. Typical areas of application for FEA include structural analysis, heat transfer, fluid flow, mass transport, and electromagnetic potential [Logan, 1993].

For many real life systems, finding an exact (analytical) solution is not possible. An exact solution generally involves the solution of ordinary or partial differential equations, and this is often unobtainable for complicated structures or boundary conditions. Finite element analysis, however, models the solution region by dividing it into an equivalent system of smaller regions (finite elements)

interconnected at nodes. The governing differential equations for each element are then replaced by algebraic approximations, and the problem reduces to solving a system of simultaneous algebraic equations rather than solving the governing differential equations over the entire region.

The essential ideas of finite element analysis began to appear in literature in the 1940's. In 1941, Hrenikoff proposed that the elastic behavior of a continuous plate would be similar, under certain loading conditions, to a framework of physically separate one-dimensional rods and beams, connected together at discrete points [Hrenikoff, 1941]. Two years later McHenry further refined the idea of using one-dimensional elements to solve for the stresses in continuous solids [McHenry, 1943]. Also in 1943, Courant proposed breaking a continuous region into triangular segments and using piecewise interpolation (or shape) functions over the subregions to model torsion problems in elasticity [Courant, 1943]. In 1955, Argyris took the well-established framework-analysis procedures and reformulated them into a matrix format ideally suited for newly-introduced digital computers [Argyris, 1955].

The first use of two-dimensional elements was by Turner, Clough, Martin, and Topp in 1956 [Turner, et al., 1956]. They analyzed aircraft wing panels using an assemblage of simple triangular panels, and they derived stiffness matrices for triangular and rectangular plane stress elements as well as truss and beam elements. The term "finite element" was first introduced by Clough in 1960 when he used both triangular and rectangular elements for plane stress analysis [Clough, 1960].

Finite element analysis was first applied to three-dimensional problems with the development of a stiffness matrix for tetrahedral elements in 1961 [Martin,

1961]. Additional types of three-dimensional elements were studied by Argyris in 1964 [Argyris, 1964].

Finite element analysis of non-structural problems was first presented in 1965 when Zienkiewicz and Cheung applied the method to field problems [Zienkiewicz, et al., 1965]. Finite elements could then be used to solve problems in fluid flow and heat transfer. More recently, finite element analysis has been applied to nonlinear problems, large-displacement behavior, and electric fields, with new areas of application still being discovered [Logan, 1993].

### 2.3.1. Implementation of FEA

The general steps of the finite element method are presented in this section. For simplicity, we focus our discussion on the structural stress-analysis problem and assume we are performing a two-dimensional (plane stress) analysis. However, the ideas presented here are analogous to those used to solve non-structural (i.e., heat transfer and fluid mechanics) problems, and the equations can readily be extended into three dimensions.

- Step 1 of the finite element method is to divide the solution region into subdivisions or elements. For example, if our analysis involved the thin plate shown in Figure 2.2a below, we might discretize the region using triangular elements as shown in Figure 2.2b. Alternatively, we could use four-sided quadrilateral elements, or for a three-dimensional analysis we could use tetrahedra, bricks, or wedges.

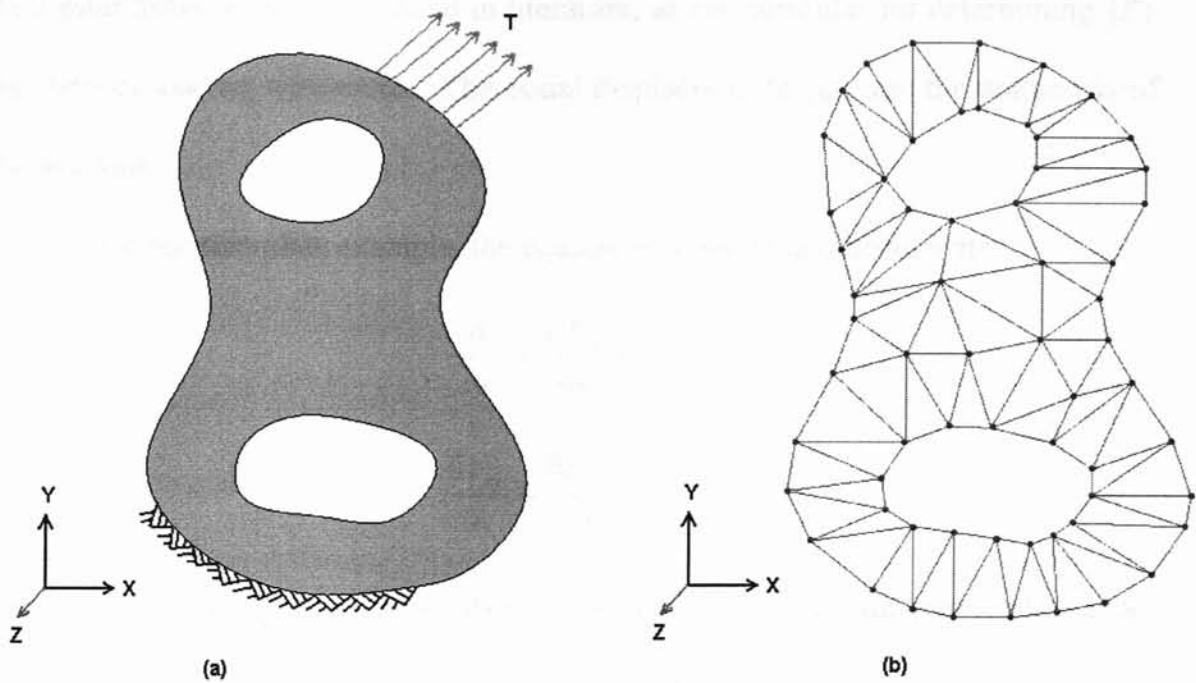


**Figure 2.2: Thin plate discretized using triangular elements.**

- Step 2 is the development of *element equations* – algebraic approximations of the system’s governing equations, applicable to each element. The system’s governing equations are often differential equations expressing a conservation or balance of some physical property such as mass, momentum, or energy. They may also be integral equations expressing a variational principle, such as the minimization of potential energy for conservative mechanical systems [Burnett, 1987].

Deriving element equations from the governing equations is an exercise in finite element theory and is the focus of many finite element textbooks. These element equations are often expressed in matrix form as  $[k^e]\{q^e\} = \{f^e\}$ , where  $[k^e]$  represents the stiffness matrix of element  $e$ ,  $\{q^e\}$  is the vector of nodal displacements, and  $\{f^e\}$  is the vector of nodal forces. The stiffness matrices for common types of elements (triangles, quadrilaterals, tetrahedra, bricks, etc.) are

well-established and can be found in literature, as can formulas for determining  $\{f^e\}$  for various loading conditions. The nodal displacements  $\{q^e\}$  are the unknowns of the analysis.

For our thin plate example, the equations of stress equilibrium are

$$\begin{aligned}\frac{\partial \sigma_x}{\partial x} + \frac{\partial \tau_{xy}}{\partial y} &= -f_x \\ \frac{\partial \tau_{xy}}{\partial x} + \frac{\partial \sigma_y}{\partial y} &= -f_y\end{aligned}\tag{Eq. 1}$$

where  $\sigma_x$ ,  $\sigma_y$ , and  $\tau_{xy}$  are components of stress, and  $f_x$  and  $f_y$  are internal loads that act on every material point inside the plate (such as gravity).

The constitutive relations (stress-strain equations) that describe the material's elastic response are

$$\begin{aligned}\sigma_x &= \frac{E}{1-\nu^2} \varepsilon_x + \frac{E\nu}{1-\nu^2} \varepsilon_y \\ \sigma_y &= \frac{E\nu}{1-\nu^2} \varepsilon_x + \frac{E}{1-\nu^2} \varepsilon_y \\ \tau_{xy} &= \frac{E}{2(1+\nu)} \gamma_{xy}\end{aligned}\tag{Eq. 2}$$

where  $\varepsilon_x$ ,  $\varepsilon_y$ , and  $\gamma_{xy}$  are components of strain, and  $E$  and  $\nu$  are the material's Young's modulus and Poisson's ratio.

Finally, the strain-displacement relations that describe the purely geometric aspects of the deformation are

$$\begin{aligned}\varepsilon_x &= \frac{\partial u}{\partial x} \\ \varepsilon_y &= \frac{\partial v}{\partial y}\end{aligned}\tag{Eq. 3}$$

$$\gamma_{xy} = \frac{\partial u}{\partial y} + \frac{\partial v}{\partial x}$$

where  $u$  and  $v$  are components of displacement in the  $x$ - and  $y$ -directions, respectively.

Combining Equations 1 through 3 yields two second-order partial differential equations which are the governing equations for our problem:

$$\frac{E}{1-\nu^2} \frac{\partial^2 u}{\partial x^2} + \frac{E}{2(1-\nu)} \frac{\partial^2 v}{\partial x \partial y} + \frac{E}{2(1+\nu)} \frac{\partial^2 u}{\partial y^2} = -f_x$$

Eq. 4

$$\frac{E}{1-\nu^2} \frac{\partial^2 v}{\partial y^2} + \frac{E}{2(1-\nu)} \frac{\partial^2 u}{\partial x \partial y} + \frac{E}{2(1+\nu)} \frac{\partial^2 v}{\partial x^2} = -f_y$$

The governing equations are approximated by element equations which can be written in the form

$$\begin{bmatrix} k_{11} & k_{12} & \cdots & k_{16} \\ k_{21} & k_{22} & \cdots & k_{26} \\ \vdots & \vdots & & \vdots \\ k_{61} & k_{62} & \cdots & k_{66} \end{bmatrix} \begin{bmatrix} q_1 \\ q_2 \\ \vdots \\ q_6 \end{bmatrix} = \begin{bmatrix} f_1 \\ f_2 \\ \vdots \\ f_6 \end{bmatrix}$$

Eq. 5

We can compute values for  $k_{ij}$  and  $f_i$  using formulas derived in finite element texts. The coefficients  $k_{ij}$  are related to the partial derivative terms in the governing equations and can be computed from the Young's modulus, Poisson's ratio, and nodal coordinates of an element. The values of  $f_i$  are related to the internal loads  $f_x$  and  $f_y$  in the governing equations and can be computed from knowledge of the body forces, traction loads, and point loads acting on the element.

- Step 3 is to assemble the individual element equations generated in Step 2 into a “global” set of equations which characterizes the response of the entire system. This can be done using a method of superposition and often results in a very large number of equations. The global equations are often expressed in matrix form as

Eq. 6

$$[K] \{Q\} = \{F\}$$

where  $[K]$  represents the global stiffness matrix,  $\{F\}$  is the global force vector, and  $\{Q\}$  is a vector of unknown nodal displacements.

Our thin plate shown in Figure 2.2 would involve relatively few global equations because it is meshed with so few elements, but a more complicated problem could easily yield more than one million equations in the global set.

- Step 4 requires us to modify the global equation set to account for boundary constraints. Physically, these constraints prevent rigid body motion of the structure. Mathematically, they change  $[K]$  from a singular matrix to a nonsingular matrix so that the global equation set is solvable.

The thin plate in Figure 2.2 is constrained along its lower boundary. The displacement of all nodes on this portion of the boundary is therefore taken as zero, and the corresponding displacement variables can be eliminated from the global equation set.

- Step 5 is the solution of the global equation set to determine the nodal displacements  $\{Q\}$ . This can be done using conventional numerical analysis techniques for solving linear systems.

- Step 6 involves the computation of stress, strain, and any other quantities of interest. These can be computed from the displacements determined in Step 5 using the necessary equations of solid or structural mechanics.

For our thin plate example, the strains  $\varepsilon_x$ ,  $\varepsilon_y$ , and  $\gamma_{xy}$  for each element can be computed from the element's nodal displacements, and the corresponding stresses can then be calculated as

$$\begin{aligned}\sigma_x &= \frac{E}{1-\nu^2} (\varepsilon_x + \nu\varepsilon_y) \\ \sigma_y &= \frac{E}{1-\nu^2} (\nu\varepsilon_x + \varepsilon_y) \\ \tau_{xy} &= \frac{E}{2(1+\nu)} \gamma_{xy}\end{aligned}\tag{Eq. 7}$$

In summary, we see that the finite element method is one in which a continuous quantity, such as the displacement throughout a body, is approximated by a discrete model composed of a set of piecewise-continuous functions defined within each finite element [Logan, 1993].

### 2.3.2. The H-Method and the P-Method

The finite element method can be subdivided into two categories based on the nature of the elements used. The first category, known as the *h-method*, relies on first-order interpolating polynomials (also called shape functions) to describe the internal behavior (i.e., deflection) of an element. The second category, called the *p-method*, utilizes higher-order polynomials to characterize an element's internal



behavior, thereby enabling an element to more accurately capture gradients and other complexities of the field variable [Parametric Technology Corporation, 1999].

The h-method is considered the more traditional approach because it was the technique implemented in the earliest commercially available finite element software programs. Although the mathematical theory behind the p-method was developed about the same time, digital computers at that time were only able to do the computations necessary to solve problems using the h-method. As the processing power of computers later increased, it became possible and practical to solve problems using the p-method.

The following sections discuss the two different methods in more detail and discuss some advantages of using a p-method solver.

#### 2.3.2.1. The H-Method

As mentioned previously, the h-method uses first-order interpolating polynomials to describe the behavior of an element. In order to achieve accurate results for a problem, an FEM analysis based on the h-method usually requires a relatively dense mesh of very tiny elements.

To illustrate this, consider the cantilever beam shown in Figure 2.3a below. The deflection of the beam (based on conventional beam theory) is a third-order function of the horizontal position, as illustrated in Figure 2.3b.



**Figure 2.3: Cantilever beam with end load.**

If we analyze the beam using a single h-element, the resulting deflection would be as shown in Figure 2.4a. We clearly need additional elements to accurately portray the deflection along the length of the beam.

If we use two h-elements to analyze the beam, the deflection is closer to the theoretical solution (see Figure 2.4b), but the beam's behavior is still somewhat unrealistic. For example, we see a discontinuity at the center of the beam, and we see rotation of the beam at its cantilevered end.

We can achieve a better solution by using three h-elements (Figure 2.4c), and even better by using four h-elements (Figure 2.4d). We see that using more elements improves the solution, but an infinite number of elements would be required to exactly match the third-order closed-form solution for the deflection.

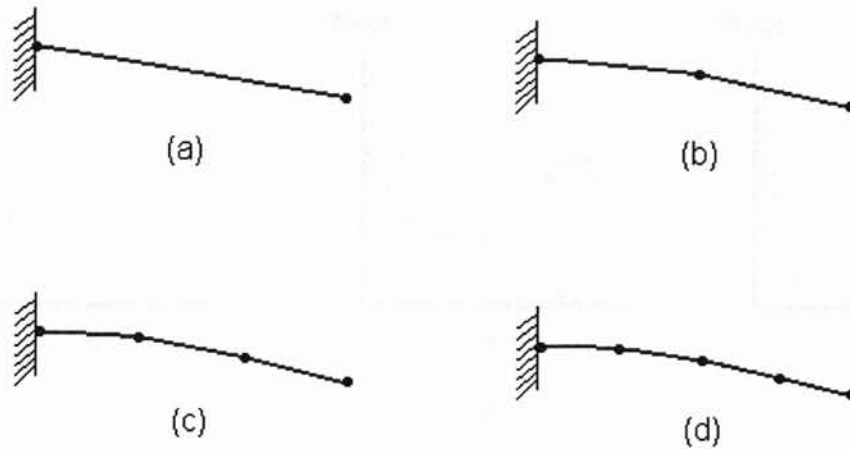


**Figure 2.4: Using h-elements to model the cantilever beam.**

The process of decreasing element size in order to improve accuracy is known as h-convergence. When successively finer element meshes produce negligible change in the results, we conclude that the analysis has converged to an accurate solution.

As an alternative example of using h-elements in FEA, suppose we are modeling a structure within which the stress varies as shown in Figure 2.5a.

Using h-elements, the displacement in any given element is a linear function of position. The strain throughout the element is therefore constant (since strain is computed as the derivative of displacement), and the stress in the element (computed from constitutive relations) is also constant. H-elements would therefore model the stress distribution as shown in Figure 2.5b - as a series of constant, discontinuous stresses. Reducing element size would improve the accuracy of the stress values (see Figure 2.5c), but the FEM analysis would still yield discontinuous stresses throughout the structure and would fall short of predicting the highest stress.

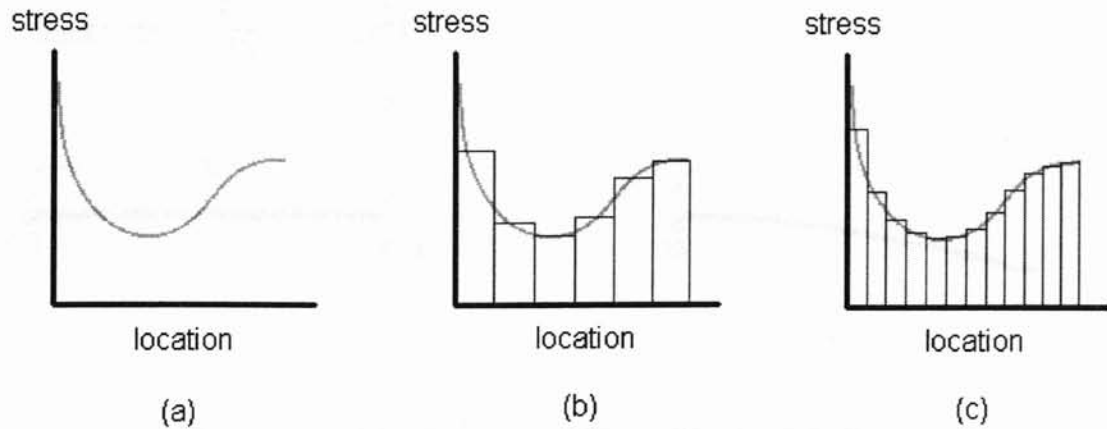


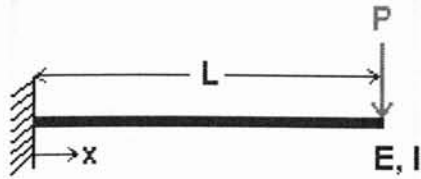
**Figure 2.5: Using h-elements to model a stress distribution.**

### 2.3.2.2. The P-Method

Unlike the h-method, which uses linear shape functions and relies on mesh refinement to improve the results, the p-method allows for increasing the internal mathematical complexity of the elements to achieve better solution accuracy. In the p-method, convergence to an accurate solution is pursued by increasing the order of the polynomial shape function within each element rather than repeatedly remeshing the problem with smaller elements [Parametric Technology Corporation, 1999].

Consider again our cantilever beam example (shown again in Figure 2.6a). We have already seen that modeling the problem with a single first-order element produces poor results. Suppose, though, that we now use a p-element, and the deflection of the element is represented by a second-order shape function. The deflected shape of the element would more closely resemble the true curvature of the beam and would avoid the unrealistic discontinuities observed in the h-element analyses. If our p-element instead employs a third-order shape function, we would capture the true deflected shape exactly, as shown in Figure 2.6b below.

$$\text{deflection} = \frac{P}{6EI}(x^3 - 3Lx^2)$$



(a)



(b)

**Figure 2.6: Using one p-element to model the cantilever beam.**

If we were to repeat this analysis using fourth-order and higher shape functions, we would observe that increasing the polynomial order does not change our FEM solution. We would therefore conclude that the third-order shape function had accurately captured the results.

Hence, in the p-method convergence is obtained by increasing the order of the shape functions on each element. The mesh stays the same for every iteration, called a p-loop pass, and we conclude that our finite element analysis has converged when successively higher polynomial orders produce negligible change in the results [Toogood, 2001].

Suppose now that we are trying to capture the stress distribution discussed in the previous section and illustrated again in Figure 2.7a. Recall that first-order elements (h-elements) represented the stress distribution as a series of constant, discontinuous stresses. If we instead use p-elements with second-order shape functions, then the stress distribution within each element varies linearly, and our model (still with relatively few elements) provides a much better representation of the stress distribution (see Figure 2.7b). If we use higher-order p-elements, we can capture the stress distribution exactly, as depicted in Figure 2.7c.

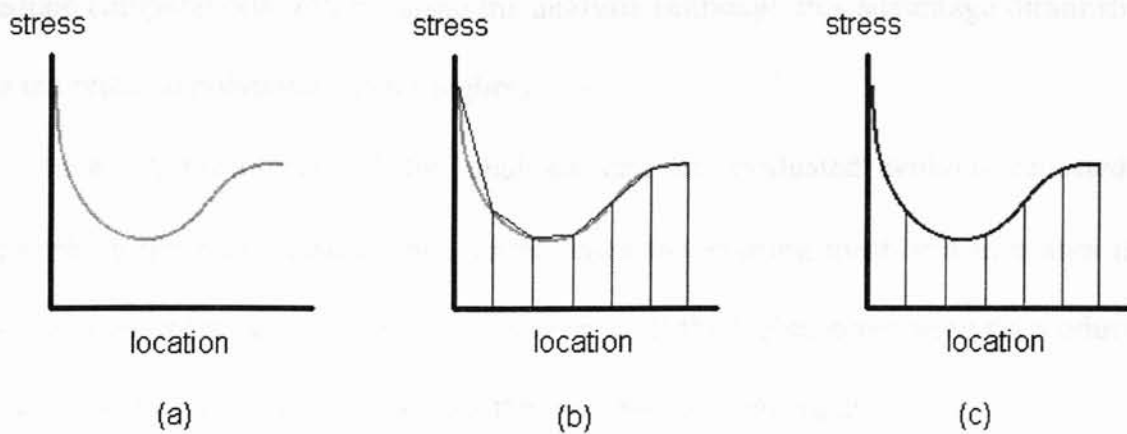


**Figure 2.7: Using p-elements to model a stress distribution.**

### 2.3.2.3. Advantages of the P-Method

As described previously, p-method finite elements can embody considerably more mathematical complexity than their h-method counterparts. Because of this capability, there are several advantages in using the p-method of finite element analysis [Toogood, 2001].

- Limits on element size and shape are not nearly as restrictive for p-elements as they are for h-elements. P-elements are allowed to exhibit greater aspect ratio, skewness, and so on because they can capture more complex behavior over a given distance. This is particularly beneficial when utilizing automatic mesh generators to produce the finite element mesh. [These mesh generators can produce very poor meshes for h-elements but tend to be much more effective with p-elements.]
- In general, fewer higher-order elements are needed to achieve the same degree of accuracy in the final results. This means that the finite element mesh for a problem can be more coarse than a corresponding mesh of h-elements, and this can

reduce computational effort during the analysis (although this advantage diminishes as the order of polynomials gets higher).

- Convergence of the analysis can be evaluated without repeatedly remeshing the part. Instead, one simply uses the existing mesh and increases the polynomial order associated with the elements. If the higher-order analysis produces negligible change in the results, then the analysis has converged.

## 2.4. Pro/MECHANICA

Pro/MECHANICA is a suite of engineering analysis tools provided by Parametric Technology Corporation (PTC). In addition to the structural finite element analysis package utilized in this research effort, Mechanica also embodies tools to analyze the dynamic and thermal performance of mechanical systems. Within Pro/MECHANICA, there are two basic modes of operation: independent mode and integrated mode. Choosing which operating mode to use essentially determines how closely Mechanica interacts with its cousin application, Pro/ENGINEER. The difference between the two modes is described in the following section.

### 2.4.1. Integrated Mode and Independent Mode

Integrated mode permits the use of Pro/MECHANICA functionality from within the Pro/ENGINEER user interface. This mode offers a seamless transition from the Pro/E solid modeling engine to the Pro/M finite element engine and back again. Furthermore, any changes that are made to the model in Mechanica (i.e.,

during an optimization study) are automatically updated in Pro/E and in any downstream deliverables (engineering drawings, CNC machine toolpaths, etc.) This provides a truly integrated design analysis software in which a model can be created, analyzed, and optimized, all from a single user interface.

Independent mode, on the other hand, incorporates a user interface that is quite different from the Pro/E environment. Upon invoking independent mode, all ties with Pro/E are severed. Therefore, any changes made to the model in Mechanica have no effect on the Pro/E part or downstream deliverables. These changes must be manually updated by re-opening the model in Pro/E and making the necessary modifications.

Unfortunately, a few Mechanica commands and result displays are not yet available in integrated mode. Thus, independent mode offers the widest range of Pro/MECHANICA functionality. However, PTC is constantly working to migrate the functionality of independent Mechanica into integrated mode, and with each new release the integrated mode comes closer to offering all of Mechanica's standalone functionality [Parametric Technology Corporation, 2002].

For this research effort, integrated mode was selected as the preferred mode of operation in order to capitalize on the design functionality of both Pro/ENGINEER and Pro/MECHANICA.

#### 2.4.2. Convergence

Pro/MECHANICA utilizes the p-method of finite element analysis. As with other p-method solvers, Mechanica converges to an accurate solution by increasing



the internal mathematical complexity of elements during an analysis rather than repeatedly remeshing the problem with finer and finer meshes.

Mechanica uses polynomial shape functions to formulate the behavior of each element, and each shape function may, if necessary, increase up to a ninth-order polynomial during the analysis. [In theory, it would be possible to go to even higher orders than this, but Mechanica limits the polynomials to ninth-order functions because higher orders become too computationally expensive.]

At the beginning of an analysis, Mechanica assigns low-order shape functions to each element, and the finite element solution is computed. After this initial p-loop pass, polynomial orders are increased and a second p-loop pass is performed. Mechanica then evaluates the change in the solution using measures such as von Mises stress and displacement. By comparing these values on an element-by-element basis, Mechanica determines which elements in the model need to have more complex shape functions and which elements are adequately modeled by the current shape functions. Mechanica increases polynomial orders where necessary and then performs a third p-loop pass. This iterative process continues until all elements converge to a (user-defined) specified accuracy or until a maximum specified polynomial order is reached.

This process of performing multiple p-loop passes and adaptively (on an element-by-element basis) working toward convergence over the entire model is known in Mechanica as Multi-Pass Adaptive Convergence. By adaptively increasing the polynomial orders, Mechanica's finite element model is efficient to solve, while

accurately capturing the performance of the structure [Parametric Technology Corporation, 1999].

After running an analysis, we can assess the convergence of the model by graphing convergence measures as a function of p-loop pass. For example, if we graph the maximum von Mises stress and maximum displacement versus p-loop pass, the plots may appear as in Figure 2.8 below.

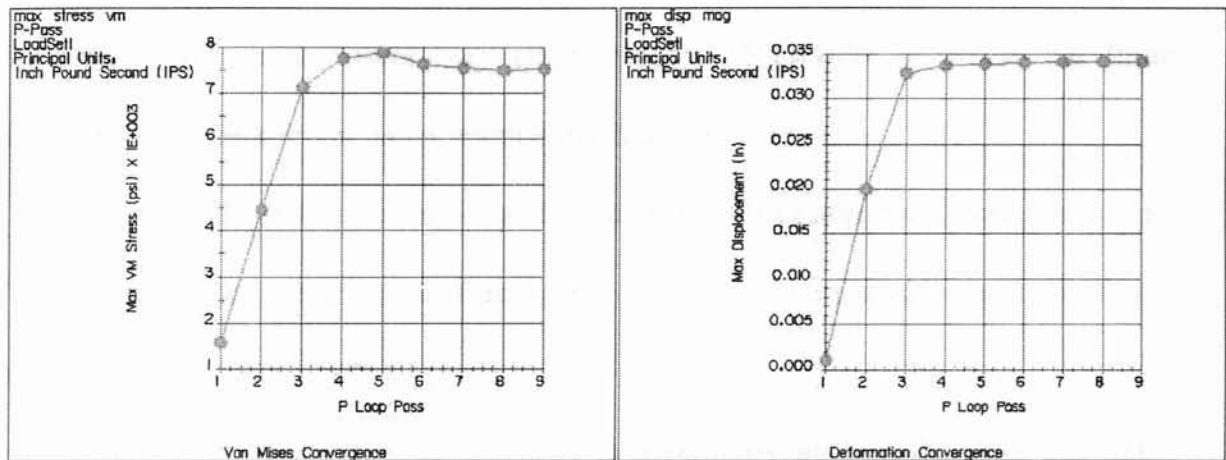


**Figure 2.8: Sample convergence plots from Pro/MECHANICA.**

The “leveling-off” of these graphs indicates that increased polynomial orders will cause little change in the results, and we can conclude that the solution is well converged.

An alternative convergence method, known as Single-Pass Adaptive Convergence, is also available in Mechanica but was not used in this research effort. This type of analysis begins with an initial pass where all p-orders are set to 3. Mechanica assesses the accuracy of the solution based on stress discontinuities at the element boundaries and computes the final p-order required for each element. A final solution pass is then made using these polynomial orders. Because this technique offers the user no intermediate results with which to evaluate solution

convergence, Single-Pass Adaptive Convergence was never used in this research effort.

### 2.4.3. AutoGEM

Pro/MECHANICA contains an automatic mesh generator called AutoGEM. In integrated mode, AutoGEM is always utilized to produce the finite element mesh. In independent mode, users may either employ AutoGEM or create the finite element mesh themselves using manual mesh-definition tools.

AutoGEM utilizes triangles and quadrilaterals to mesh two-dimensional (i.e., “shell”) geometry; tetrahedra, bricks, and wedges are commonly used for three-dimensional solid geometry.

Although generation of elements is essentially automatic, users can exert considerable influence on the size, shape, and density of the elements by modifying AutoGEM parameters that dictate allowable element geometry. For example, users can input minimum and maximum allowable angles between adjacent edges and between adjacent faces of elements (see Figures 2.9a and 2.9b). Users can also specify the maximum allowable edge turn (the maximum amount of arc to be allowed on an edge – see Figure 2.9c) and the maximum allowable aspect ratio (roughly an element’s length-to-width ratio).

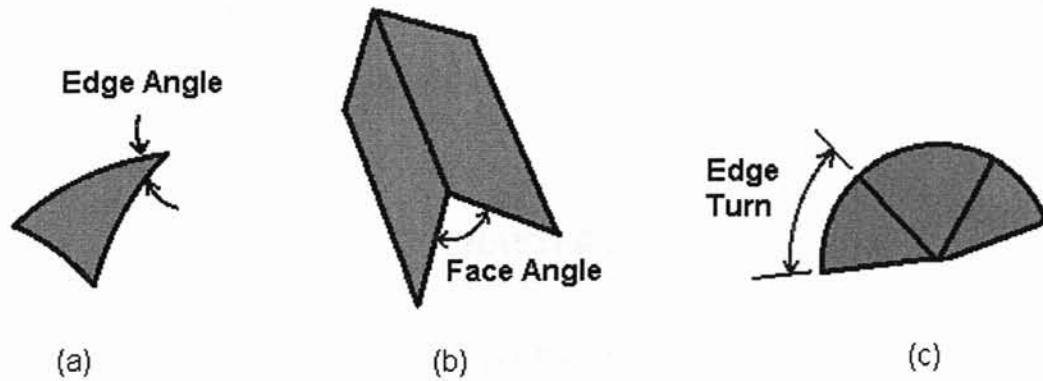


**Figure 2.9: AutoGEM parameters.**

Besides altering the AutoGEM parameters described above, users can also influence the mesh by adding datum points and surface regions to a model. Datum points are simply reference points that can be “seeded” on a model to guide mesh creation. When AutoGEM is executed, it will respect seed points as required locations for element nodes. Surface regions are reference features that divide a physical surface into multiple areas. AutoGEM will treat the boundaries of these surface regions as curves to which element edges must conform. Datum points and surface regions are used frequently in this research effort to influence the placement of element nodes and edges in order to tighten the mesh density in areas of particularly high stress gradients.

## CHAPTER 3

### METHODOLOGY

#### 3.1. Model Development

The initial goal in this research project is to develop a finite element model that simulates three-point bending tests conducted in OSU's mechanical engineering laboratories. These tests utilized an Instron 4202 Load Frame to apply a downward force to test specimens supported on a steel test fixture. The resultant loading condition is diagrammed in Figure 3.1 below.

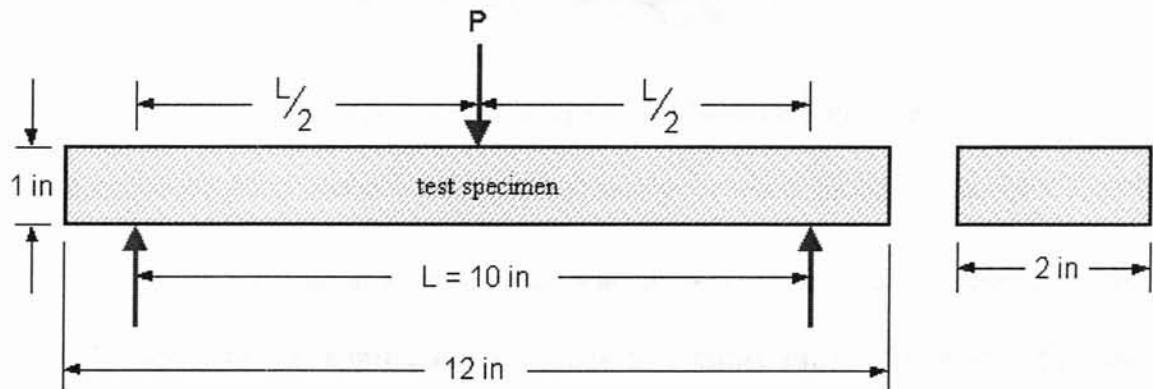


**Figure 3.1: Loading condition for three-point bending test.**

The actual loading points are 1.375-inch-diameter steel bars. In accordance with ASTM standards, steel loading pads are located between the loading bars and the test specimen to avoid localized crushing of the specimen, and a rubber pad is

placed underneath the mid-span steel pad to help distribute the applied load [ASTM C 393-00, 2000]. An exploded view of the experimental setup is shown in Figure 3.2.

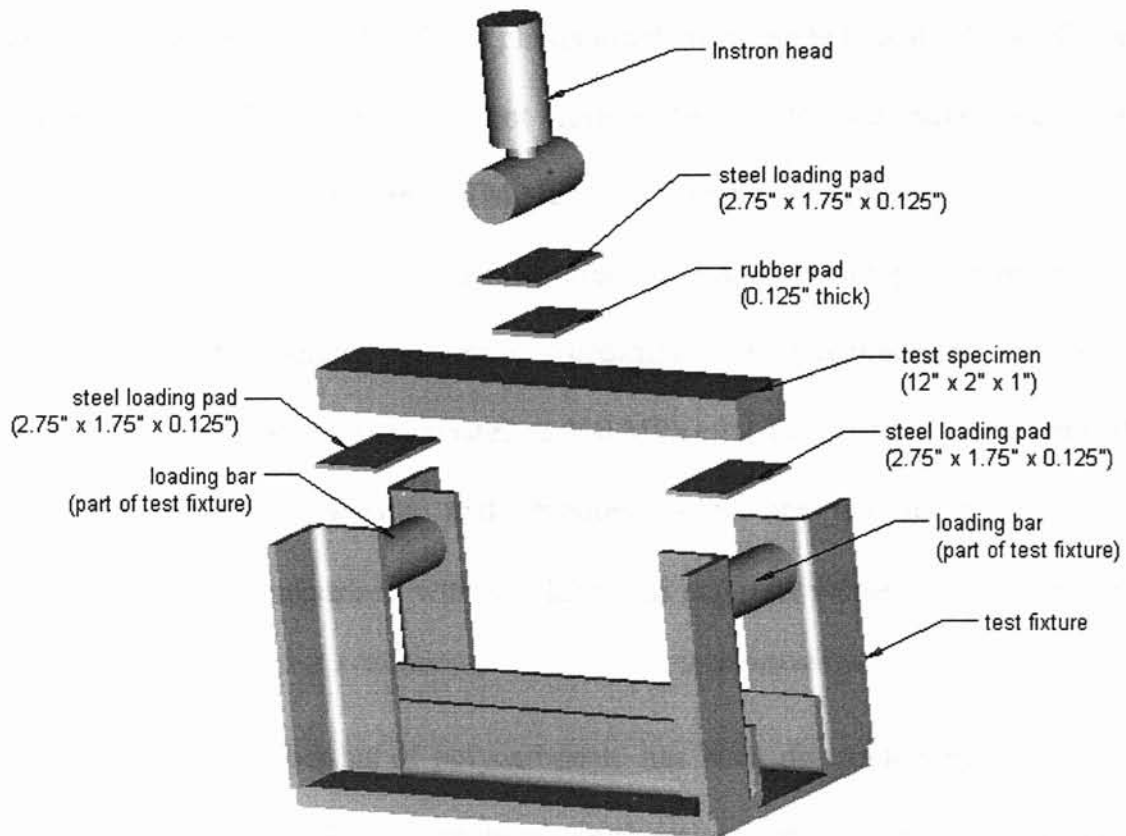


**Figure 3.2: Experimental setup for three-point bending test.**

Our finite element analysis needs to accurately model the test specimen and accurately simulate the application of loads and constraints. To model the test specimen's geometry, we simply construct a Pro/ENGINEER model that can be imported into Pro/MECHANICA. After entering Pro/M, we then assign material properties and specify the necessary loads and constraints. Material properties, loads, and constraints are discussed in more detail in the following sections.

### 3.1.1. Material Properties

The test specimens modeled in this research are composite beams having a polymer core sandwiched between carbon fiber facings. Two different polymers have been used as core materials: a photocurable resin known as RPC 700 ND, and polycarbonate. Also, two different carbon fiber materials have been used: LTM25 / CFS003 2x2 twill, and LTM26EL / CFS0508 plain weave.

RPC 700 ND resin is manufactured by Rapid Prototyping Chemicals, a subsidiary of 3D Systems Corporation. According to the manufacturer, the material has a tensile modulus of approximately 2,500 MPa after full post-cure (see Appendix A). The material's density and Poisson's ratio are not furnished by the manufacturer, but comparison with similar resins suggests values of  $\rho = 1.24 \text{ g/cm}^3$  and  $\nu = 0.38$ .

The tensile modulus of polycarbonate has been determined through tensile tests conducted in OSU's mechanical engineering laboratories; its value is approximately  $E = 2,350 \text{ MPa}$ . The Poisson's ratio of polycarbonate is estimated from material property tables to be approximately  $\nu = 0.38$  [Kalpakjian, 1997], and the density is assumed to be  $\rho = 1.24 \text{ g/cm}^3$  from comparison with similar materials.

Material properties for the LTM25 / CFS003 carbon fiber were acquired from NASA technical memorandum 110286 (see Appendix B). Properties used in our Pro/MECHANICA analysis are summarized in the following table, with reference to the coordinate directions shown in Figure 3.3.

**Table 3.1: In-plane properties of LTM25 / CFS003.**

$E_x^t$ , Young's modulus, tension (Msi)	7.06
$E_y^t$ , Young's modulus, tension (Msi)	7.06
$\nu_{xy}$ , Poisson's ratio, tension	0.042
$G_{xy}$ , in-plane shear modulus (Msi)	0.414
$t$ , thickness (in)	0.00904
$\rho$ , density (lbm/in <sup>3</sup> )	0.06

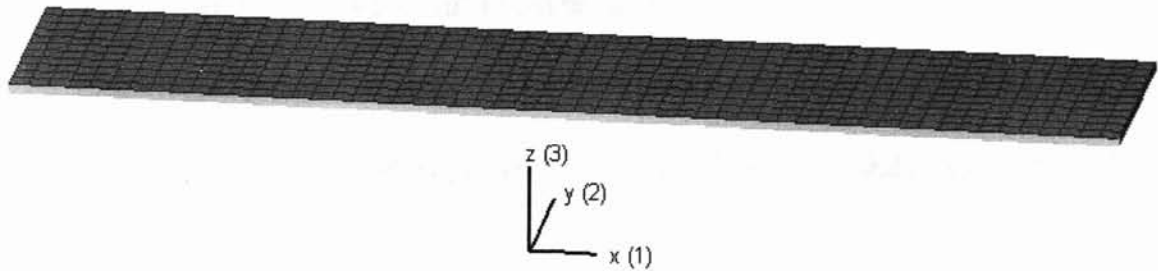


**Figure 3.3: Coordinate directions for laminate properties.**

Although material properties for the LTM26EL / CFS0508 plain weave are not directly available, it is reasonable to assume they are very similar to those of the 2x2 twill above. Both materials are woven fabrics with 3-K fibers (3,000 carbon filaments per fiber); the only substantial difference is the weave type (plain weave versus 2x2 twill). Manufacturers of the fabrics suggest that a plain weave may have a slightly lower modulus than a 2x2 twill, but data to quantify the difference is lacking. For this research, it is assumed that the properties in Table 3.1 apply to both carbon fiber materials.

Although not actually part of the test specimen, material properties of the rubber and steel components of the experimental setup will also be useful for our analysis.



The rubber is a neoprene-based sheet purchased from Texcel. Young's modulus can be computed from an expression published by Good [Good, 2002]:

$$E = 20.97 * e^{0.0564 * IRHD} \quad (psi)$$

where IRHD is the Shore A hardness of the material. Measurements of the rubber in this experiment indicate an average durometer of 73 (Shore A), suggesting a modulus of  $E = 1290$  psi. Good also reports an average Poisson's ratio for neoprene (among other rubber types) of  $\nu = 0.46$ . The density of the rubber is reported on Texcel data sheets as  $\rho = 1.42$  g/cm<sup>3</sup> [Texcel, 2002].

Material properties for steel can be used directly from the Pro/MECHANICA material database. These properties are  $E = 29 \times 10^6$  psi,  $\nu = 0.27$ , and  $\rho = 7.827$  g/cm<sup>3</sup>.

With the necessary material properties now established, we next consider the application of appropriate loads and constraints.

### 3.1.2. Boundary Conditions for 3-Point Bending Analysis

When establishing the boundary conditions for our analysis, we want to keep the model as simple as possible while still capturing the essence of the experimental loads and constraints.

Recognizing that our interest lies in the stresses and deflections of the composite beam test specimen, not in the steel test structure or Instron head, we want to only model and analyze components that directly impact the behavior of the test specimen. Modeling additional geometry would merely complicate the analysis and lengthen runtimes.

For this analysis, therefore, we model only the beam, loading pads, rubber pad, and a small portion of the test fixture (see Figure 3.4 below). With these components, it is believed that the experimental loads and constraints can be accurately simulated in the analysis, as described in the following sections.

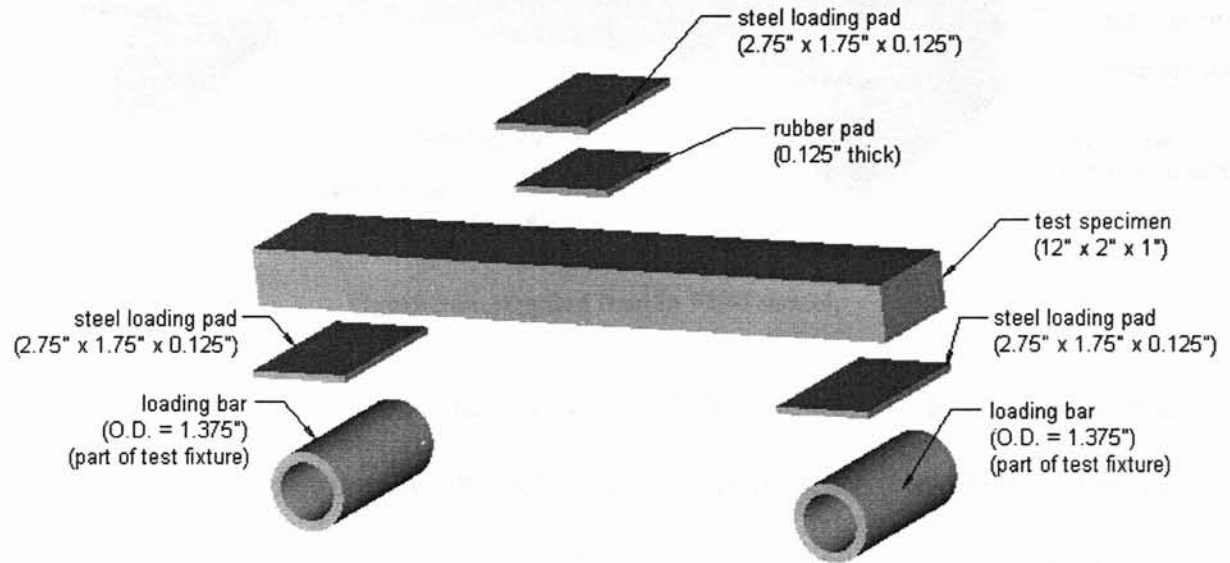


**Figure 3.4: Components in FEM model.**

### 3.1.2.1. Loads

The applied load is incorporated into the analysis as a uniform distributed load acting upon the top surface of the mid-span loading pad, as shown in Figure 3.5 below.

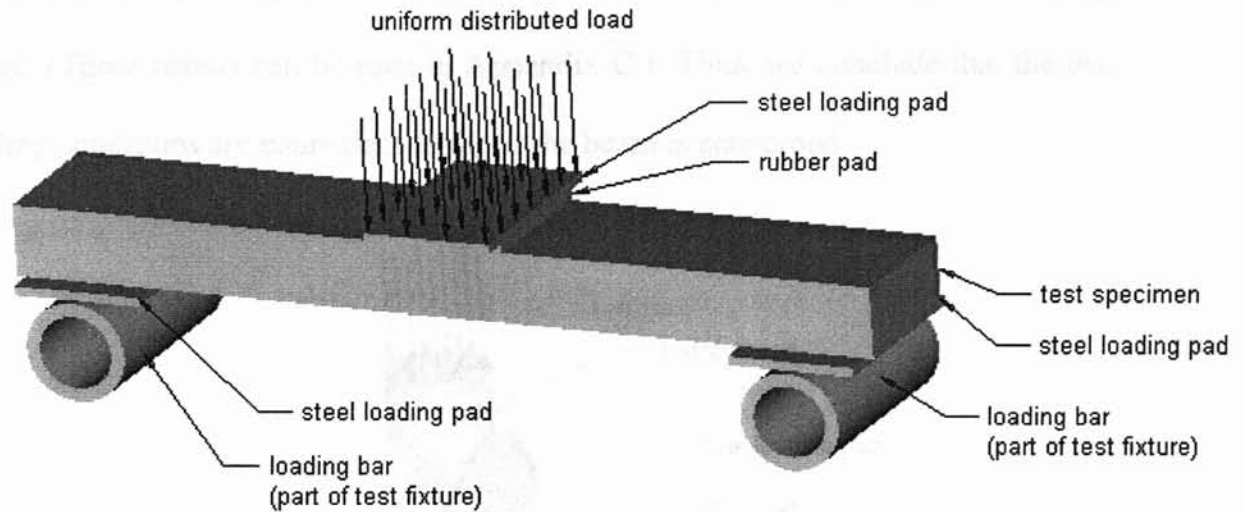


**Figure 3.5: Applied load in FEM model.**

Although this load distribution differs somewhat from the actual experimental load distribution, the difference will have negligible effect on the test specimen itself. Recall that the experimental load was actually applied to the loading pad via the 1.375-inch-diameter cylinder at the end of the Instron head. The load therefore acted upon a relatively small subregion of the loading pad and was more concentrated than portrayed in our FEM model. However, the loading pad and rubber pad distributed the applied load onto the test specimen, effectively dispersing any stress concentrations. Since our interest is in the stress and deformation of the composite beam (not the loading pad or rubber pad), the experimental loading condition should prove equivalent to the FEM model depicted in Figure 3.5.

To verify the equivalence of the two loading conditions, we employ a simple homogeneous beam as a test case. First, we analyze the beam's response to a uniform distributed load acting on the top loading pad as depicted in Figure 3.5. We then repeat the analysis but model the actual Instron head as the source of the applied load (see Figure 3.6 below). When we compare the beam's stress and

Recall from Figure 3.4 that our analysis models only the test specimen, loading pads, rubber pad, and a small portion of the test fixture. Specifically, the test fixture has been reduced to its two loading bars. (By excluding the remainder of the fixture, a much more efficient analysis is achieved.) We will now constrain these components in ways that simulate the physical constraints present in the system.

Since the test fixture is constructed of steel angle iron, we assume its deflection during the experiments is negligible and the loading bars are in effect rigidly supported. We therefore constrain the ends of the loading bars against all motion, as indicated in Figure 3.7.

We must now create two contact regions so that Mechanica will allow the loading pads to pivot on the loading bars during the analysis. Without contact regions, Mechanica would assume that all components are rigidly connected to one another, as if the entire assembly were one continuous solid. However, defining the contact region between a loading pad and its corresponding loading bar informs Mechanica that the two components are free to move apart. This enables the loading pad to pivot on the loading bar as occurs during the actual experiment.

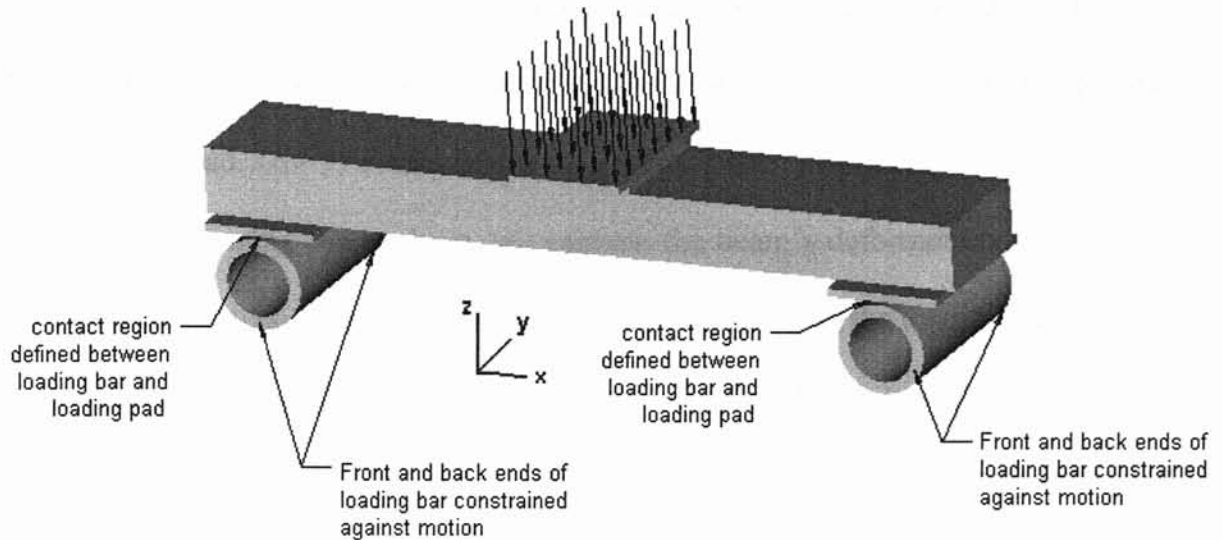


**Figure 3.7: Constraints for FEM model.**

Since contact regions enable relative motion between the fixed loading bars and the remainder of the structure, part of our model is now insufficiently constrained. In essence, the loading pads, rubber pad, and test specimen form a “subassembly” whose downward movement is restricted by the loading bars but whose lateral movement is unrestrained (contact regions are frictionless in Mechanics). In other words, the loading bars support the subassembly vertically, but there is nothing to prevent it from “sliding off” the loading bars laterally.

We therefore need to constrain the beam subassembly against motion in the x- and y-directions. A reasonable choice is to constrain the top surface of the mid-span loading pad in these directions, as this can represent the effect of frictional forces between the loading pad and the Instron head. Implementing this constraint gives us a fully-constrained model as desired.

To assess the appropriateness of our loading conditions and constraints before introducing a more difficult test specimen, we once again employ a simple

homogeneous beam as a test case. We assume the beam is constructed of RPC 700 ND photocurable resin, and we apply a 600-lbf uniform distributed load to the mid-span loading pad.

After running the analysis, we animate the beam's deformation and observe the beam bending downward while the loading pads pivot on the loading bars, just as we would expect. Furthermore, the stress distribution is consistent with our expectation for a beam in bending – a fringe plot of bending stress reveals tension in the lower half of the beam and compression in the upper half of the beam. (See Figure 3.8 below.)

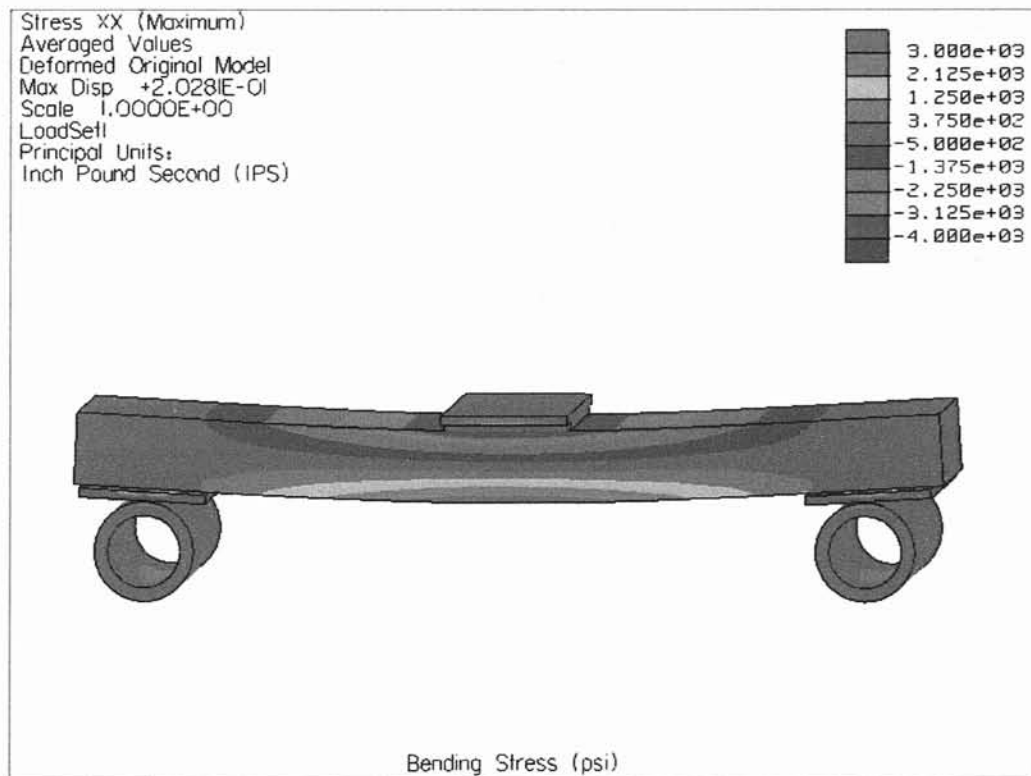


**Figure 3.8: Bending stress in deformed test specimen.**

The results indicate that we have chosen appropriate loading conditions and constraints. This is encouraging, but we are somewhat concerned by the runtime of the analysis. This test specimen was a simple rectangular beam, and yet it required

more than 50 minutes to complete. For more sophisticated test specimens, which may include multiple materials and complex internal structure, we could easily face runtimes on the order of hours or even days. We should therefore seek ways of simplifying the analysis in order to reduce the required computational effort.

The following sections investigate the use of symmetry and other means to simplify the analysis.

### 3.1.3. Use of Symmetry

There are two planes of symmetry in this model, as illustrated in Figure 3.9 below. The  $y$ - $z$  plane of symmetry divides the structure in half, producing a left side and right side that are mirror images of one another. Similarly, the  $x$ - $z$  plane of symmetry divides the model in half, producing a front side and back side that are mirror images. This section evaluates the effectiveness of using symmetry to simplify the analysis.

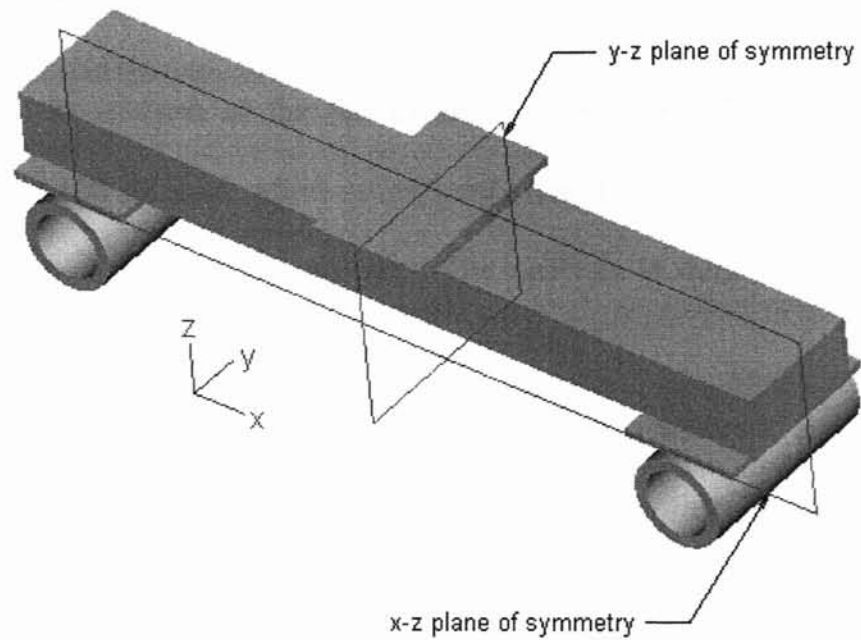


**Figure 3.9: Planes of symmetry.**

Before running our next analysis, the test specimen is made slightly more complicated by adding carbon fiber facings to the solid RPC 700 ND resin core. The facings are added to the top and bottom of the test specimen, and each facing consists of two layers of carbon fiber.

Each layer of carbon fiber is modeled in Pro/E as a solid protrusion of thickness 0.00904 inches. Because of the small thickness, it is necessary when setting up these analyses to alter the default AutoGEM settings. Specifically, the default Edge Angle and Face Angle limits are too restrictive to successfully mesh the facings. The Minimum setting for these parameters needs to be changed from  $5^\circ$  to  $1^\circ$ , and the Maximum needs to be changed from  $175^\circ$  to  $177^\circ$  in order to generate a complete mesh of solid tetrahedral elements for the geometry.



### 3.1.3.1. Full Model

First, an analysis of the full model is performed. The test specimen is subjected to a 600 lbf load, which is uniformly distributed on the mid-span loading pad as described in previous sections. The analysis is defined as a Multi-Pass Adaptive analysis seeking a convergence level of 3%.

The analysis generates 11,137 solid tetrahedral elements and shows very good convergence behavior. The analysis converges to within 3% on Pass 7 with a maximum polynomial order of 8. Figure 3.10 below contains convergence plots for the analysis, showing the maximum model displacement and maximum von Mises stress computed during each p-loop pass. Both graphs “level off” nicely, indicating that the results are well converged. Total runtime for this analysis is 51.41 hours.

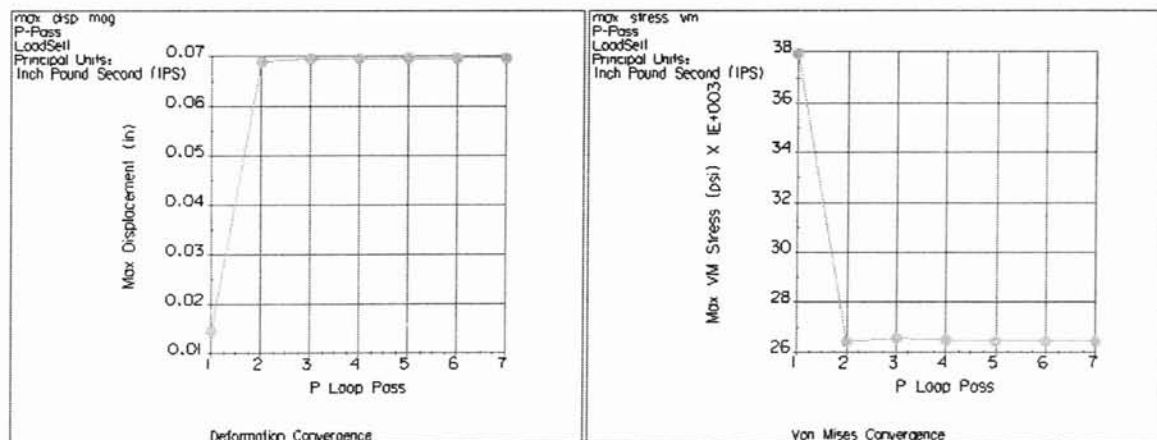


**Figure 3.10: Convergence plots for full model.**

Von Mises stress in the deformed test specimen is shown in Figure 3.11 below. The fringe plot on the left has a scale ranging from 2,500 psi to 22,500 psi to show the stress distribution in the facings; the plot on the right has a scale ranging from 100 psi to 900 psi to show the stress distribution in the solid core. Both plots

reveal stress distributions consistent with our engineering intuition for a beam supported at its ends and loaded in the middle.

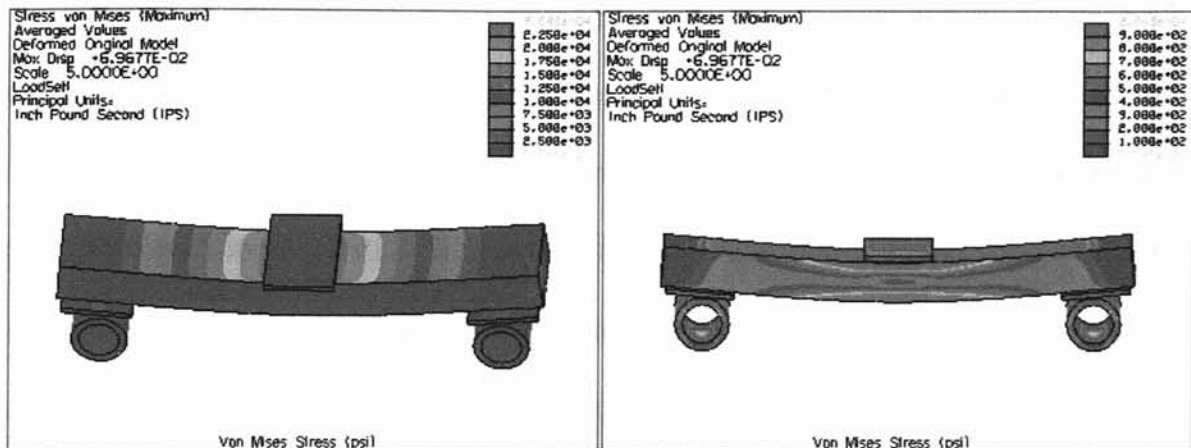


Figure 3.11: Fringe plots of von Mises stress in full model.

### 3.1.3.2. Half Model

Next, the model is cut in half on the y-z plane of symmetry, and the analysis is repeated. For the half model, the applied load is 300 lbf, and we must specify some additional constraints at the plane of symmetry to represent the effects of the missing half of the model. Appropriate constraints involve fixing the x-translation, y-rotation, and z-rotation, and freeing the remaining degrees of freedom – x-rotation, y-translation, and z-translation. (In Mechanics, the rotation constraints are actually irrelevant for this analysis since the model consists entirely of solid elements. However, we will specify the rotational constraints anyway in order to be consistent with our intuition concerning allowable motion at the plane of symmetry.)

This analysis generates 7,578 solid tetrahedral elements and shows very good convergence behavior, much like the full model. The analysis converges to within

3% on Pass 6 with a maximum polynomial order of 7. Total runtime for this analysis is only 12.93 hours, about one-fourth the runtime of the full model.

Von Mises stress in the deformed test specimen is shown in Figure 3.12 below. Again, the fringe plot on the left has a scale ranging from 2,500 psi to 22,500 psi to show the stress distribution in the facings, and the plot on the right has a scale ranging from 100 psi to 900 psi to show the stress distribution in the solid core. As we would expect, the stress distributions are consistent with those for the full model.

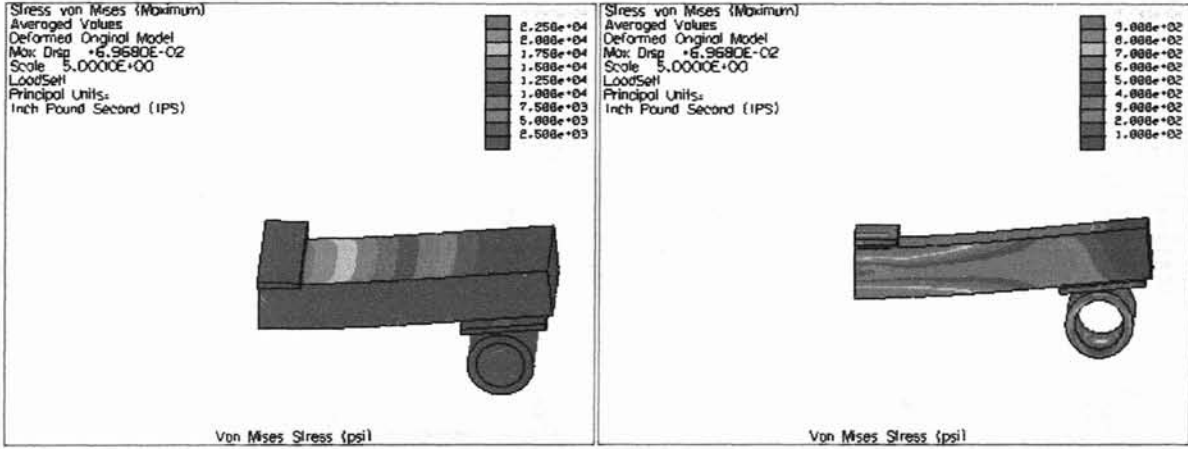


Figure 3.12: Fringe plots of von Mises stress in half model.

### 3.1.3.3. Quarter Model

Finally, the half-model is cut on the x-z plane of symmetry, and the analysis is repeated on a quarter of the full model. For this analysis, the applied load is 150 lbf. Appropriate constraints at the x-z plane of symmetry involve fixing the x-rotation, y-translation, and z-rotation, and freeing the remaining degrees of freedom – x-translation, y-rotation, and z-translation. (As in the half-model, the rotation

constraints are actually irrelevant for this analysis since the model consists entirely of solid elements.)

This analysis generates 5,519 solid tetrahedral elements and once again shows very good convergence behavior. The analysis converges to within 3% on Pass 6 with a maximum polynomial order of 7. Total runtime for this analysis is 5.46 hours.

Von Mises stress in the deformed test specimen is shown in Figure 3.13 below. As we would expect, the stress distributions are consistent with those for the full model and the half-model.

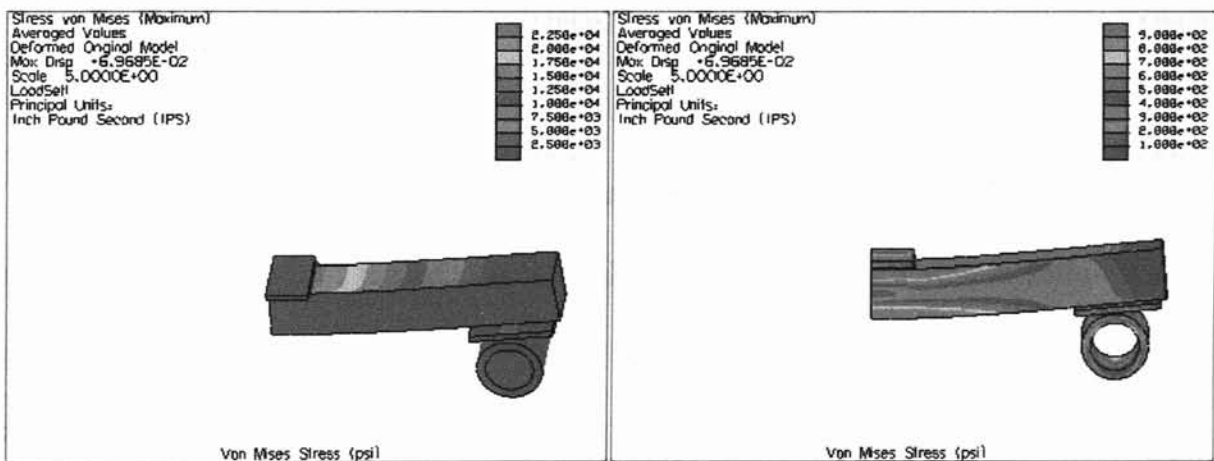


**Figure 3.13: Fringe plots of von Mises stress in 1/4 model.**

The above fringe plots for the full model, half model, and 1/4 model appear to show good qualitative agreement with one another. For a more quantitative comparison, we now consider the maximum model displacement and maximum von Mises stress from each analysis. These values are summarized in the following table, along with other information useful for comparing the different analyses.

**Table 3.2: Comparison of analyses on full model, half model, and 1/4 model.**

	Full model	Half model	1/4 model
Number of Elements (solid tetrahedra)	11,137	7,578	5,519
Max Model Displacement (in)	0.06968	0.06968	0.06968
Max von Mises Stress (psi)	26,433.25	26,434.43	26,435.81
Total Runtime (hours)	51.41	12.93	5.46

Based on these results, we conclude that cutting the model on its symmetry planes is a very useful and effective means of simplifying the analysis. We observe essentially no loss of accuracy, yet the runtime of the quarter model is about one-tenth the runtime of the full model.

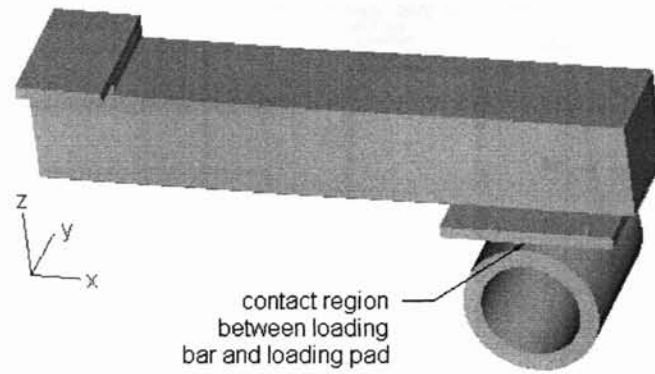
#### 3.1.4. Avoidance of Contact Regions

We have achieved substantial improvements in runtime by limiting our analysis to one-fourth of the full model. However, even with a simple solid-core composite test specimen, total runtime is nearly 5.5 hours. We would like to simplify the model even further before analyzing a more complicated (i.e., honeycomb core) test specimen.

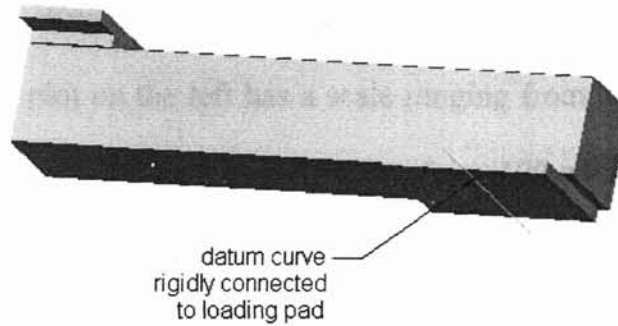
One way we might reduce the computational effort of this analysis is to eliminate contact regions from the model. In our current analysis, Mechanica is spending considerable time computing detailed stress gradients and deformations associated with contact regions. Because contact area varies non-linearly with the applied load, this requires an iterative solution scheme to complete each p-loop pass. This can result in substantially longer runtimes than if no contact region were present.

Our quarter model contains a single contact region, located between the loading bar and loading pad (see Figure 3.14a). Since we are not particularly interested in the contact stresses within these components, we will now modify our model so that it does not require contact analysis.

To eliminate the model's contact region, we delete the loading bar from our model and replace it with a datum curve rigidly connected to the loading pad (see Figure 3.14b). We then constrain the datum curve to simulate the effects of the missing loading bar. Specifically, we constrain the curve against y-translation and z-translation, and against x-rotation and z-rotation. By freeing the remaining two degrees of freedom (x-translation and y-rotation), we permit the curve to translate and rotate in the same way that the loading pad slides and pivots upon the loading bar.



(a)



(b)

**Figure 3.14: Contact region in 1/4 model.**

To evaluate the accuracy of the new boundary conditions, we analyze a  $\frac{1}{4}$ -model composite beam with a 150-lbf applied load, and we compare the results with the  $\frac{1}{4}$ -model analysis presented in the previous section. Our new analysis generates 6,319 solid tetrahedral elements and shows very good convergence behavior, as illustrated by the convergence plots in Figure 3.15. The analysis converges to within 3% on Pass 6 with a maximum polynomial order of 7. Total runtime for this analysis is 1.88 hours.

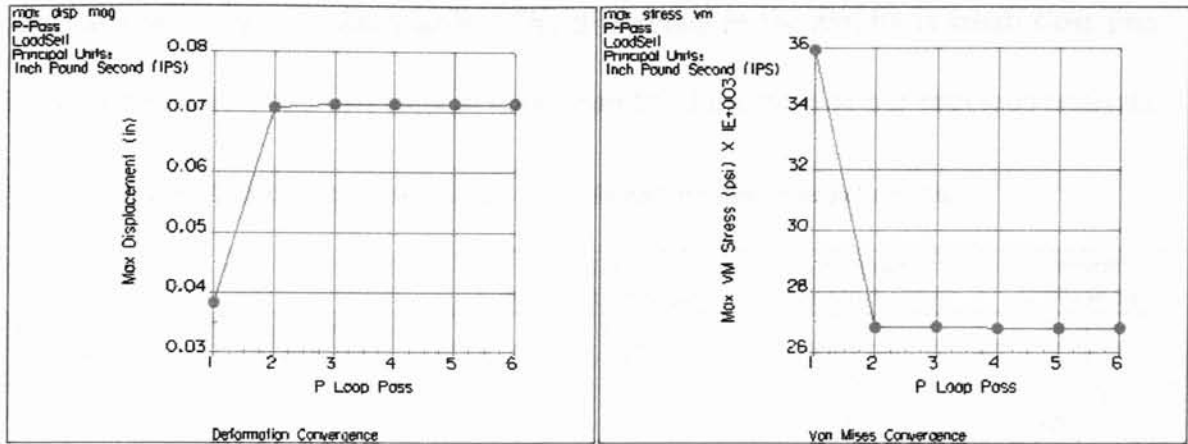


Figure 3.15: Convergence plots for analysis without contact region.

Von Mises stress in the deformed test specimen is shown in Figure 3.16 below. The fringe plot on the left has a scale ranging from 2,500 psi to 22,500 psi, while the plot on the right has a scale ranging from 100 psi to 900 psi. The stress distributions appear very similar to the distributions in the previous section that included the contact region.

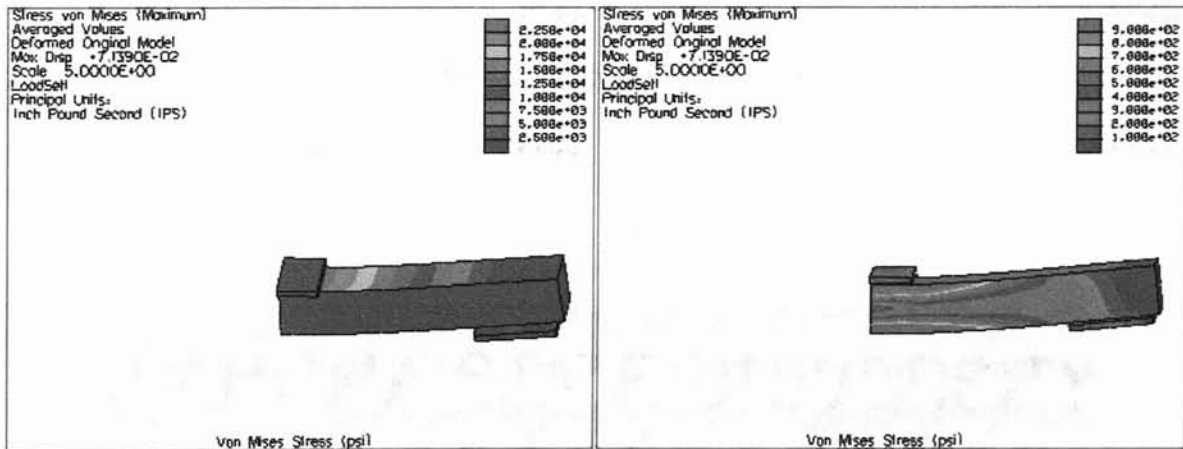


Figure 3.16: Von Mises stress fringe plots for analysis without contact region.

For a more quantitative assessment, we compare values of maximum model displacement and maximum von Mises stress from the two analyses. These are



summarized in the following table. The difference in the results is small (less than 2.5%), yet our new analysis runs in about one-third the time of our previous analysis.

**Table 3.3: Comparison of analyses with and without contact regions.**

	1/4 model with contact region	1/4 model w/o contact region	Percent Difference
Number of Elements (solid tetrahedra)	5,519	6,319	14.5%
Max Model Displacement (in)	0.06968	0.07139	2.45%
Max von Mises Stress (psi)	26,435.81	26,788.77	1.34%
Total Runtime (hours)	5.46	1.875	65.7%

By eliminating the contact region from our analysis, we have thus achieved substantial increase in runtime with minimal loss of accuracy.

### 3.1.5. Honeycomb Model

We are now ready to analyze a test specimen with a honeycomb core. Our initial core will adopt relatively large honeycomb cells to avoid excessive complexity. As illustrated in Figure 3.17 below, the cells have a diameter of 0.65 inches and a wall thickness of 0.025 inches.

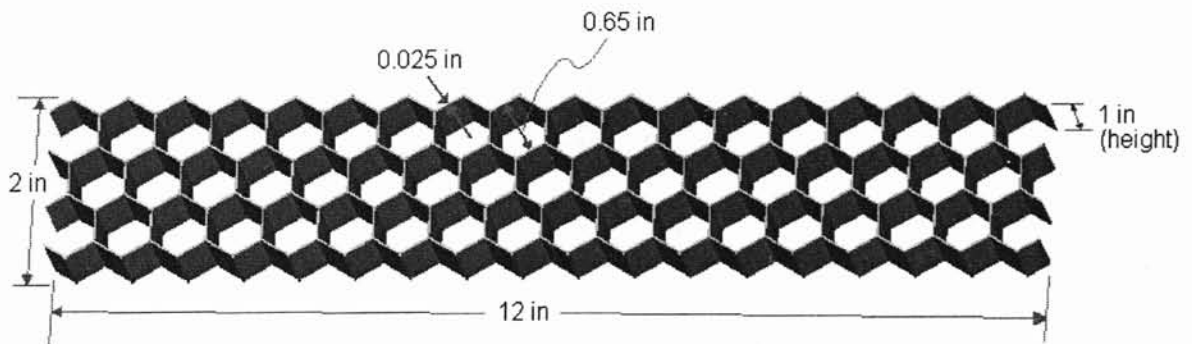


**Figure 3.17: Honeycomb core.**

The honeycomb core is coupled with carbon fiber facings on top and bottom to form a composite beam. As in our previous analyses, each facing consists of two layers of carbon fiber.

We eliminate contact regions from our model as described in the previous section. We also take advantage of the model's two symmetry planes so that we only have to analyze one-fourth of the full model. We then run the analysis with a 150-lbf applied load, utilizing all solid tetrahedral elements to mesh the geometry.

### 3.1.5.1. All Solid Elements

We find that our current AutoGEM settings are too restrictive to mesh the new geometry with solid elements, and we must again modify the limits on the Edge and Face Angles. In order to generate a complete mesh of solid elements, we change the maximum allowed Edge and Face Angles from  $177^\circ$  to  $179^\circ$ .

Mechanica then meshes the geometry with 9,738 solid tetrahedral elements and takes 19.8 hours to complete the run. The analysis ends on Pass 7, when the maximum displacement polynomial order of 9 is reached. Convergence plots of the maximum von Mises stress and maximum displacement are shown in Figure 3.18. Both plots are reasonably well behaved, indicating decent convergence of the solution.

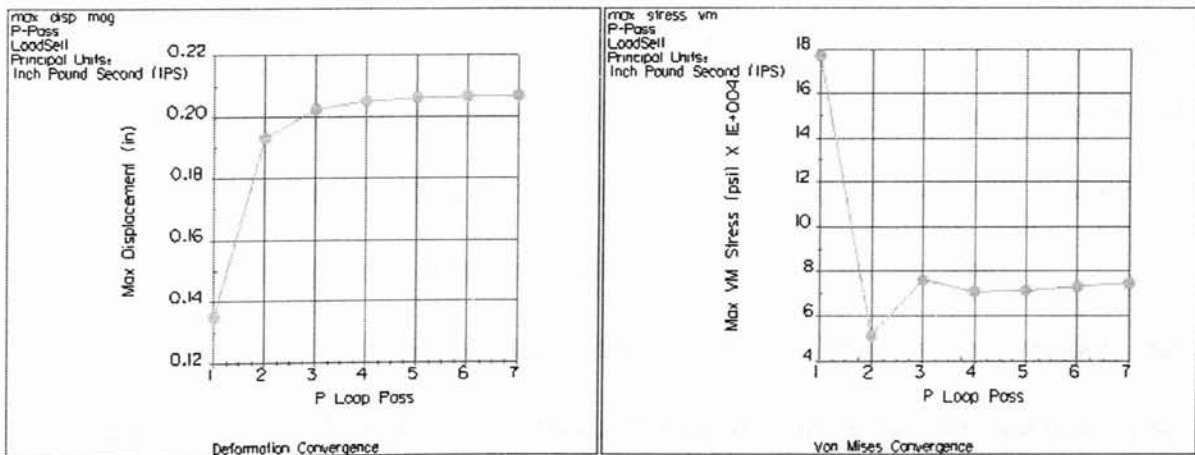
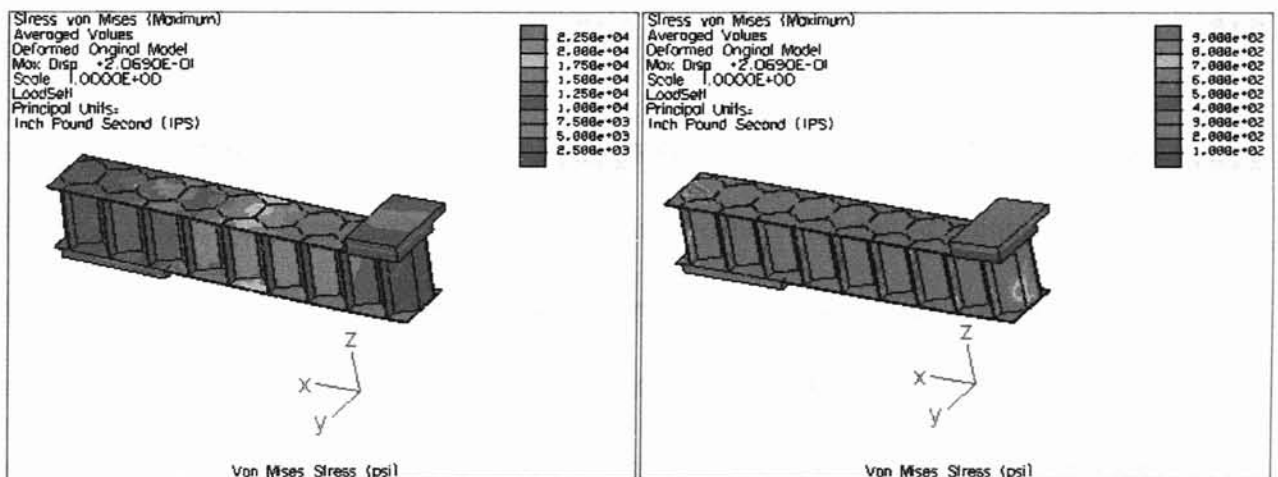


Figure 3.18: Convergence plots for honeycomb-core test specimen.

We now generate fringe plots of the von Mises stress in the model, as shown in Figure 3.19 below. These plots have the same scales as our previous fringe plots (2,500 psi - 22,500 psi on the left, 100 psi - 900 psi on the right), but we have re-oriented the model to view its “back side.” This allows us to see stresses at the center of the test specimen, thanks to our cuts on the symmetry planes. (We could also use Mechanica’s *cutting plane* and *capping surface* tools to further view the interior of our model.)



**Figure 3.19: Von Mises stress fringe plots for honeycomb-core test specimen, all solid elements.**

Our fringe plots allow us to see that cell walls parallel to the y-z plane carry substantially less load than the angled walls. In fact, the y-z walls are in the worst orientation to withstand bending of the beam. In a later section we will explore the effect of re-orienting cells so that their walls are parallel to the x-z plane.

Even though the honeycomb cells are rather large in this model, our computer required 19.8 hours to run this analysis, indicating that the analysis is no simple task. To see how much symmetry had helped us, we repeated the analysis on

a half-model of the same test specimen. After running for 57.90 hours, however, the run crashed due to lack of sufficient hard drive space. Mechanical's computation output files during the analysis filled up the available 54.3 GB of hard drive space and needed more room, so the run crashed.

This experience suggests the need to further simplify the analysis if we want to later analyze larger and more complicated structures. The following section discusses the use of shell idealizations to simplify the model.

#### 3.1.5.2. Facings Compressed to Shells

A reasonable simplification for our model is to compress the carbon fiber facings to their midplanes and mesh these components with two-dimensional shell elements. In general terms, shell elements are an acceptable idealization for thin components whose thickness dimension is less than one-tenth of the component's other dimensions. Our carbon fiber facings, whose thickness is only 0.00904 inches, certainly satisfy this guideline.

After compressing the facings, we specify properties of the associated shell elements using Mechanical's *laminated layup* tool. This tool is convenient for defining engineering laminates by specifying the materials used, the number of layers of each material, and the orientation of each layer. To match our model in the previous section, we specify that each facing consists of two layers of carbon fiber oriented at  $0^\circ$  in the x-y plane.

When we constrain the symmetry planes of our model, we note that it is now important to correctly specify both translation *and* rotation since our shell elements

possess rotational degrees of freedom. After specifying material properties and applying the 150-lbf load, we run the analysis.

When we run the analysis, Mechanica meshes the geometry with 1,677 shells and 7,356 solid elements. The run finishes in 9.2 hours (about one-half the time of our previous analysis) after completing Pass 6 with a maximum polynomial order of 9. Interestingly, we once again see Mechanica pushing the limits of our computer during this analysis. The run had to be completed in two parts because the first attempt crashed after 4.25 hours, reporting that the computer had insufficient swap space for the analysis; after rebooting the computer to clear the memory, the run was re-started from its last completed p-loop pass and finished the analysis approximately five hours later.

We now graph the maximum displacement and maximum stress parameters to evaluate the convergence of the analysis. As shown in Figure 3.20 below, the displacement parameter appears to converge nicely. The maximum von Mises stress, however, does not converge and seems unusually high throughout most of the analysis. (It is possible that the maximum stress might converge if additional p-loop passes could be performed. However, it is likely that the stress would converge to an excessively high value, as explained below.)

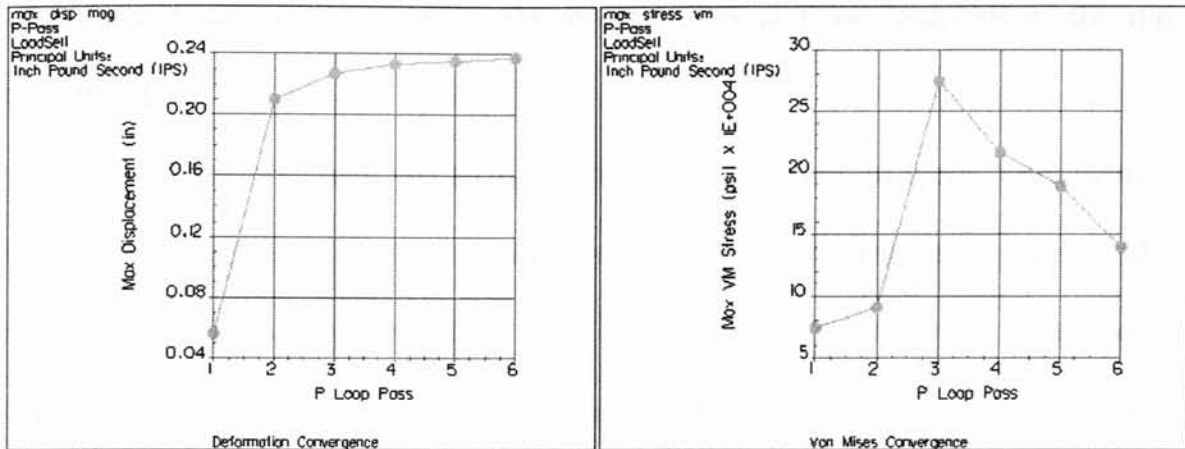


**Figure 3.20: Convergence plots for honeycomb-core test specimen, with facings compressed to shells.**

To understand why the stress value is so high during this analysis, we note that shells have 6 degrees of freedom (3 translation DOF's and 3 rotation DOF's) and solids have only 3 degrees of freedom (3 translation DOF's). In a model that combines shell and solid elements, Mechanica must generate *links* between solid elements and adjacent shell elements in order to fully constrain the shell elements into the model. These links are rigid and can lead to unusually high stress concentrations at solid-shell junctions. These stress concentrations are the likely cause of the excessively high stress values reported during the analysis.

Due to link-related stress concentrations, we should keep in mind that some stress values may be “inflated” at solid-shell junctions. This is one drawback of using shell idealizations to simplify our model rather than meshing the entire model with solid elements.

Although the maximum stress convergence plot does not show nice convergence, this need not be our only indication of stress convergence. Rather, we can place datum points at various locations throughout the model, and we can create

*user-defined measures* to monitor the stress values at those locations as the run progresses.

We therefore repeat the analysis after placing several of these “seed points” throughout the core and facings. Plotting von Mises stress versus p-loop pass at the seed points generates graphs such as those shown below. These graphs reveal much nicer stress convergence and give us greater confidence in the results of the analysis.

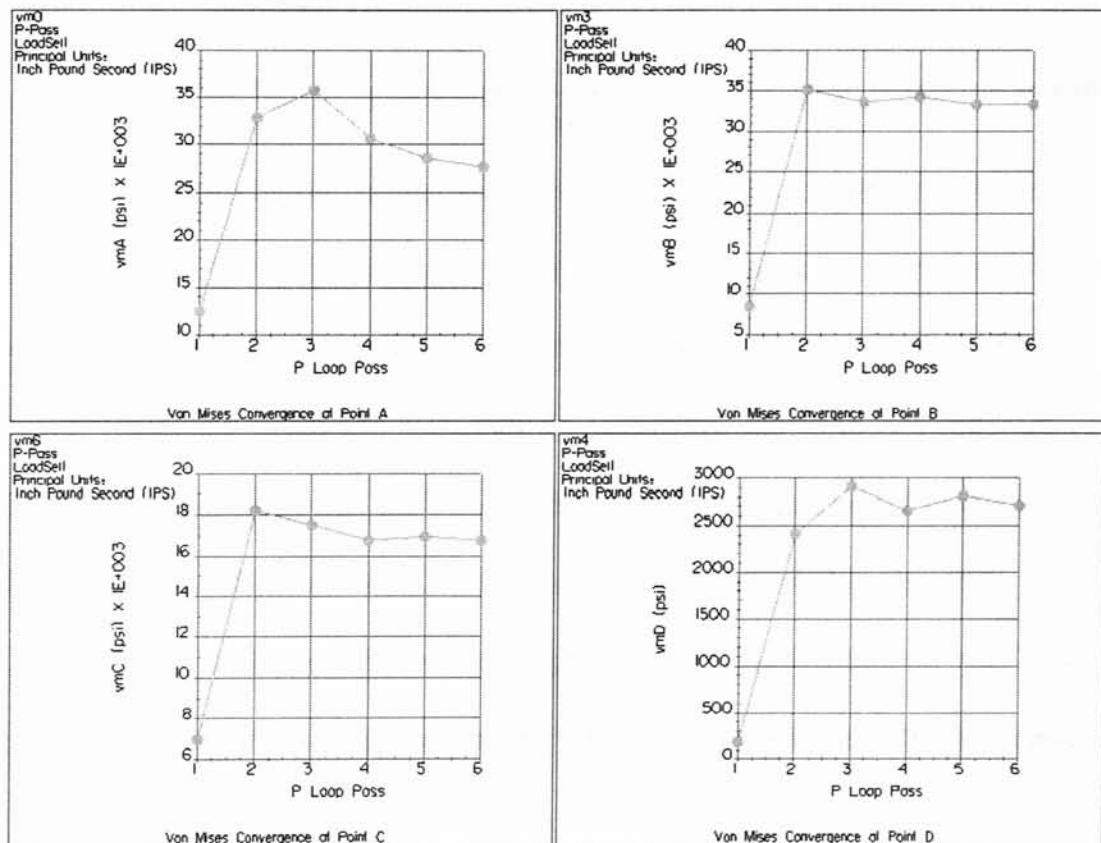


**Figure 3.21: Stress convergence at seed points within test specimen.**

With greater confidence in the convergence of the analysis, we now generate fringe plots of the von Mises stress (see Figure 3.22). These plots show good agreement with the fringe plots of the previous section based on all solid elements.

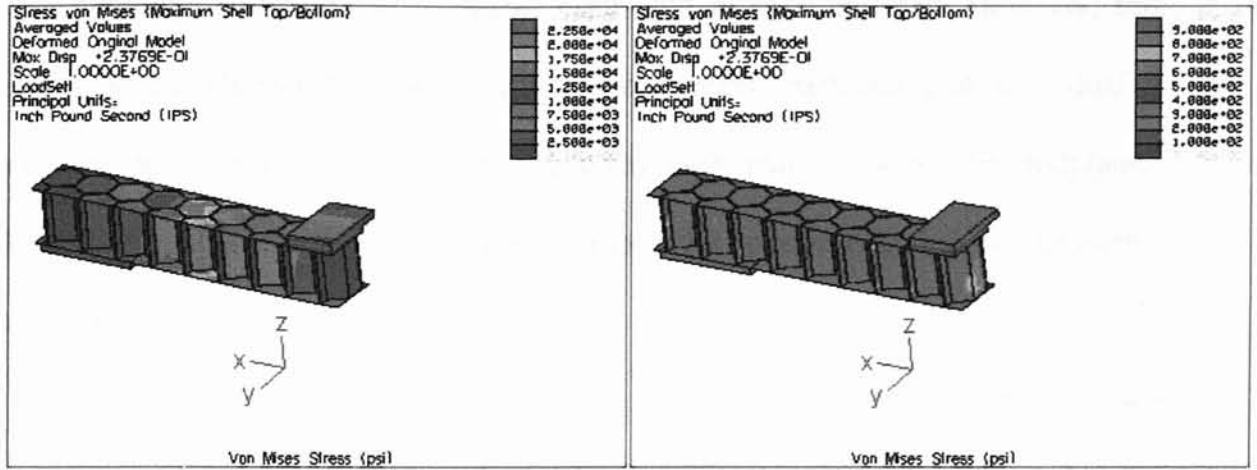


**Figure 3.22: Von Mises stress in honeycomb-core test specimen, with facings compressed to shells.**

For a quantitative comparison between this model and the all-solid model, we can compare the two models in terms of the stress and displacement values computed at various seed point locations. The locations of several seed points and the corresponding stress and displacement values are shown in Appendix D. From this data, we conclude that the displacement values in our current model are within about 3% of the all-solid model, and our stress values are within about 6%.

In the next section, we investigate further idealization of the model by meshing not only the facings but also the honeycomb cell walls with shell elements.

### 3.1.5.3. Core Walls and Facings Are Shells

The honeycomb cell walls, like the carbon fiber facings, comprise thin-walled geometry whose thickness is less than one-tenth of the width and height dimensions. This means that the cell walls are good candidates for shell elements.

We could define the shells much like we defined shells for the facings in the previous section – by specifying the pair of surfaces associated with each wall and



then allowing Mechanica to compress each wall to its midplane. However, this becomes quite inefficient for the user (who must specify each wall pair individually) and for the computer (which must compress each pair to locate the midplane). Instead, we achieve a more efficient shell model by constructing the core geometry as a *surface model* in Pro/E.

When we create the Pro/E surface model of the honeycomb core, we represent each core wall as a two-dimensional surface (thickness = 0) located at the wall's midplane. Upon transferring the geometry into Mechanica, there is no need to pair cell wall surfaces and compress them to midplanes because the wall midplanes are directly available in the surface model. We simply specify the wall thickness that is represented by each midplane, and Mechanica can immediately mesh the geometry with shell elements.

For convenience, we also create surface models of the facings so that we no longer need to compress the facings to their midplanes during the analysis.

We next specify the material properties of all components and apply the 150-lbf load. When we run the analysis, Mechanica generates 563 shell elements and 632 solid elements. The analysis requires less than 7 minutes to complete.

The improvement in runtime is impressive, but we observe unexpected (and unrealistic) displacement behavior when we display the deformed test specimen. As shown in Figure 3.23 below, Mechanica has permitted the rubber pad (composed of solid elements) to penetrate the shell elements of the composite beam test specimen. Close inspection reveals that the bottom loading pad (also composed of solid elements) has penetrated the test specimen as well. As a result of this unrealistic

penetration, deflection values are substantially higher than in our previous analyses, and the model is not producing acceptable results.

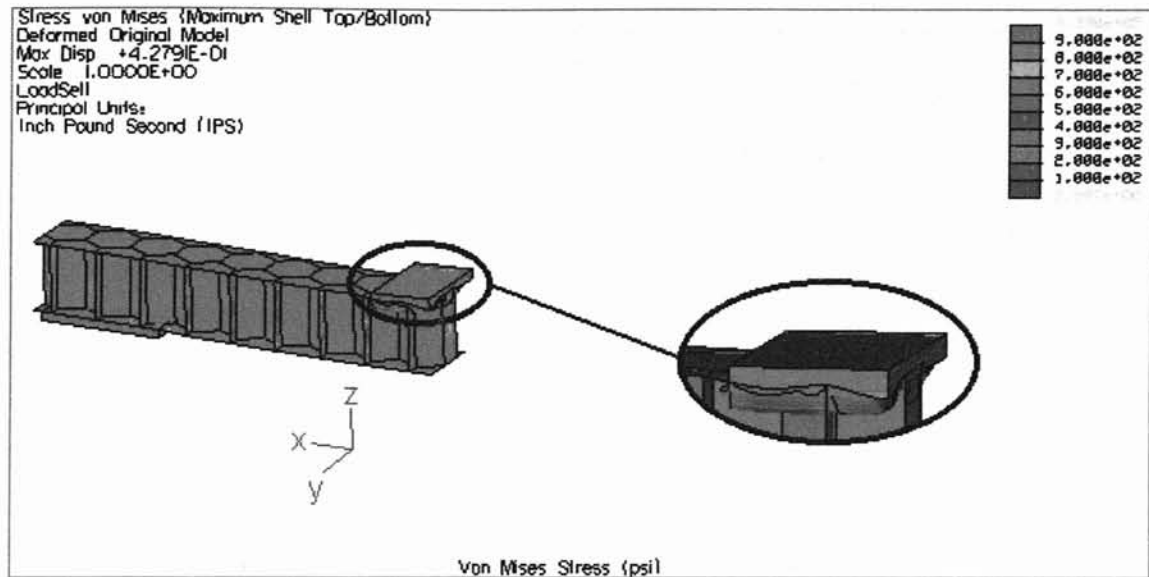


**Figure 3.23: Fringe plot of deformed test specimen, showing penetration of rubber pad into core.**

Preventing this behavior requires two modifications to our model. First, we add a number of datum points to the lower surface of the rubber pad and upper surface of the loading pad in order to “tie” these components to the composite beam (see Figure 3.24). These datum points become element nodes shared by the shell elements of the facings and the tetrahedral elements of the adjoining solid components. As shared nodes, they tie the components together at discrete locations. If we could, we would place an infinite number of points on these surfaces in order to prevent penetration at all locations. Since this is not possible, however, we make a second modification to the model to achieve almost the same effect – we idealize the rubber pad’s lower surface as a rigid surface. This prevents the surface from deforming and penetrating the composite beam in between our discrete datum points. (We could also define the upper surface of the loading pad as

rigid, but this seems unnecessary since it is made of steel and therefore is practically rigid for our loading conditions anyway.)

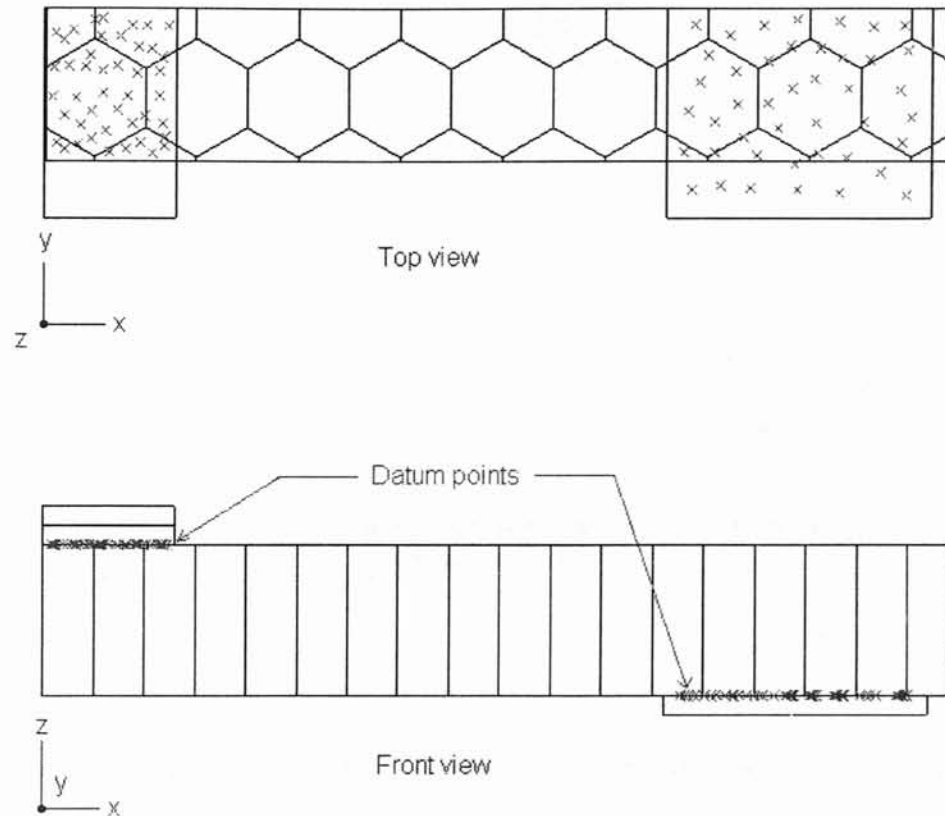


**Figure 3.24: Datum points to “tie” surfaces of rubber pad and loading pad to composite beam.**

With these modifications in place, we repeat the analysis. The added datum points prompt the creation of more elements than before, and Mechanica generates 1,532 shells and 746 solid elements. The run completes on Pass 7 with a polynomial order of 9. Total runtime is 35.7 minutes.

Convergence plots of maximum displacement and maximum stress are shown in Figure 3.25 below. Although the displacement has converged nicely, the von Mises stress shows no indication of convergence. We suspect that the shell-solid links are to blame. We saw in the previous section that linking a shell surface to a parallel solid surface can cause unusually high stress values. We now see that

the singularity is even more pronounced if a shell surface is perpendicular to the solid face it attaches to.

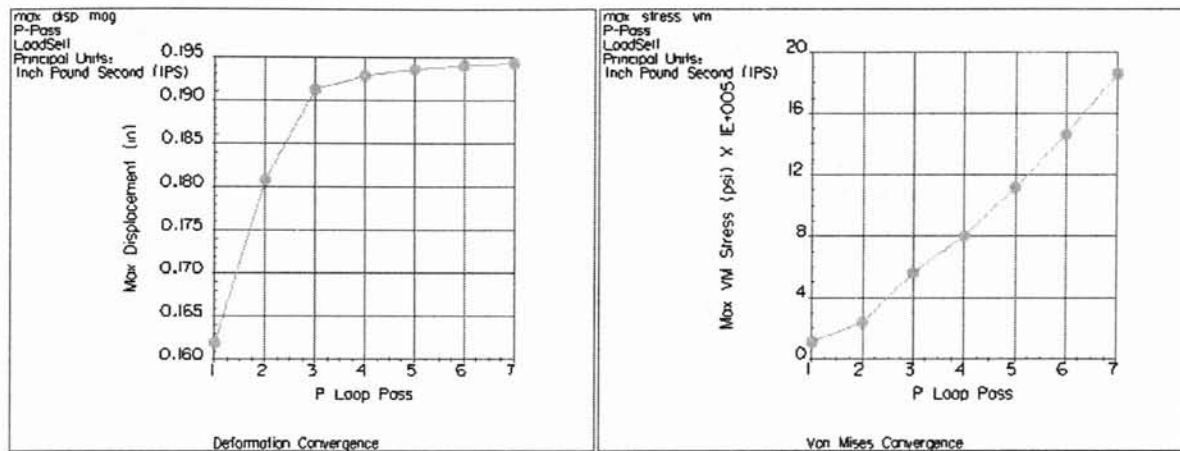


**Figure 3.25: Convergence plots for honeycomb-core test specimen, with core walls and facings modeled as shells.**

Using seed points, we assess the stress convergence at various locations on the core and facings. Plots like those shown below indicate good convergence at discrete locations within the test specimen even though the overall maximum model stress did not converge.

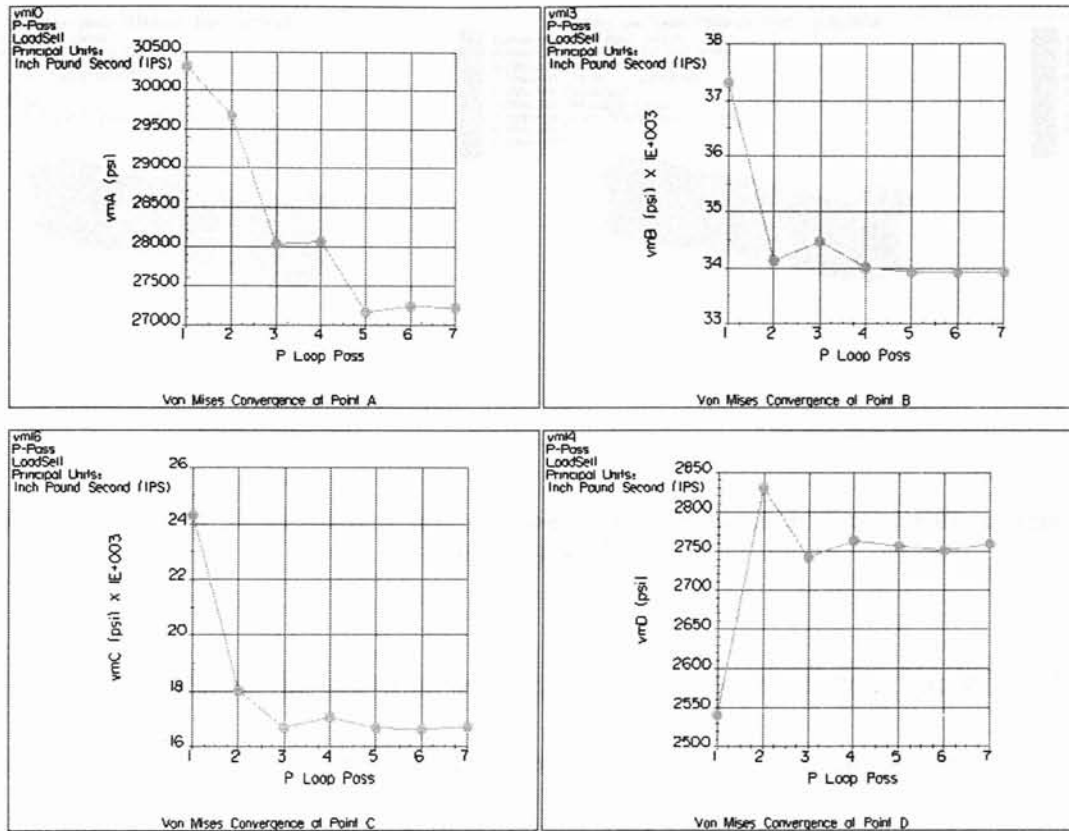


**Figure 3.26: Stress convergence at seed points within test specimen.**

Fringe plots of von Mises stress are shown in Figure 3.27 below. The plot on the left illustrates the expected stress distribution in the facings and appears consistent with our previous honeycomb-core analyses. The plot on the right also shows reasonable agreement with our previous analyses, except directly beneath the rubber pad. In this area, we observe unusually low stress values. This results from defining the bottom of the rubber pad as a rigid surface. Because the surface is not allowed to deform, bending stresses in the beam are substantially reduced immediately beneath this surface. This translates to lower von Mises stress in the core as shown in the fringe plot.

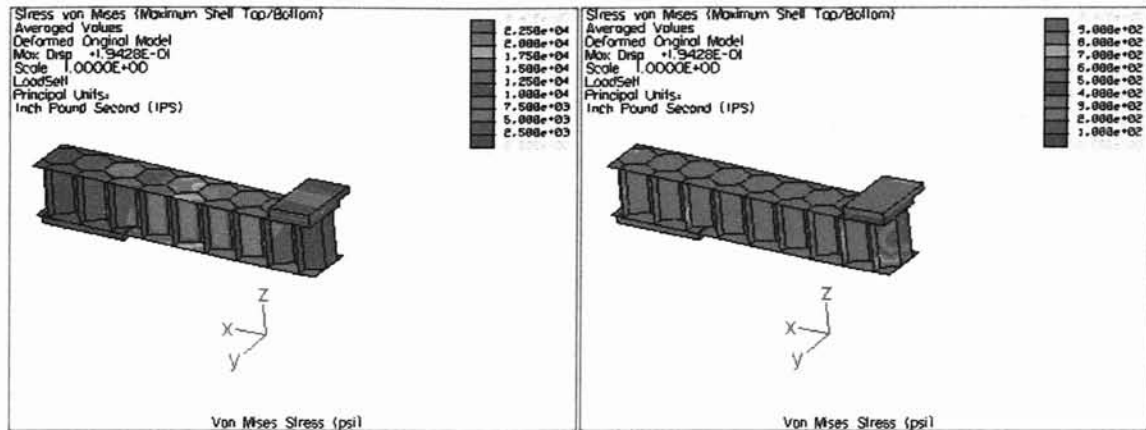


**Figure 3.27: Von Mises stress in honeycomb-core test specimen, with core walls and facings modeled as shells.**

As we did in the previous section, we compare our current model to the all-solid model in terms of stress and displacement values at discrete points. We use the same locations as in the previous section, with the stress and displacement data summarized in Appendix D. We conclude that the displacement values in our current model are within 3% of the all-solid model, and our stress values are within about 16.5%. Thus, we conclude that this model has achieved substantial savings in runtime over previous models, but is somewhat less accurate in predicting stresses in the beam.

Unfortunately, Mechanica does not allow us to use cutting planes or capping surfaces to view the interior of a shell model. Using these tools only reveals stresses in solid components, as shown in Figure 3.28 below. Thus, we have less capability to view the stresses in this model, as compared with our previous solid-core models.

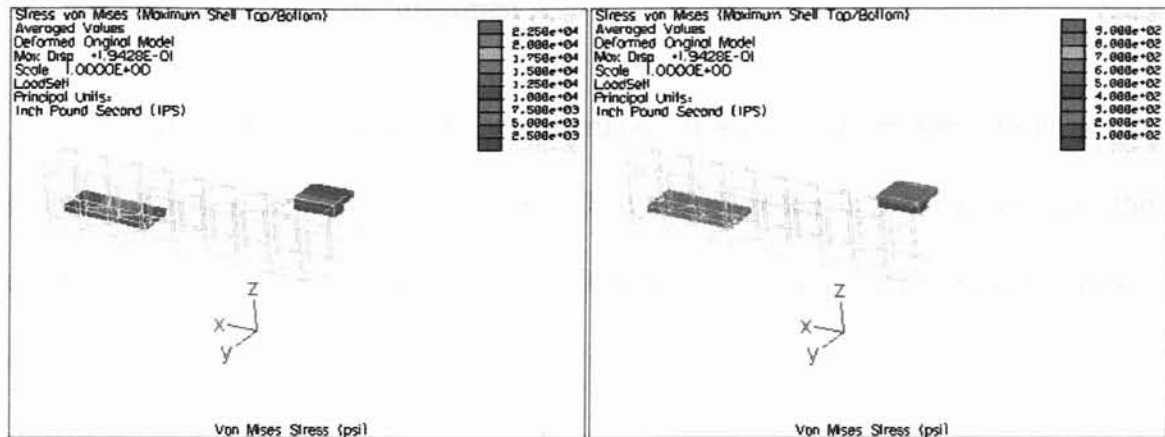


**Figure 3.28: Von Mises stress fringe plots using capping surfaces.**

We have now investigated three different methods for analyzing our honeycomb composite beams:

- 1) Meshing the entire geometry with solid elements.
- 2) Compressing the facings to their midplanes and meshing with shell elements.
- 3) Idealizing the core walls and the facings as shells.

Presumably, the first method is the most accurate since it makes no simplifying assumptions concerning the geometry. The second method loses some accuracy by treating the facings as two-dimensional shells, but it is substantially faster. The third method has more difficulty capturing the true stresses, but it shows good accuracy in predicting displacements and is significantly faster than both previous methods.

Our next task is to analyze two honeycomb test specimens which were recently tested in OSU's mechanical engineering laboratories. For each structure, we will implement each of the above three modeling methods in hopes of gaining further insight into the advantages and disadvantages of each method.

### 3.2. Implementation to Test Specimen A

The first test specimen we wish to analyze is similar to our previous structure but has a much denser honeycomb core. The cell diameter is 0.18 inches, and the wall thickness is 0.025 inches. Figure 3.29 below shows the quarter model that we will analyze.

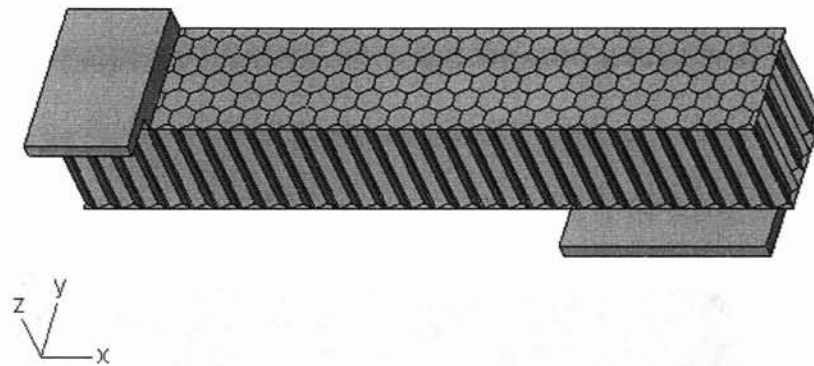


**Figure 3.29: Test Specimen A.**

In this test specimen, the core is made of RPC 700 ND photocurable resin and the facings each consist of two layers of LTM25 / CFS003 carbon fiber fabric.

We first evaluate the effectiveness of idealizing the model using shell elements. To do so, we apply a 150-lbf load and compare the stresses, deflections, and runtimes based on each of our three analysis methods:

- 1) All solid elements.
- 2) Facings compressed to shells.
- 3) Core and facings meshed as shells.

We next compare our computational results to experimental results. We therefore analyze the model under several load magnitudes to generate a load-



deflection curve. We then compare this curve with a load-deflection curve generated experimentally by testing the composite beam in the lab.

### 3.3. Implementation to Test Specimen B

The second test specimen we wish to analyze has a much larger cell size and contains an “outer wall” around the core. The cell diameter of this specimen is 1.0 inches, and the thickness of the cell walls and the core’s outer wall is 0.035 inches. Figure 3.30 below shows the quarter model we will analyze.

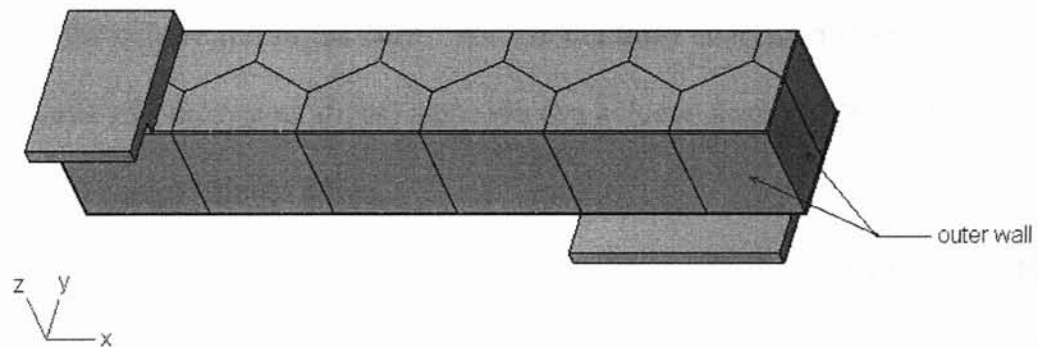


**Figure 3.30: Test Specimen B.**

Test Specimen B contains different materials from the previous test specimen. The core is made of polycarbonate, and the facings each consist of 2 layers of LTM26EL / CFS0508.

As with Test Specimen A, we first assess the advantages of idealizing our model with shell elements. We apply a 100-lbf load to the test specimen and compare the stresses, deflections, and runtimes for each of our three analysis methods.

We next compare our computational results to experimental results. We analyze the model under different load magnitudes and generate a load-deflection curve. We then compare this curve with a load-deflection curve generated experimentally by testing the composite beam in the lab.

### 3.4. Effect of Number of Carbon Fiber Layers

Using our Test Specimen B model, we next study how changes to the structure affect the stiffness of the beam. Specifically, we evaluate changes in the number of layers of carbon fiber in the facings, changes in the wall thickness, and changes in the orientation of the core. We use the third analysis method (idealizing the core walls and facings as shells) since we can achieve accurate deflection results with minimal computational effort.

We first seek to evaluate the benefit of adding additional layers of carbon fiber to the facings. The core walls in these analyses have a nominal wall thickness of 0.035 inches. We run a series of analyses, incrementing the number of layers in each facing from zero to six. For each analysis, we record the deflection at the bottom of the lower facing when the beam is subjected to a total load of 400 lbf.

### 3.5. Effect of Wall Thickness

Next, we seek to evaluate the benefit of increasing the thickness of the honeycomb walls (both the outer core wall and the cell walls). We run a series of analyses changing the wall thickness from 0.010 inches to 0.100 inches in small increments. For each analysis, the facings consist of 2 layers of carbon fiber. Once

again, we record the deflection at the bottom of the lower facing when the beam is subjected to a load of 400 lbf.

### 3.6. Effect of Core Orientation

Finally, we wish to evaluate the effect of rotating the core cells  $90^\circ$  (about the z-axis) from their current orientation. The new orientation is illustrated in Figure 3.31 below. The wall thickness is 0.035 inches and the facings consist of two layers of carbon fiber.

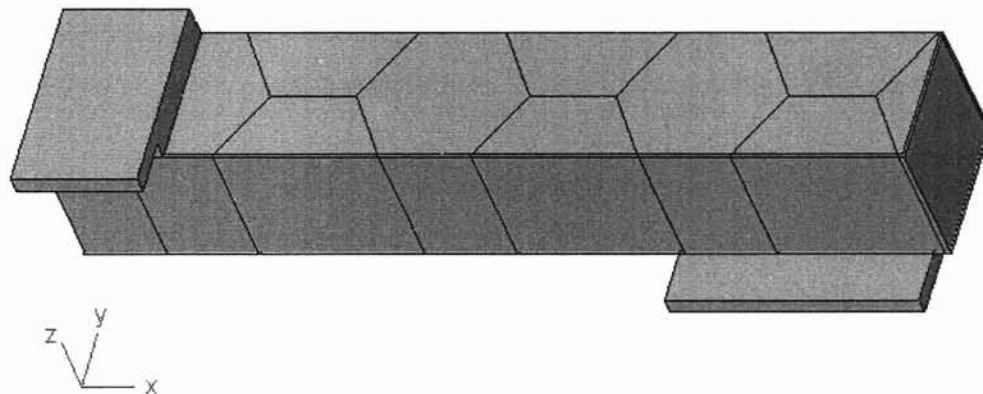


**Figure 3.31: Alternate core orientation based on Test Specimen B.**

To gain additional insight, we also rotate the cell orientation of Test Specimen A by  $90^\circ$  (see Figure 3.32 below). Recall that Specimen A has a cell diameter of 0.18 inches. After we run the analysis, we compare deflections with the original core orientation.

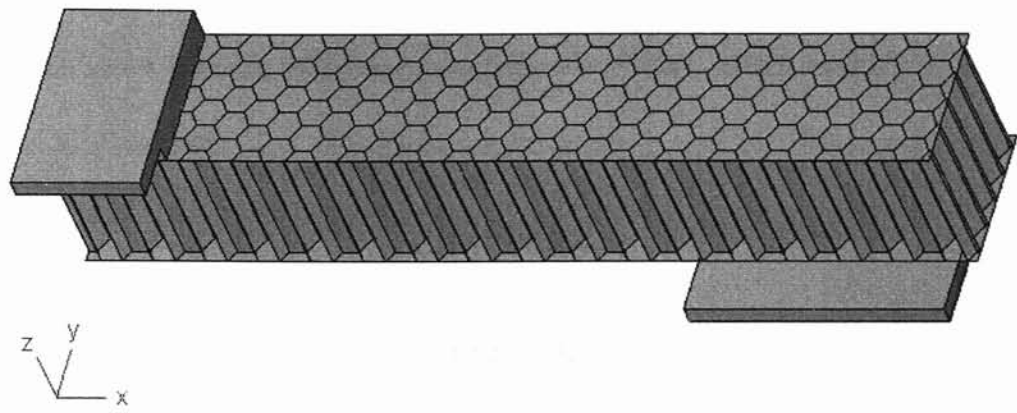


**Figure 3.32: Alternate core orientation based on Test Specimen A.**

## CHAPTER 4

### RESULTS

#### 4.1. Results for Test Specimen A

This section presents the analysis results for Test Specimen A and compares them to experimental findings. As described previously, Test Specimen A has a dense honeycomb core, with cell diameter 0.18 inches and wall thickness 0.025 inches. Figure 4.1 shows the model under investigation.

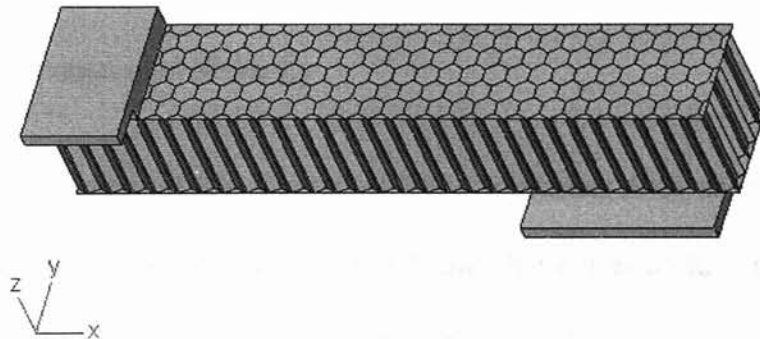


**Figure 4.1: Test Specimen A.**

##### 4.1.1. All Solid Elements

When modeling the geometry entirely with solid tetrahedral elements, the analysis proves too computationally intensive for our Pentium IV 1.8 GHz computer.

Mechanica meshed the geometry and completed Pass 1 and Pass 2 of the analysis in about 2 hours, but the run appeared to “stall” while solving equations in Pass 3. No progress was shown for several days, and we observed Mechanica making no use of available System Resources. The analysis had simply halted without explanation.

We rebooted the computer and set the analysis to “restart” from the previously completed Pass 2. The analysis proceeded normally into Pass 3 but again froze while solving the finite element equations.

We rebooted the computer once again and restarted the analysis. Mechanica proceeded as before, getting stuck while solving the Pass 3 equations. Mechanica was left running for over a week but showed no indication of progress.

Based on this experience, we concluded that we simply do not have the resources to run an analysis of this magnitude.

#### 4.1.2. Facings Compressed to Shells

When we compress the facings of Test Specimen A to shells, we find that Mechanica is unable to generate a complete finite element mesh for the model.

We note that although shells are simpler than solid elements when generating and solving finite element equations, combining shell geometry and solid geometry in one model makes the model substantially more difficult to preprocess and mesh. Not only must the geometry be discretized so that shell nodes coincide with solid nodes at all solid-shell junctions, but all junctions must acquire *links* to fully constrain the shells (having 6 DOF's) to solids (having only 3 DOF's).

We tried many different combinations of AutoGEM parameter settings, but none of them enabled the software to successfully mesh the geometry. Even as we approached Mechanica's built-in limits for the most relaxed allowable AutoGEM settings, Mechanica failed to generate a complete mesh.

After making over twenty different attempts to mesh the geometry, we concluded that this particular model is just too complex for Mechanica's preprocessing engine.

#### 4.1.3. Core Walls and Facings Are Shells

When we model the facings and core walls of Test Specimen A as shells, the analysis runs to completion. Mechanica generates 2,886 shells and 680 solid elements; the run finishes after completing Pass 7, with a maximum polynomial order of 9. Total runtime for this analysis is 1.65 hours.

Convergence plots of the maximum displacement and maximum stress are shown in Figure 4.2 below. Both plots show the anticipated behavior for this solid-shell model; the displacement graph levels off, showing reasonable convergence, and the stress continues to rise with no sign of convergence. As described previously, the stress convergence problem is due to shell-solid links causing abnormally high stress.

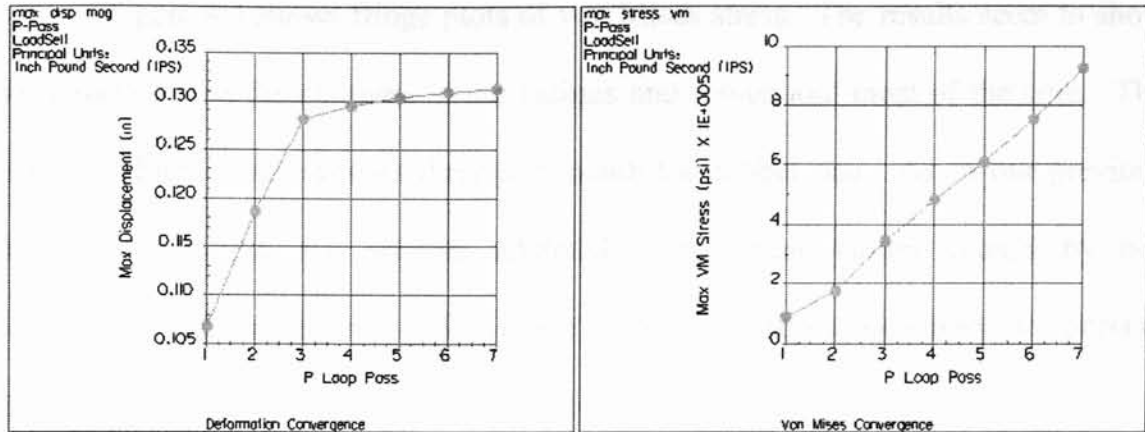


Figure 4.2: Convergence plots for Test Specimen A, with core walls and facings modeled as shells.

Nonetheless, seed points located in the core and facings (see Appendix E) show reasonable stress convergence as shown in Figure 4.3 below. We therefore conclude that our stress results are not entirely inaccurate.

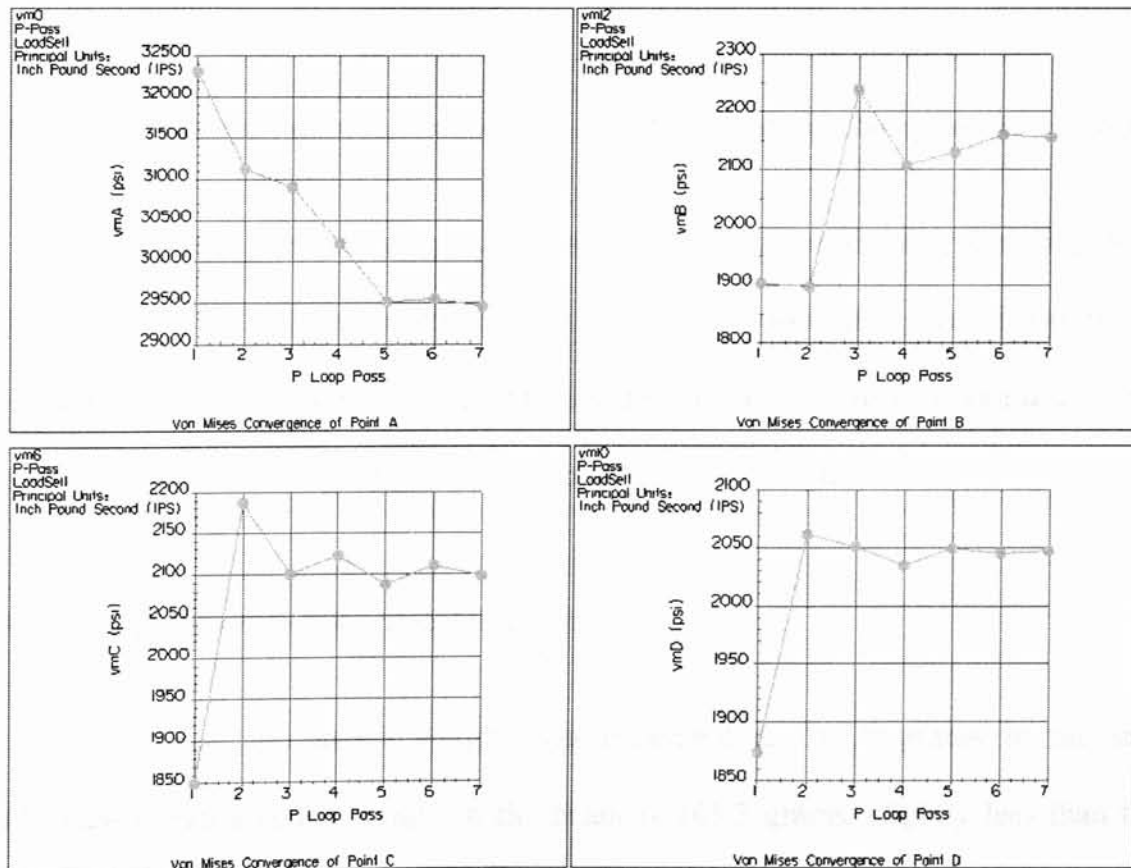
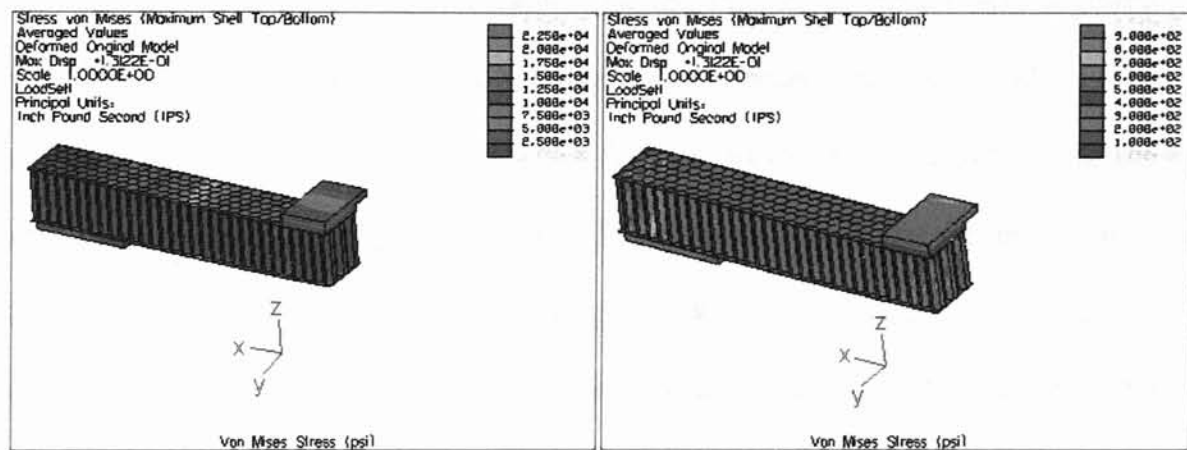


Figure 4.3: Stress convergence at seed points within Test Specimen A.



Figure 4.4 shows fringe plots of von Mises stress. The results seem to show reasonable stress distributions in the facings and throughout most of the core. The only “problem area” appears directly beneath the rubber pad. As in our previous honeycomb model, we observe artificially low stress values caused by our idealization of the rubber pad’s lower surface as rigid, necessary to prevent penetration into the core.



**Figure 4.4: Von Mises stress in Test Specimen A, with core walls and facings modeled as shells.**

We notice in the fringe plots that some of the core walls carry very little load (evidenced by their low stress values) because they are orientated parallel with the y-z plane. In a later section we will evaluate the increase in stiffness obtained by re-orienting the core to align these walls parallel with the x-z plane.

#### 4.1.4. Comparison to Experimental Results

The test specimen’s weight was measured as 147.9 grams in the lab. Mechanics indicates the weight of the beam is 145.3 grams, slightly less than the actual weight. The small difference is perhaps due to the film adhesive used in

constructing the test specimen. Since the film adhesive was not expected to influence the stress or deflection of the test specimen, it was not included in the Pro/MECHANICA model.

We now analyze the test specimen at several different load values and generate a load-deflection curve for the model. We can then compare our results with load-deflection curves obtained experimentally in the lab.

The experimental load-deflection data, obtained by Patterson, was acquired by testing the composite beam on an Instron load frame [Patterson, 2001]. The recorded deflections are values displayed by the Instron machine indicating the vertical displacement of the Instron head. This corresponds to the displacement of the mid-span steel loading pad in our model. When we plot the computational results along with two experimental curves obtained in the lab, we have the following graph.

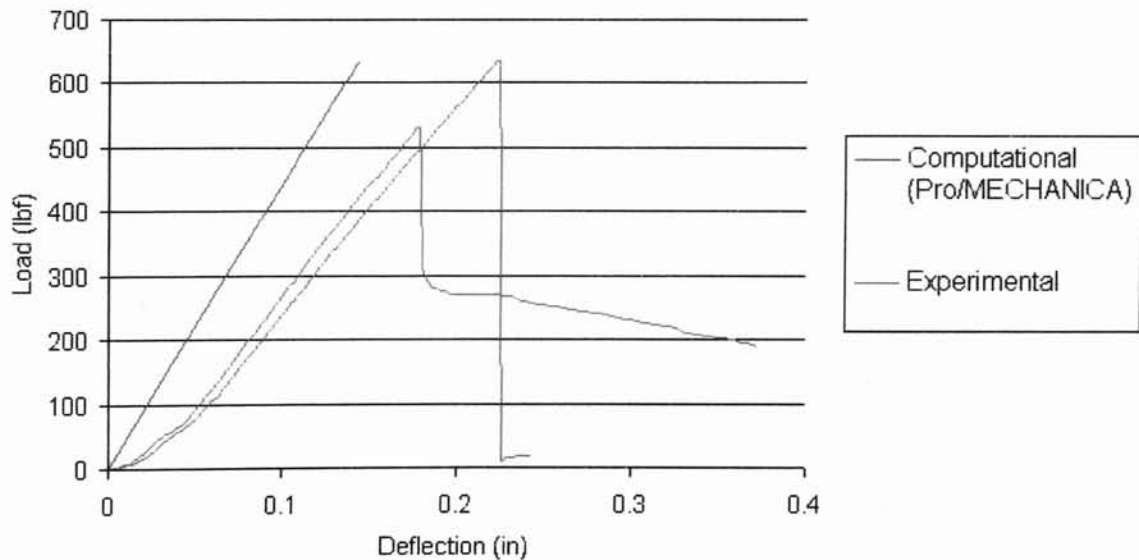


**Figure 4.5: Load versus deflection curves based on computational and experimental results.**

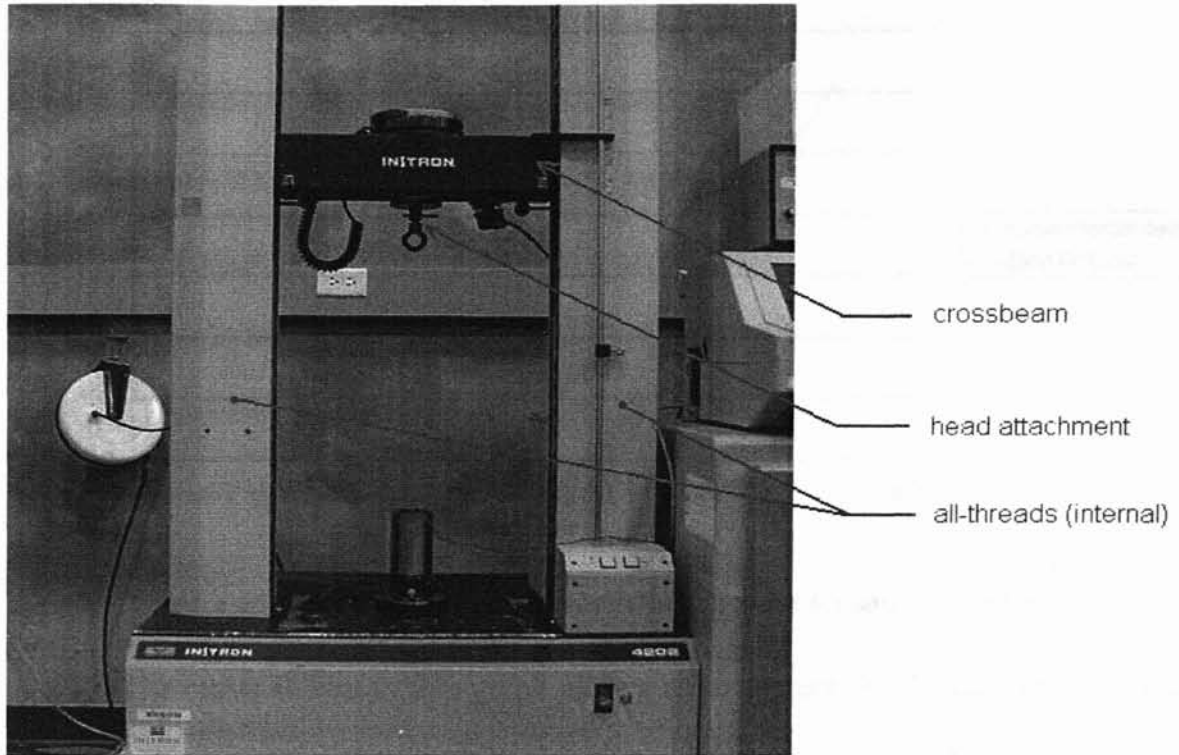


**Figure 4.6: Instron load frame.**

To assess the magnitude of error that can be attributed to the Instron's finite stiffness, we generate a load-deflection curve from a small steel plate resting directly upon the Instron's load platform. A simple FEM analysis of the steel plate reveals that the vertical deflection should be essentially zero (Mechanica reports the value to be 0.0000124 inches under a 600-lbf load). Experimental data suggests a much larger deflection, however, as shown in Figure 4.7.

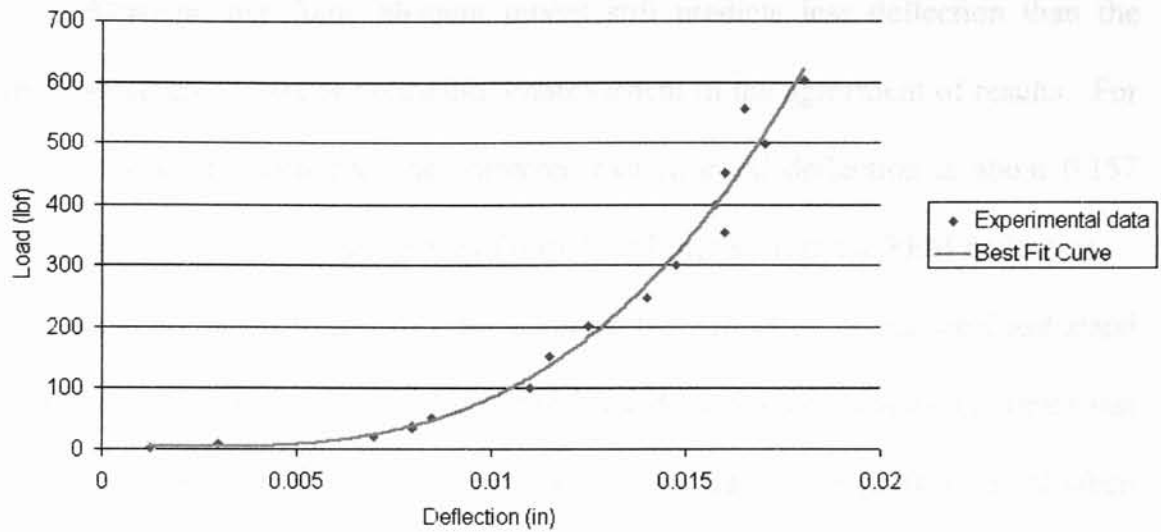


**Figure 4.7: Experimental load versus deflection curve for small steel plate.**

The curve shown in this graph allows us to correct for the deflection of the Instron machine during our experiments. By subtracting this deflection from the corresponding experimental deflection value at a given load, we obtain the following “corrected” load-deflection curves.

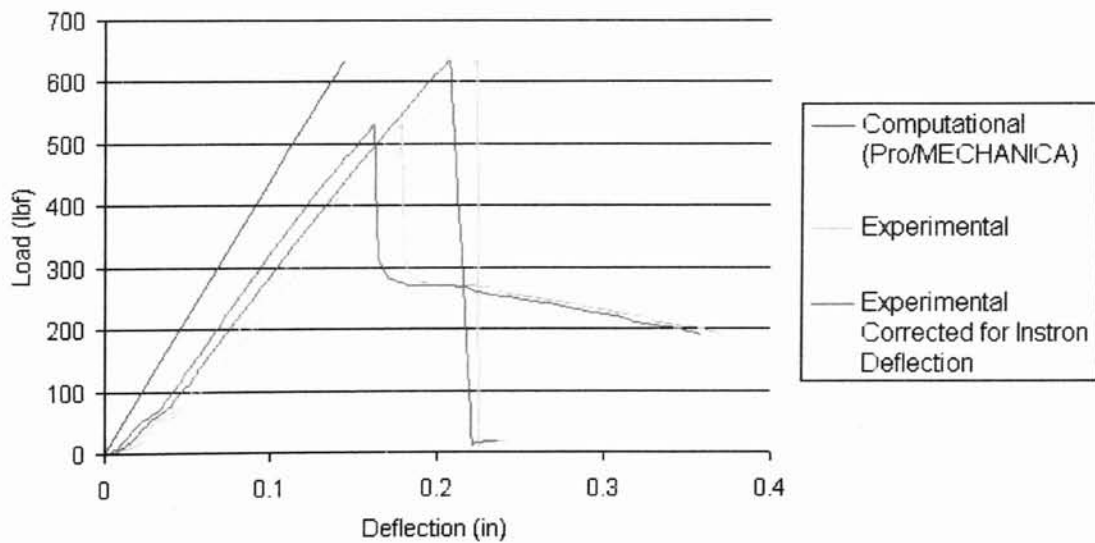


**Figure 4.8: Test Specimen A load versus deflection curves based on computational and experimental results, corrected for Instron deflection.**

Although our finite element model still predicts less deflection than the experimental data, there is noticeable improvement in the agreement of results. For a 500-lbf load, for example, the corrected experimental deflection is about 0.157 inches. This represents a difference of only 0.044 inches from the FEM deflection.

Another likely source of error involves the deflection of our steel test stand during the experiments. Recall that the test stand supports the composite beam test specimens (see Figure 4.9), and we assumed the test stand to be perfectly rigid when we established boundary conditions for our FEM model. During our experiments, it is likely that the test stand does in fact deform under the applied load, which will increase the apparent deflection of the test specimen. Unfortunately, the magnitude of the test stand's deflection is difficult to quantify, but it is reasonable to conclude that this deflection accounts for some of the difference between our experimental results and FEM results.

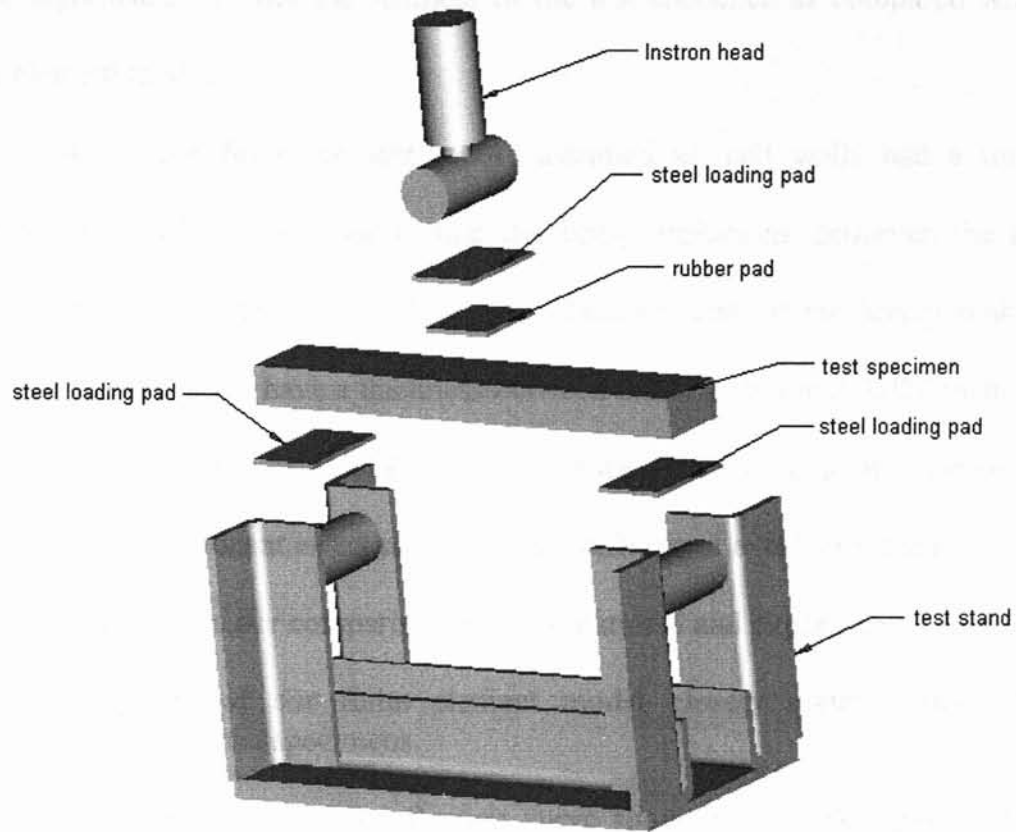


**Figure 4.9: Exploded view of experimental setup.**

Additional sources of error relate to the material properties and geometry of the test specimen itself. Our finite element model assumed that the resin core was perfectly homogeneous with no voids in the honeycomb walls. Due to real-world manufacturing limitations, however, it is quite possible that the core contained internal flaws or contaminants that would weaken the structure, causing greater deflection than predicted by FEM. Furthermore, the modulus used in our finite element model assumed that the entire core was fully post-cured. Experience with RPC resin suggests that material properties are substantially degraded if full post-cure is not achieved. Experience also suggests the possibility that the core may not have been fully post-cured by the manufacturer before shipment to OSU. This

would significantly reduce the stiffness of the test specimen as compared with the finite element model.

Finally, our finite element model assumed all cell walls had a uniform thickness of 0.025 inches. Due to manufacturing limitations, however, the actual wall thickness varies throughout the core. Measurements of the honeycomb core indicate that most walls have a thickness between 0.020 inches and 0.030 inches, but a number of walls fall outside of this range. As we will show in a later section, wall thickness has a significant effect on the overall stiffness of a test specimen.

To summarize our comparison of computational and experimental results:

- 1) The weight of our finite element model closely matches that of the experimental test specimens.
- 2) The computational load-deflection curve shows reasonable agreement with experimental curves.

The computational load-deflection curve predicts slightly less deflection than observed in the experimental results, but this is not surprising when we consider the numerous assumptions that must be incorporated into our finite element model concerning boundary conditions, material properties, and specimen geometry.

#### 4.2. Results for Test Specimen B

This section presents the analysis results for Test Specimen B and compares them to experimental findings. As described previously, Test Specimen B has a large-cell honeycomb core (diameter = 1 inch) and has a wall surrounding the outside of the core. Figure 4.10 shows the model under investigation.

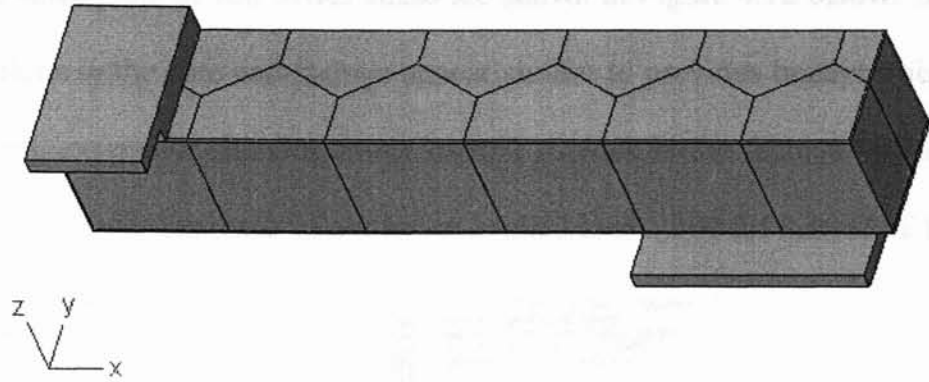


**Figure 4.10: Test Specimen B.**

#### 4.2.1. All Solid Elements

When we run the analysis with all solid tetrahedra, Mechanica meshes the geometry with 8,846 elements. The run lasts 16.6 hours and completes on Pass 7 with a maximum polynomial order of 9.

Convergence plots of the maximum von Mises stress and maximum displacement are shown in Figure 4.11. Both plots are reasonably well behaved, indicating decent convergence of the solution.

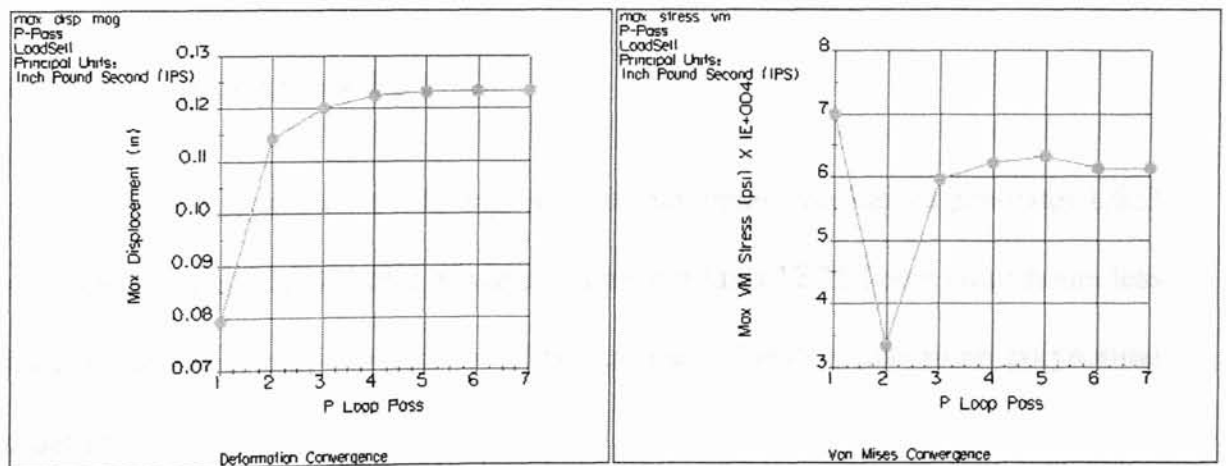


**Figure 4.11: Convergence plots for Test Specimen B, all solid elements.**



Fringe plots of von Mises stress are shown in Figure 4.12 below. The stress distributions in the core and facings appear similar to previous honeycomb core test specimens, except for showing lower overall stresses in the facings. (These lower stresses are simply the result of our lower applied load – 100 lbf instead of 150 lbf.)

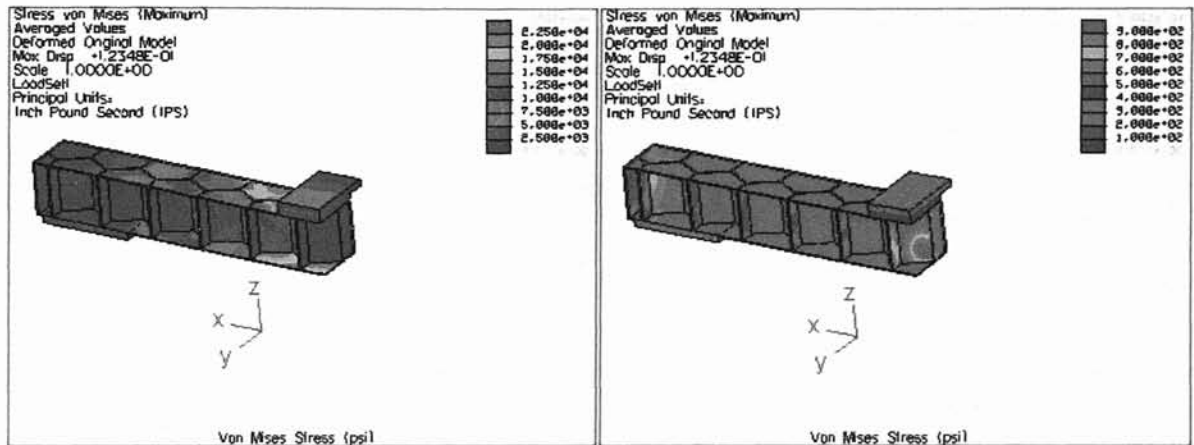


**Figure 4.12: Von Mises stress in Test Specimen B, all solid elements.**

We again notice that some of the core walls carry very little load (they have low stresses) due to their orientation. They therefore provide little contribution to the beam’s stiffness. In a later section we will reorient the core by 90° and evaluate the beam’s new stiffness.

#### 4.2.2. Facings Compressed to Shells

After we compress the facings to their midplanes, Mechanica generates 1,623 shell elements and 5,247 solid elements. This run lasts 12.35 hours (four hours less than the all-solid analysis) and completes on Pass 7 with a maximum polynomial order of 9.

Convergence plots of maximum displacement and maximum stress are shown in Figure 4.13 below. The displacement parameter appears to converge well.

The maximum von Mises stress, however, does not give a clear indication of convergence and is an order of magnitude higher than in the all-solid analysis. The poor convergence and unusually high stress is again related to the solid-shell links required in this model.

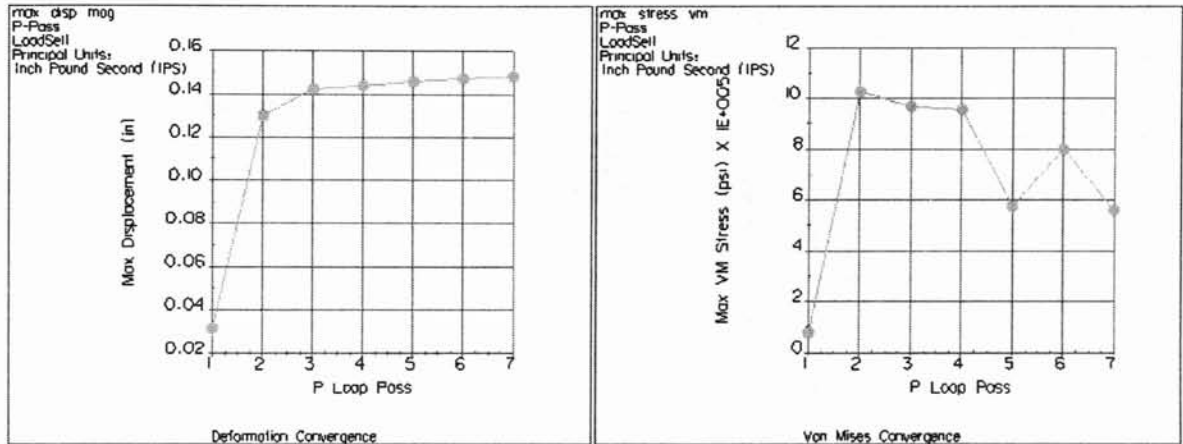


**Figure 4.13: Convergence plots for Test Specimen B, with facings compressed to shells.**

Because the maximum model stress does not show nice convergence, we seek an alternative indication of stress convergence for our model. We again place datum points at various locations in the model (shown in Appendix F) and monitor the stress convergence at these locations. Plotting von Mises stress versus p-loop pass at the seed points generates graphs such as those shown below. The graphs suggest that the stress is in fact converging, and they give us greater confidence in the results of the analysis.

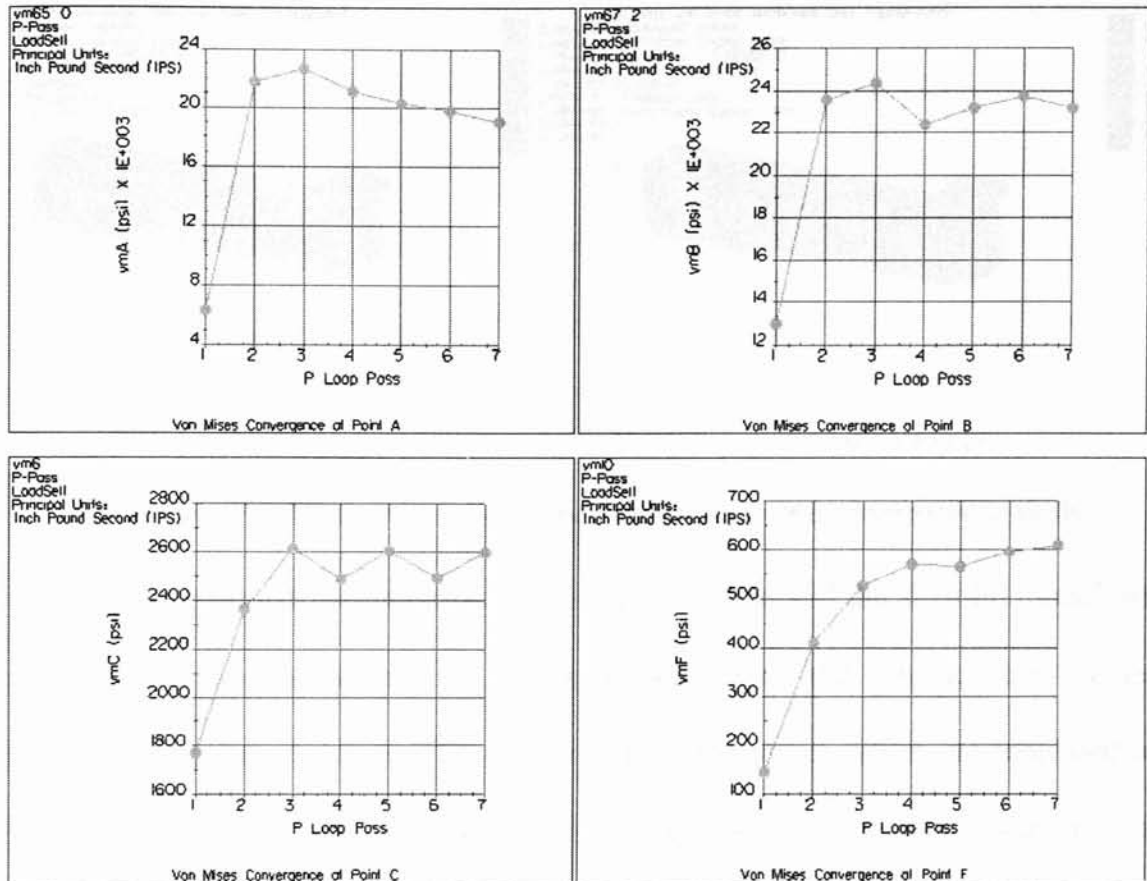


**Figure 4.14: Stress convergence at seed points within Test Specimen B, with facings compressed to shells.**

We see from the fringe plots in Figure 4.15 below that the stress distribution basically matches the distribution predicted by the all-solid model. The only apparent discrepancy is in the lower facing near the beam’s center, where our current model predicts somewhat higher stresses. These high stresses can be attributed to solid-shell links between the core and facing.

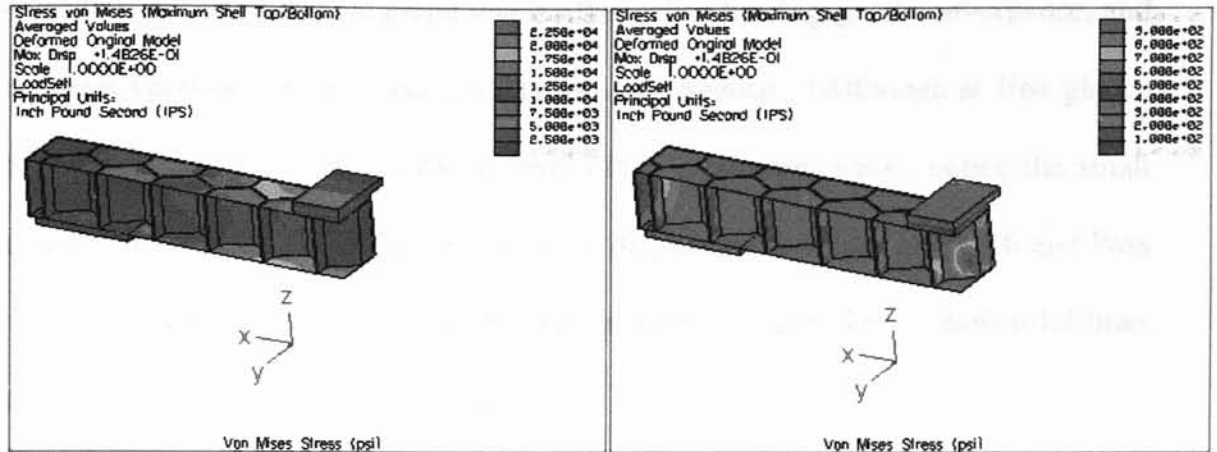


**Figure 4.15: Von Mises stress in Test Specimen B, with facings compressed to shells.**

For a quantitative comparison between this model and the all-solid model, we can compare the two models in terms of the stress and displacement values computed at our seed points. The stress and displacement values are tabulated in Appendix F. From this data, we conclude that the displacement values in our current model are within about 3% of the all-solid model, and our stress values average within about 6%.

Thus, by compressing the facings to shells we achieved significant savings in time with little loss of accuracy.

#### 4.2.3. Core Walls and Facings Are Shells

When we model the facings and core walls as shells, the analysis runs even faster. Mechanica generates 1,470 shells and 461 solid elements; the run finishes after completing Pass 7, with a maximum polynomial order of 9. Total runtime for this analysis is about 24 minutes.

Convergence plots of the maximum displacement and maximum stress are shown in Figure 4.16 below. Both plots show the anticipated behavior for this type

of model; the displacement graph levels off nicely, showing good convergence, and the stress continues to rise, with no sign of convergence. (Although at first glance the displacement does not appear to level off to a constant value, notice the small scale on the y-axis. The difference between displacement values at Pass 6 and Pass 7 is less than 1%.) The stress convergence problem is again due to shell-solid links causing extremely high localized stresses.

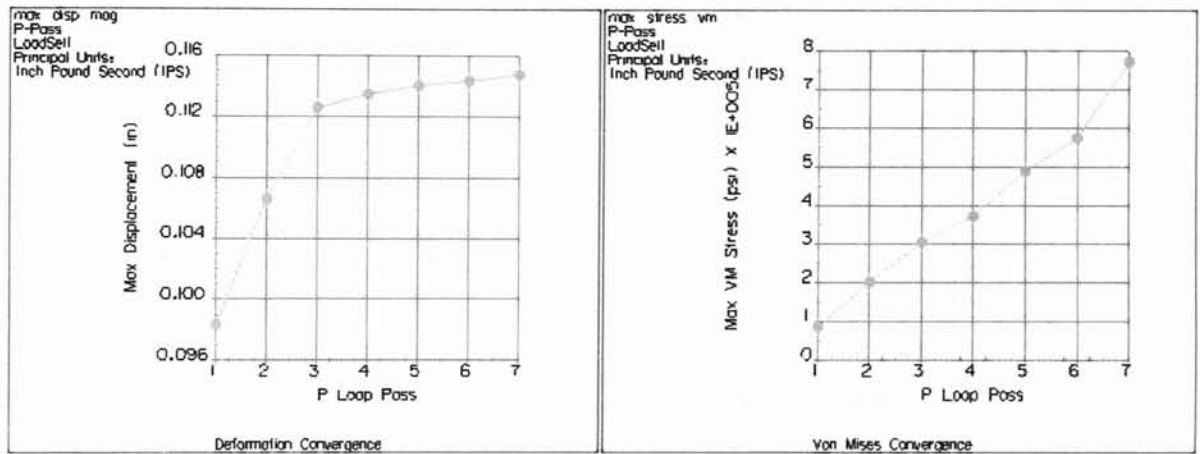


**Figure 4.16: Convergence plots for Test Specimen B, with core walls and facings modeled as shells.**

Seed points located in the core and facings show reasonable stress convergence, however. (See Figure 4.17 below.) We therefore conclude that our stress results at most locations throughout the test specimen are valid.

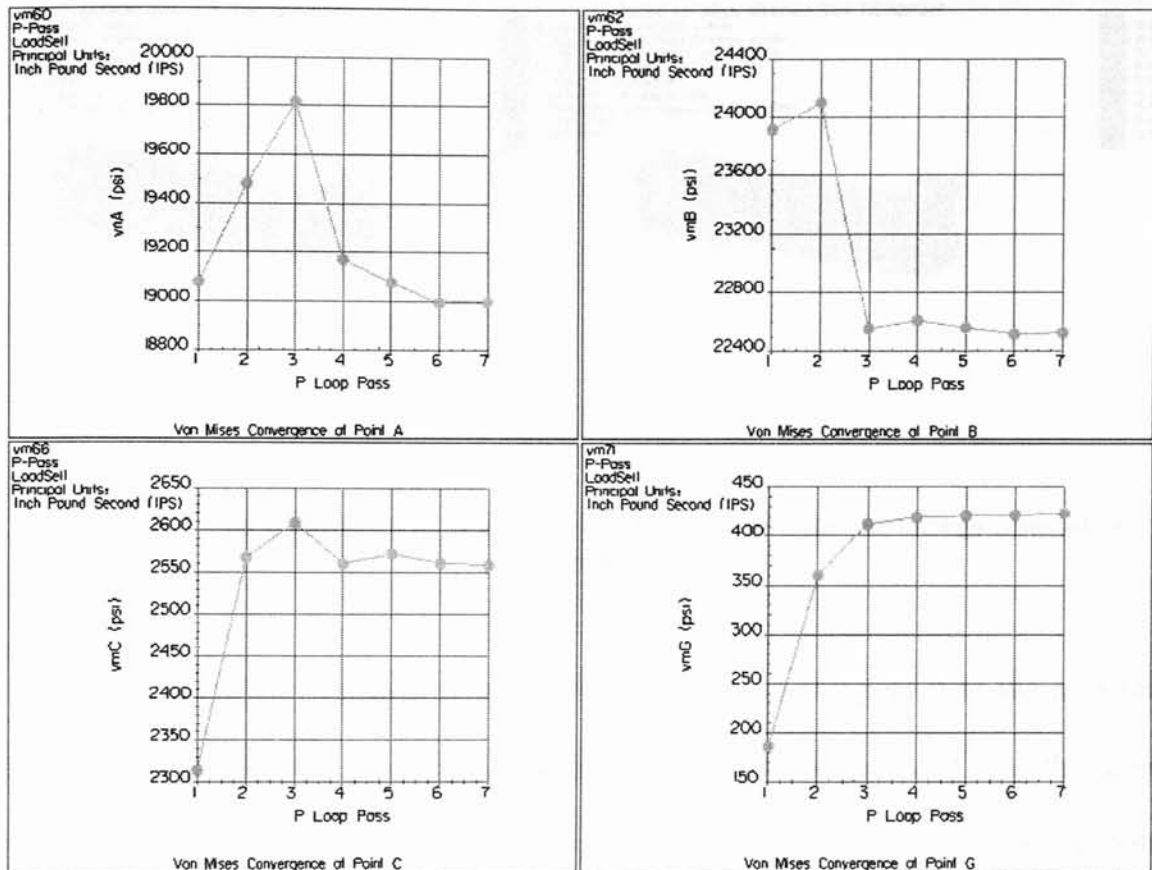


**Figure 4.17: Stress convergence at seed points within Test Specimen B, with core walls and facings modeled as shells.**

Figure 4.18 shows fringe plots of von Mises stress. The plots seem to agree with our previous two analyses of this specimen, except in the cell walls directly beneath the rubber pad. In these walls we observe artificially low stress values caused by our idealization of the rubber pad's lower surface as rigid, necessary to prevent penetration into the core.

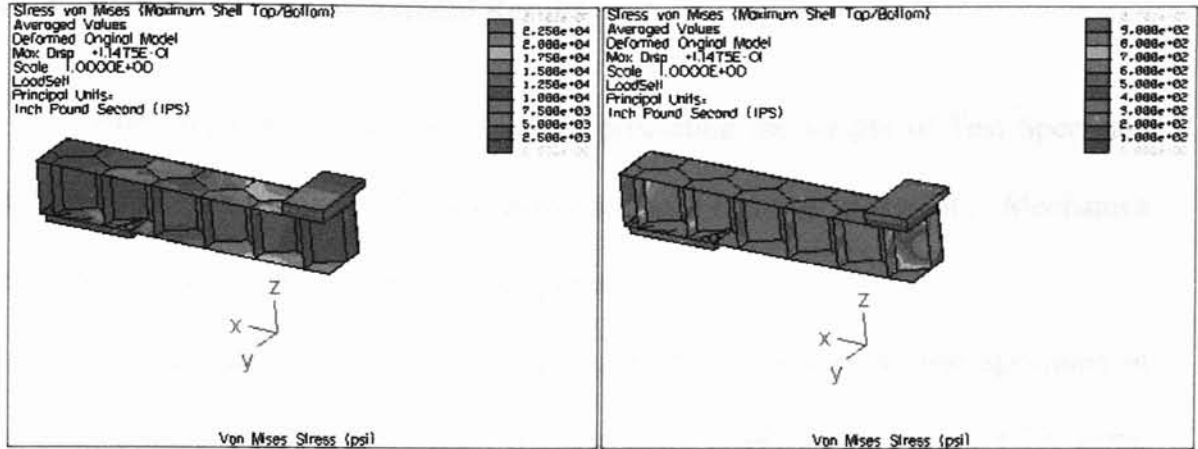


**Figure 4.18: Von Mises stress in Test Specimen B, with core walls and facings modeled as shells.**

To assess the accuracy of our current model, we compare it to the all-solid model in terms of stress and displacement values at discrete points. Using the same locations as in the previous section, we acquire the stress and displacement data summarized in Appendix F. We conclude that the displacement values in our current model are within 3% of the all-solid model, and our stress values average within about 9%.

We conclude that this model has achieved substantial savings in runtime over our previous models. The model is somewhat less accurate in predicting stresses, especially near the beam's center, but its deformation shows good agreement with our previous models.

#### 4.2.4. Comparison to Experimental Results

Mechanica does a very good job of predicting the weight of Test Specimen B. The test specimen's weight was measured as 74 grams in the lab; Mechanica indicates the weight of the beam is 73.4 grams.

To generate a load-deflection curve, we now analyze the test specimen at several different load values. The resulting curve is plotted in Figure 4.19, along with two curves obtained experimentally by Fullwood [Fullwood, 2002]. These curves (shown in pink in Figure 4.19) represent the original deflection data obtained from the Instron load frame. The red curves result from "correcting" the data to account for the deflection of the Instron machine, as described previously.

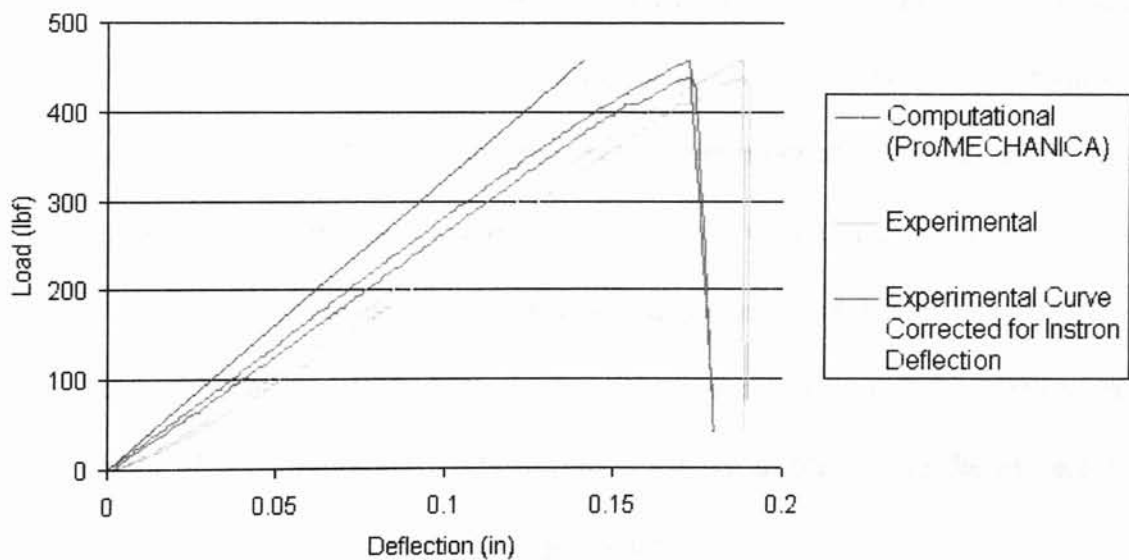


**Figure 4.19: Test Specimen B load versus deflection curves based on computational and experimental results, corrected for Instron deflection.**

For a given load, our finite element model predicts slightly less deflection than suggested by the experimental results. For example, at a load of 400 lbf the FEM deflection is 0.123 inches and the (corrected) experimental deflection is about



0.147 inches, a difference of 0.024 inches. As discussed earlier, potential causes for the discrepancy include the following:

- 1) Deflection of the steel test fixture.
- 2) Internal flaws or contaminants in the honeycomb core.
- 3) Variations in the core's wall thickness due to manufacturing limitations.

With these factors in mind, it is not surprising that the experimental stiffness falls slightly short of the computational stiffness since real-world boundary conditions, material properties, and specimen geometry necessarily fall short of the ideal model depicted by FEA.

#### 4.3. Effect of Number of Carbon Fiber Layers

We now evaluate the effect of adding additional layers of carbon fiber to the facings of Test Specimen B. The polycarbonate core in this study has a nominal wall thickness of 0.035 inches, and we increment the number of layers in each facing from zero to six. For each case, we record the beam's weight and the deflection at the lower facing's center point when the beam is subjected to a total load of 400 lbf.

Table 4.1 below summarizes the results of our study, and the results are shown graphically in Figure 4.20. Deflection is plotted in blue using the left scale, and weight is plotted in pink against the right scale.

**Table 4.1: Effect of number of carbon fiber layers.**

# layers CF	Beam deflection (in)	Beam full weight (gf)
0	1.390	50.9
1	0.166	62.7
2	0.108	74.5
3	0.089	86.3
4	0.079	98.2
5	0.072	110.0
6	0.068	121.8

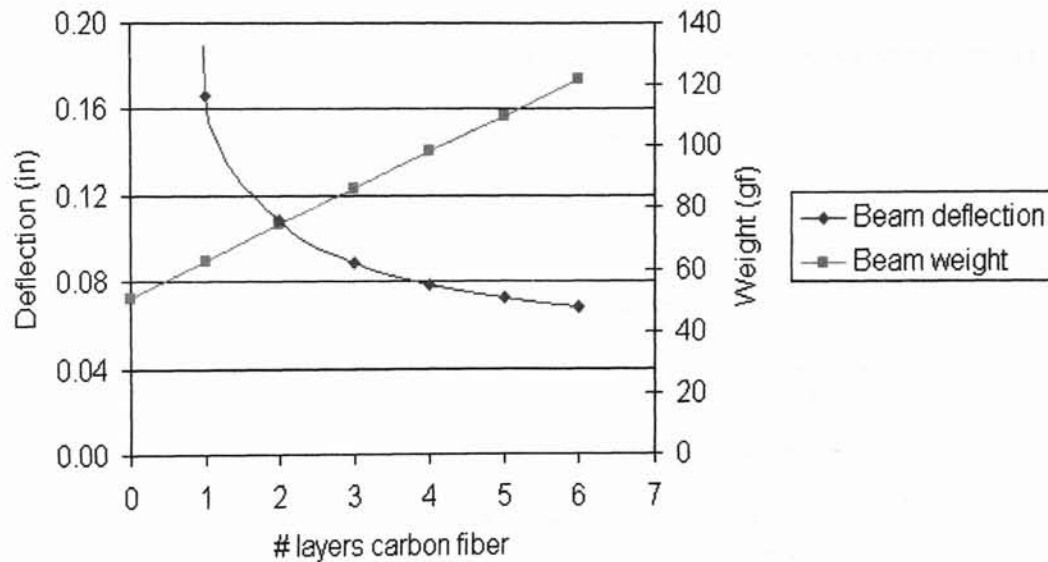


**Figure 4.20: Effect of number of carbon fiber layers.**

From the above plot, we conclude that using two layers rather than one layer of carbon fiber substantially increases the beam's stiffness. Adding additional layers increases the stiffness even more, but the benefits are less for each succeeding layer. The beam's total weight increases by 11.8 grams for each layer added.

#### 4.4. Effect of Wall Thickness

Next we evaluate the effect of changing the thickness of the walls in the polycarbonate core of Test Specimen B . The test specimen incorporates two layers of carbon fiber in each facing, and we increment the wall thickness from 0.010 inches to 0.100 inches. For each case, we record the beam's weight and the deflection at the lower facing's center point when the beam is subjected to a total load of 400 lbf.

Table 4.2 below summarizes the results of our study, and the results are shown graphically in Figure 4.21. Deflection is plotted in blue using the left scale, and weight is plotted in pink against the right scale.

**Table 4.2: Effect of wall thickness.**

wall thickness (in)	Beam deflection (in)	Beam full weight (gf)
0.010	0.233	38.2
0.015	0.176	45.4
0.025	0.129	60.0
0.035	0.108	74.5
0.045	0.097	89.1
0.055	0.089	103.6
0.065	0.084	118.2
0.075	0.079	132.7
0.100	0.072	169.1

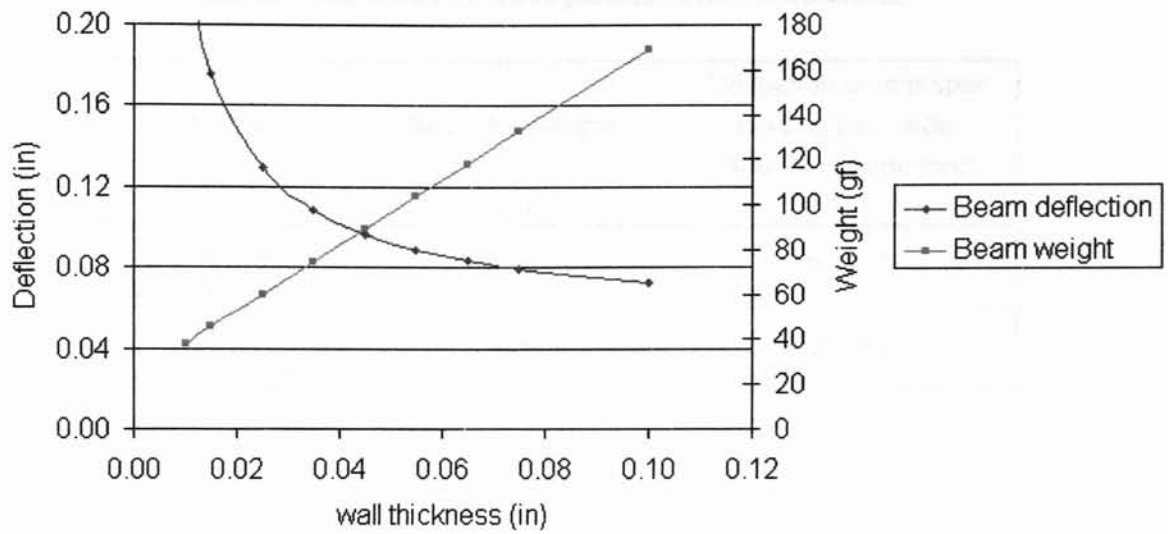


**Figure 4.21: Effect of core wall thickness.**

We conclude that changing the wall thickness has a substantial effect on the beam's stiffness, especially for thicknesses less than about 0.040 inches. Also, we see that the weight of the test specimen increases by approximately 14 grams for every 0.010 inches added to the wall thickness.

#### 4.5. Effect of Core Orientation

We now evaluate the effect of rotating the honeycomb core by 90° (about the z-axis) from its original orientation. Except for the new cell orientation, the geometry is identical to the original test specimen.

The following table compares the weight and deflection of the original Test Specimen B to the weight and deflection our new structure. We see that the deflection of the new structure is slightly larger, and the weight is slightly more. We therefore conclude that the original orientation was the more favorable geometry, although the difference in performance is small.

**Table 4.3: Test Specimen B comparison of core orientations.**

Model	Beam full weight (gf)	Deflection of mid-span loading pad under 400-lbf applied load (in)
Original Test Specimen B	73.4	0.1230
Alternate Core Orientation	73.6	0.1265

As an alternative example, we also rotate the core of Test Specimen A by 90° and compare the new weight and deflection to the original specimen. Table 4.4 below summarizes the weights and the deflection under a 600-lbf load. Based on this information, we conclude that the new orientation is preferable to the original orientation since the new geometry is stiffer and saves on weight.

**Table 4.4: Test Specimen A comparison of core orientations.**

Model	Beam full weight (gf)	Deflection of mid-span loading pad under 600-lbf applied load (in)
Original Test Specimen A	145.3	0.1312
Alternate Core Orientation	141.8	0.1244

## CHAPTER 5

### CONCLUSIONS AND RECOMMENDATIONS

#### 5.1. Conclusions

Pro/MECHANICA has been shown to be a useful tool for performing finite element analysis of freeform composite structures.

Three different methods of analyzing these structures were investigated in this research. The first method, modeling the entire structure with solid tetrahedral elements, proved somewhat prohibitive because it was so computationally intensive. The second method, in which carbon fiber facings were compressed to their mid-planes and meshed with shell elements, enabled an analysis to run faster. Comparing stress and displacement values of the second method to those of the first method suggested that the two analyses were in reasonably good agreement. The third method, idealizing the core walls as well as the facings with shell elements, substantially speeded up the analysis but was noticeably detrimental to the stress results.

Using each of the above three methods, we analyzed two freeform composite test specimens that had recently been tested in OSU's mechanical engineering labs. We saw reasonably good agreement between our computational results and

experimental results. Although FEA slightly overpredicted the experimental stiffness, the discrepancy can be attributed to analyzing “perfect” material properties, geometry, and boundary conditions. The real-world properties and behavior of any structure will naturally fall short of these idealizations.

Finally, we investigated the effects of altering the number of laminate layers in the facings, the thickness of the core walls, and the core orientation. We observed that our structure becomes stiffer as we increase the number of carbon fiber layers or the cell wall thickness, but the gain in stiffness is accompanied by a direct increase in weight. Analyzing core orientations for two different honeycomb geometries revealed that a longitudinal (rather than transverse) orientation of cell walls will sometimes (but not always) result in a stiffer structure.

## 5.2. Recommendations

Further research is recommended concerning the failure criteria of freeform composite structures. In this research effort, we predicted the stiffness and weight of our structures, but we did not predict the failure point of the specimens. Further knowledge of failure properties of the core materials and carbon fiber facings could add to the usefulness of the finite element models.

Additionally, research into the capabilities of alternative software packages is recommended. Although Pro/MECHANICA solved some very difficult analyses in this research effort, the software definitely has its limitations. In particular, the pre-processing capabilities of Mechanica seem inadequate for very complicated

geometries, and these are the norm rather than the exception in freeform composite fabrication.



## BIBLIOGRAPHY

- 3D Systems, [www.3dsystems.com](http://www.3dsystems.com) (2002).
- Adams, V. and Askenazi, A., *Building Better Products with Finite Element Analysis*, OnWord Press, 1999.
- Advanced Composites Group, *An Introduction to Advanced Composites and Prepreg Technology*, Advanced Composites Group Ltd., 1999.
- Argyris, J.H., "Energy Theorems and Structural Analysis," *Aircraft Engineering*, Oct., Nov., Dec. 1954 and Feb., Mar., Apr., May 1955.
- Argyris, J.H., "Recent Advances in Matrix Methods of Structural Analysis," *Progress in Aeronautical Science*, Vol. 4, 1964.
- ASTM C 393-00, "Standard Test Method for Flexural Properties of Sandwich Constructions," *Annual Book of ASTM Standards*, Vol. 15.03, pp. 23-26, 2000.
- Baker, A.J. and Pepper, D.W., *Finite Elements 1-2-3*, McGraw-Hill, Inc., 1991.
- Beaman, J.J., Barlow, J.W., Bourell, D.L., Crawford, R.H., Marcus, H.L., McAlea, K.P., *Solid Freeform Fabrication: A New Direction in Manufacturing*, Kluwer Academic Publishers, 1997.
- Burnett, D.S., *Finite Element Analysis: From Concepts to Applications*, AT&T Bell Laboratories, 1987.
- Clough, R.W., "The Finite Element Method in Plane Stress Analysis," *Proceedings, American Society of Civil Engineers, 2<sup>nd</sup> Conference on Electronic Computation*, Pittsburgh, Pa., pp. 345-378, Sept. 1960.
- Courant, R., "Variational Methods for the Solution of Problems of Equilibrium and Vibrations," *Bulletin of the American Mathematical Society*, Vol. 49, pp.1-23, 1943.

- Cruz, J.R., Shah, C.H., and Postyn, A.S., "Properties of Two Carbon Composite Materials Using LTM 25 Epoxy Resin," *NASA Technical Memorandum 110286*, Virginia, 1996.
- Fullwood, K., "Strength Comparison between Freeform Fabricated Core and Nomex Core Composite Sandwiches," Master's Thesis, Oklahoma State University, 2002.
- Good, J.K., "Modeling Rubber Covered Nip Rollers in Web Lines," *Proceedings of the Sixth International Conference on Web Handling*, Oklahoma State University, Stillwater, OK, June 10-13, 2001.
- Hrenikoff, A., "Solution of Problems in Elasticity by the Frame Work Method," *Journal of Applied Mechanics*, Vol. 8, No. 4, pp. 169-175, Dec. 1941.
- Jacobs, P.F., *Stereolithography and other RP&M Technologies*, Society of Manufacturing Engineers, 1996.
- Kai, C.C., and Fai, L.K., *Rapid Prototyping: Principles and Applications in Manufacturing*, John Wiley & Sons (Asia) Pte Ltd., 1997.
- Kalpakjian, S., *Manufacturing Processes for Engineering Materials* (3<sup>rd</sup> Ed.), Addison Wesley Longman, Inc., 1997.
- Kietzman, J., "Rapid Prototyping Polymer Parts via Shape Deposition Manufacturing," Ph.D. Dissertation, Stanford University, 1999.
- Logan, D., *A First Course in the Finite Element Method* (2<sup>nd</sup> Ed.), PWS Publishing Company, 1993.
- Martin, H.C., "Plane Elasticity Problems and the Direct Stiffness Method," *The Trend in Engineering*, Vol. 13, pp. 5-19, Jan. 1961.
- McHenry, D., "A Lattice Analogy for the Solution of Plane Stress Problems," *Journal of Institution of Civil Engineers*, Vol. 21, pp. 59-82, Dec. 1943.
- Parametric Technology Corporation, *Pro/MECHANICA Advanced Workshop Training Guide*, Parametric Technology Corporation, 1999.
- Parametric Technology Corporation, [www.ptc.com](http://www.ptc.com) (2002).
- Patterson, J.L., "The Study of the Feasibility of Photosensitive Resin Core Materials for Freeform Fabricated Composites as Compared to Nomex Core Materials in a Dry and Wet Environment," Master's Thesis, Oklahoma State University, 2001.

Rapid Prototyping Chemicals, [www.rpc.ch](http://www.rpc.ch) (2002).

Stratasys, Inc., [www.stratasys.com](http://www.stratasys.com) (2002).

Texcel, [www.texcelrubber.com](http://www.texcelrubber.com) (2002).

Toogood, R., *Pro/MECHANICA Structure: Release 2001 – Integrated Mode Student Edition Tutorial*, Schroff Development Corporation, 2001.

Turner, M.J., Clough, R.W., Martin, H.C., and Topp, L.J., “Stiffness and Deflection Analysis of Complex Structures,” *Journal of Aeronautical Sciences*, Vol. 23, No. 9, pp. 805-824, Sept. 1956.

Zienkiewicz, O.C. and Cheung, Y.K., “Finite Elements in the Solution of Field Problems,” *The Engineer*, pp. 507-510, Sept. 24, 1965.

---

APPENDICES

---

## APPENDIX A: RPC 700 ND RESIN DATA SHEET

700 ND Resin Data [Rapid Prototyping Chemicals, 2002]

### Properties

MEASUREMENT	METHOD	VALUE
Penetration Depth (DP)	Window panes	4.6 mils (0.12mm)
Critical Exposure (Ec)	Window panes	10.6 mJ/cm <sup>2</sup>
Viscosity of liquid resin	Brookfield @ 30°C	500 cps
Green flex-modulus after 10 min.		130 MPa
Green flex-modulus after 1 hour		270 MPa
Flexural modulus after post-cure		2400 MPa
Tensile modulus after post-cure	ISO 527	2500 MPa
Tensile strength after post cure	ISO 527	71 MPa
Elongation to break	ISO 527	12.5%
Shore D		82
Impact after post-cure, unnotched	ISO 179	30 kJ/m <sup>2</sup>
Glass transition, T <sub>g</sub>	DSC	81

APPENDIX B: LTM25 / CFS003 2x2 TWILL DATA SHEET

Properties reproduced from NASA technical memorandum 110286 [Cruz, et al., 1996].

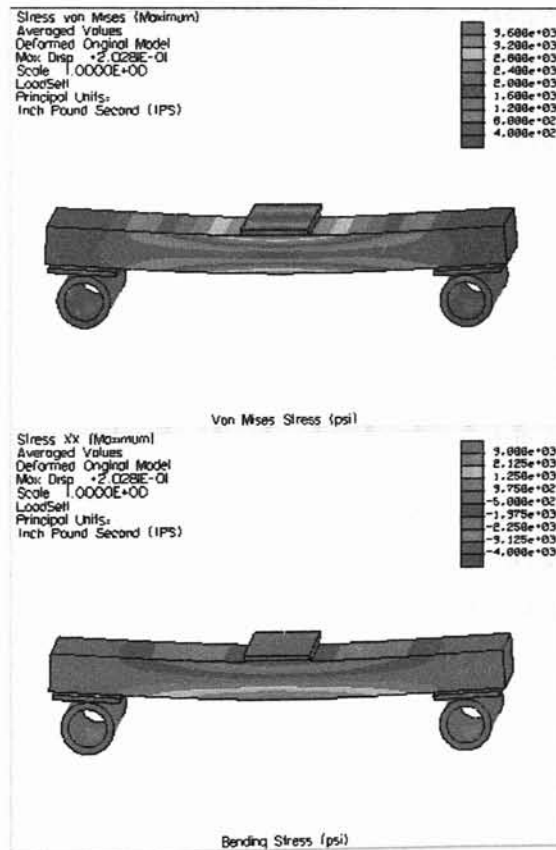
Property	Value
$E_1^t$ , Longitudinal modulus, tension (Msi)	7.06
$\nu_{12}^t$ , major Poisson's ratio, tension	0.042
$E_1^c$ , Longitudinal modulus, compression (Msi)	7.20
$\nu_{12}^c$ , major Poisson's ratio, compression	0.033
$E_2^t$ , Transverse modulus, tension (Msi)	7.52
$\nu_{21}^t$ , minor Poisson's ratio, tension	0.028
$E_2^c$ , Transverse modulus, compression (Msi)	7.54
$\nu_{21}^c$ , minor Poisson's ratio, compression	0.035
$G_{12}^s$ , in-plane shear modulus (Msi)	0.414
$F_1^{tu}$ , Longitudinal ultimate stress, tension (Ksi)	81.6
$F_1^{cu}$ , Longitudinal ultimate stress, compression (Ksi)	93.1
$F_2^{tu}$ , Transverse ultimate stress, tension (Ksi)	88.8
$F_2^{cu}$ , Transverse ultimate stress, compression (Ksi)	81.7
$F_{12}^{su}$ , in-plane shear ultimate stress (Ksi)	12.2
$\epsilon_1^{tu}$ , longitudinal ultimate strain, tension ( $\mu\text{in/in}$ )	11,100
$\epsilon_1^{cu}$ , longitudinal ultimate strain, compression ( $\mu\text{in/in}$ )	12,900
$\epsilon_2^{tu}$ , transverse ultimate strain, tension ( $\mu\text{in/in}$ )	11,400
$\epsilon_2^{cu}$ , transverse ultimate strain, compression ( $\mu\text{in/in}$ )	10,800
$\nu_{12}^{su}$ , in-plane ultimate strain ( $\mu\text{in/in}$ )	29,600
$V_f$ , Fiber volume fraction (%)	46.9
t, Thickness (in)	0.00904
T, Cure temperature ( $^{\circ}\text{F}$ )	160 for 10hrs

## APPENDIX C: COMPARISON OF TWO LOADING CONDITIONS

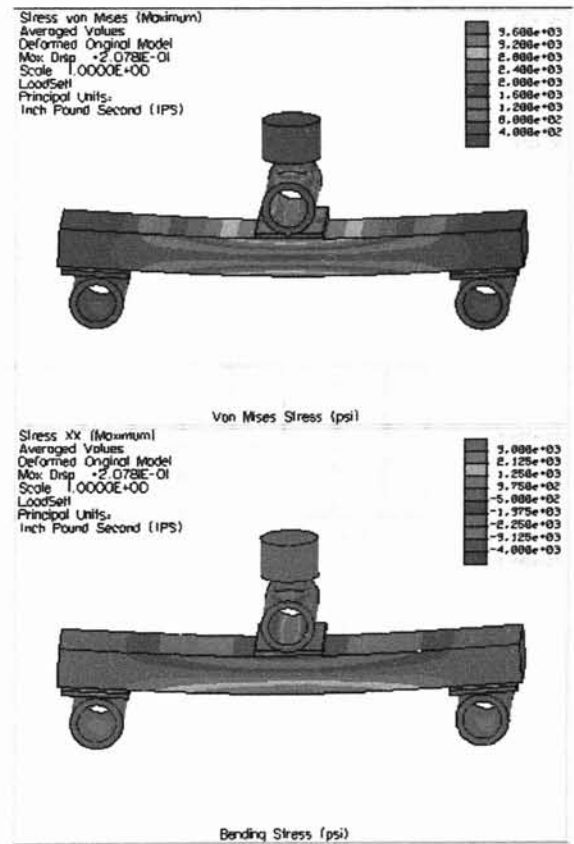
*Applied load is 600 lbf.*

*Beam is constructed of RPC 700 ND photocurable resin.*

### Stress distributions from uniform distributed load.



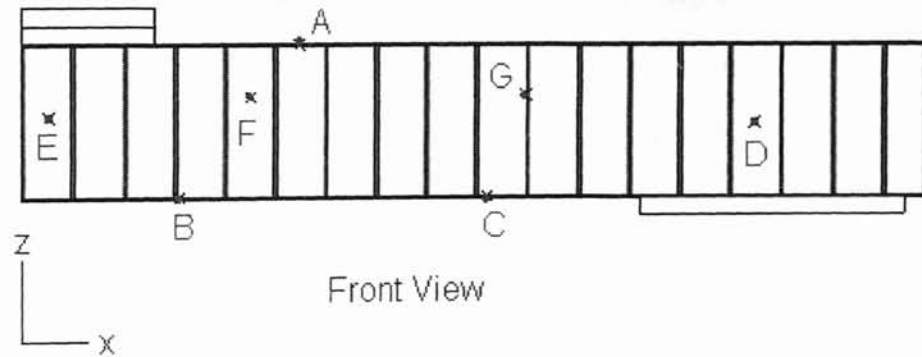
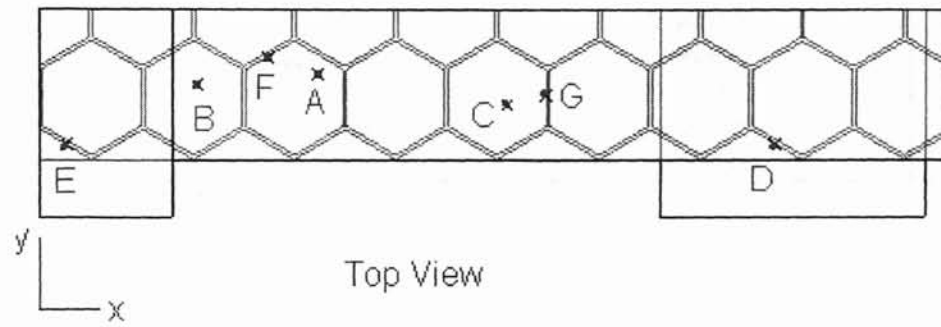
### Stress distributions from incorporation of Instron head.



	Uniform distributed load	Incorporation of Instron head
FEM mesh	1,208 tetrahedra 2 contact regions	1,642 tetrahedra 3 contact regions
Max displacement of test specimen (in)	0.2028	0.2029
Max von Mises stress within test specimen (psi)	3,959	3,964
Analysis run time (minutes)	54.41	104.03

APPENDIX D: COMPARISON OF DISPLACEMENT AND STRESS VALUES  
AT SEED POINT LOCATIONS IN HONEYCOMB CORE TEST SPECIMEN

Seed point locations:





Comparison of All-Solid Model to Facings-Compressed Model:

Displacements at Seed Points:

Location	Displacement Value (in)		% error
	All Solid Elements	Facings Compressed to Shells	
Point A	0.146310	0.151759	3.72
Point B	0.176080	0.183315	4.11
Point C	0.091173	0.093391	2.43
Point D	0.005554	0.005451	1.87
Point E	0.196907	0.202443	2.81
Point F	0.161166	0.165871	2.92
Point G	0.077256	0.079206	2.52
<b>Average Percent Error:</b>			<b>2.91</b>

Von Mises Stress at Seed Points:

Location	Von Mises Stress (psi)		% error
	All Solid Elements	Facings Compressed to Shells	
Point A	24,777.63	27,649.42	11.59
Point B	31,217.12	33,249.61	6.51
Point C	16,057.41	16,730.23	4.19
Point D	2,694.78	2,703.90	0.34
Point E	1,301.37	1,415.78	8.79
Point F	5,202.10	5,301.88	1.92
<b>Average Percent Error:</b>			<b>5.56</b>

Comparison of All-Solid Model to Surface Model:

Displacements at Seed Points:

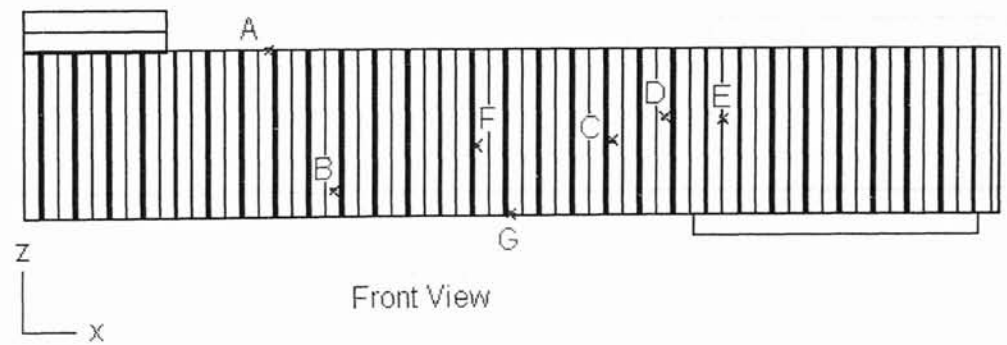
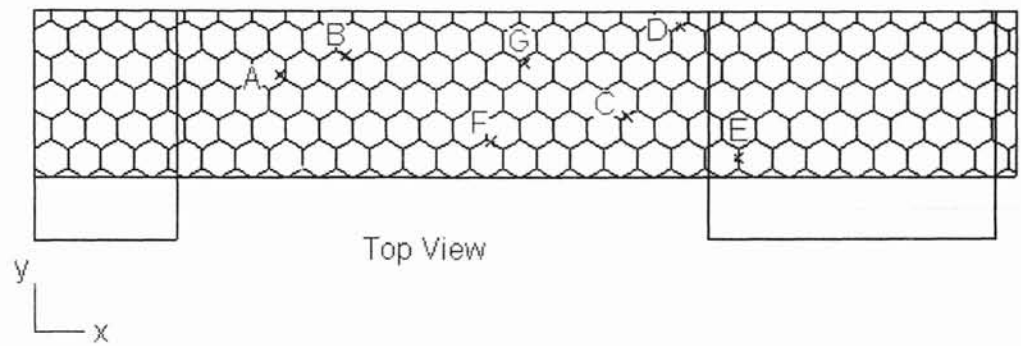
Location	Displacement Value (in)		% error
	All Solid Elements	Core and Facings Are Shells	
Point A	0.146310	0.144593	1.17
Point B	0.176080	0.173628	1.39
Point C	0.091173	0.089880	1.42
Point D	0.005554	0.005459	1.71
Point E	0.196907	0.185749	5.67
Point F	0.161166	0.158171	1.86
Point G	0.077256	0.075496	2.28
<b>Average Percent Error:</b>			<b>2.21</b>

Von Mises Stress at Seed Points:

Location	Von Mises Stress (psi)		% error
	All Solid Elements	Core and Facings Are Shells	
Point A	24,777.63	27,217.11	9.85
Point B	31,217.12	33,927.65	8.68
Point C	16,057.41	16,697.80	3.99
Point D	2,694.78	2,759.50	2.40
Point E	1,301.37	403.96	68.96
Point F	5,202.10	5,475.31	5.25
<b>Average Percent Error:</b>			<b>16.52</b>

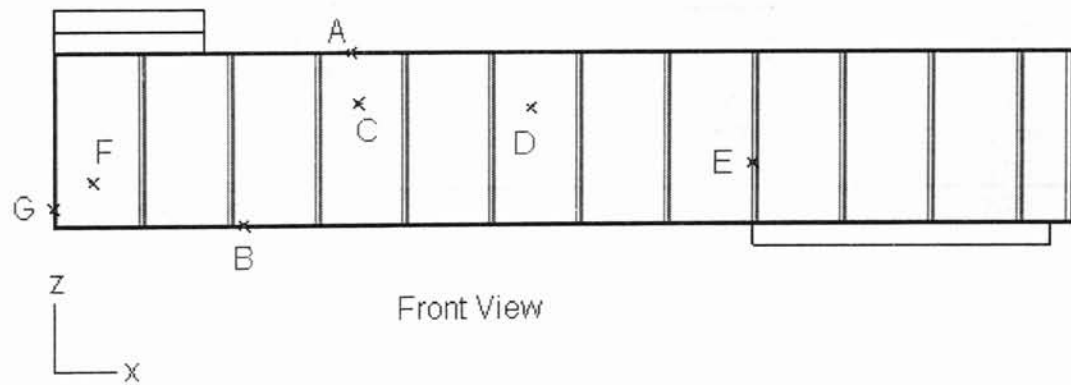
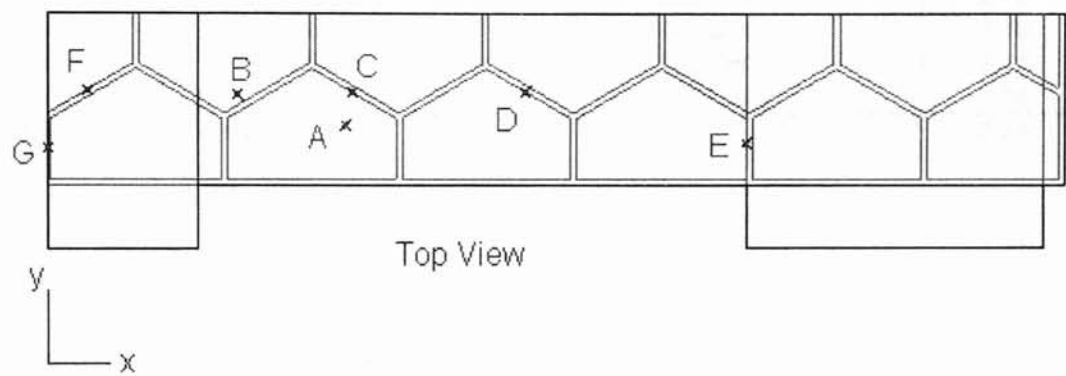
APPENDIX E: SEED POINT LOCATIONS IN TEST SPECIMEN A

Seed point locations:



APPENDIX F: COMPARISON OF DISPLACEMENT AND STRESS VALUES  
AT SEED POINT LOCATIONS IN TEST SPECIMEN B

Seed point locations:



Comparison of All-Solid Model to Facings-Compressed Model:

Displacements at Seed Points:

Location	Displacement Value (in)		% error
	All Solid Elements	Facings Compressed to Shells	
Point A	0.088279	0.090730	2.78
Point B	0.102586	0.105333	2.68
Point C	0.087650	0.090064	2.75
Point D	0.061150	0.062857	2.79
Point E	0.023013	0.023636	2.71
Point F	0.114467	0.117598	2.74
<b>Average Percent Error:</b>			<b>2.74</b>

Von Mises Stress at Seed Points:

Location	Von Mises Stress (psi)		% error
	All Solid Elements	Facings Compressed to Shells	
Point A	19,449.67	19,038.52	2.11
Point B	21,258.87	23,198.70	9.12
Point C	2,617.43	2,555.17	2.38
Point D	2,549.69	2,594.67	1.76
Point E	500.81	551.71	10.16
Point F	580.25	609.29	5.00
<b>Average Percent Error:</b>			<b>5.09</b>

### Comparison of All-Solid Model to Surface Model:

Displacements at Seed Points:

Location	Displacement Value (in)		[% error]
	All Solid Elements	Core and Facings Are Shells	
Point A	0.088279	0.086944	1.51
Point B	0.102586	0.099604	2.91
Point C	0.087650	0.086248	1.60
Point D	0.061150	0.061086	0.10
Point E	0.023013	0.023590	2.50
Point F	0.114467	0.108093	5.57

**Average Percent Error:**

**2.37**

Von Mises Stress at Seed Points:

Location	Von Mises Stress (psi)		[% error]
	All Solid Elements	Core and Facings Are Shells	
Point A	19,449.67	18,996.68	2.33
Point B	21,258.87	22,523.26	5.95
Point C	2,617.43	2,470.84	5.60
Point D	2,549.69	2,558.03	0.33
Point E	500.81	427.99	14.54
Point F	580.25	455.47	21.50

**Average Percent Error:**

**8.37**

VITA 2

Jeffrey Ryan Callicoa

Candidate for the Degree of

Master of Science

Thesis: FINITE ELEMENT ANALYSIS OF FREEFORM COMPOSITE  
STRUCTURES

Major Field: Mechanical Engineering

Biographical:

Personal Data: Born in Green Bay, Wisconsin, on September 26, 1976, the son of R. Harve and Norma Callicoa.

Education: Graduated from Bartlesville High School, Bartlesville, Oklahoma in May 1995; received Bachelor of Science degree in Mechanical Engineering from Oklahoma State University, Stillwater, Oklahoma in May 2000. Completed the requirements for the Master of Science degree with a major in Mechanical Engineering at Oklahoma State University in December, 2002.

Experience: Summer employee in Prototype Testing department at The Charles Machine Works, Inc., Perry, Oklahoma, 1996-1999; Engineering Intern in Printing Systems department at IBM, Boulder, Colorado, 2000. Teaching Assistant for OSU undergraduate Computer Aided Design course, 2000-2002; Graduate Research Assistant in OSU Department of Mechanical and Aerospace Engineering, 2000 to present.

Professional Memberships: American Society of Mechanical Engineers, Pi Tau Sigma, Tau Beta Pi.